Mechanical Properties of Bone at the Sub-lamellar Level

THESIS SUBMITTED TO THE UNIVERSITY OF LONDON

FOR THE DEGREE OF DOCTOR OF PHILOSOPHY

SEPTEMBER 2012

BY

Ines Jimenez Palomar

Supervisor: Dr Asa H. Barber

SCHOOL OF ENGINEERING AND MATERIALS SCIENCE

QUEEN MARY UNIVERSITY OF LONDON

MILE END ROAD, LONDON, E1 4NS

Abstract

Bone is a complex fibrous biological nanocomposite material optimized to avoid catastrophic failure and to perform a variety of mechanical functions, most notably load bearing. The fracture behaviour of bone is expected to be controlled by the various structural features present across the many existing hierarchical length scales. Micron sized bone lamellae present the simplest composite unit in bone consisting of mineralized collagen fibrils within a protein matrix, with some work suggesting that this length scale dominates the fracture of whole bone. However, the synergy between the bone components even at these relatively small length scales is poorly understood. The aim of this work is to therefore examine the mechanical properties of bone at length scales where the bone material itself can be considered as a composite material. To achieve this, discrete volumes of bone corresponding to the sub-lamellar unit were mechanically tested using an *in situ* Atomic Force Microscope (AFM) while monitoring using Scanning Electron Microscope (SEM). The elastic modulus of sub-lamellar bone units mechanically tested by the AFM in a bending configuration within the SEM was shown to be similar in both wet and SEM vacuum conditions, indicating that the SEM vacuum is insufficiently strong to drive off water from hydrated bone samples at lamellae length scales. AFM-SEM mechanical testing was extended to determine the structural effects of collagen fibril orientation in bone sub-lamellar units on both elastic modulus and fracture. Final experiments examined small scale mechanical properties of osteoporotic

bone, with results highlighting how osteoporosis has little effect on the strength of the bone material but lowers the elastic modulus. This work therefore highlights the use of small scale mechanical testing using AFM and SEM to determine the influence of structural organization, specifically collagen fibril orientation, and compositional changes induced by osteoporosis on resultant bone material behaviour.

Table of contents

List of figures

List of tables

Declaration

I declare that the work performed is entirely my own, conducted during the course of my Ph.D. studies at the Queen Mary University of London and has not been previously submitted for a degree at this or any other university.

Ines Jimenez-Palomar

I would like to dedicate this work to my best friends Laura and Elvia for always pushing me forward encouragingly yet sometimes brutally.

"It's possible…" – Dun Lu

Acknowledgements

First of all I would like to thank my supervisor Dr Asa H. Barber for his guidance and valuable support throughout my Ph.D. studies. I would also like to thank all the group members who I had the pleasure to meet and work with and who taught me so much: Dr Wei Wang, Dr Shuangwu Li, Dr Dun Lu, Dr Fei Hang, Russell J. Bailey, Dr Urszula Stachewicz, Beatriz Cortes-Ballesteros and Congwei Wang. I would also like to encourage and welcome new members to the group: Yiran An, Filipe Almeida, Neelam Siyab, Hao Zhang and Alexander Kao.

At the office, I would like to acknowledge my colleague and friend Alan Parish for always coming up with the most intelligent and timely solutions to my concerns inside and outside the lab and all of the people at the Ph.D. Hub at SEMS for bringing so much fun and life into the office. At home I would like to thank all of the passing roomies, my dog Travis and Oscar O'Dwyer for making the flat feel like home, supporting me and making my life easier and happier.

In the lab, I would like to thank Dr Zofia Luklinska for always keeping an eye out for me; Dr Ken Png for training me to use the equipment, especially Quanta; and Mick Willis for his insight and help with sample preparation. I would also like to acknowledge the NanoVision Centre and Nanoforce at Queen Mary University of London for use of facilities.

Back home, in Mexico, I would like to thank my friends, Laura Jileta and Elvia Zazueta, and my family for believing in me and always being there for me night and day despite being ~8,827 Km apart and ~6 hours behind. I would also like to thank Carlos J. Pasquali for developing the Matlab and Octave scripts for AFM data analysis.

I would also like to thank the research collaborators at the Koret School of Veterinary Medicine, The Hebrew University of Jerusalem in Israel, Ron Shahar and Anna Shipov for providing the rat bone samples as well as encouraging discussion and innovation.

Last but most importantly I would like to thank Queen Mary University of London for being my home for the past 8 years; the Engineering and Physics Research Council (EPSRC) for fully funding my studies for the past 3 years; my brother Claudio and my sister Ana for showing me that life is easy and anything is possible and my parents for always saying "Yes" to all of my endeavours.

Thank you,

Ines

Publications

Published

I. Jimenez-Palomar, A.H. Barber. Failure of bone at the sub-lamellar level using in situ AFM-SEM Investigations. MRS Conference Proceedings, 1424-ss04-05-oo03-05, 2012.

I. Jimenez-Palomar, A. Shipov, R. Shahar and A.H. Barber. Influence of SEM vacuum on bone micromechanics using in situ AFM. Journal of the Mechanical Behavior of Biomedical Materials, 5, 149-155, 2012.

F. Hang, D. Lu, R. J. Bailey, I. Jimenez-Palomar, U. Stachewicz, B. Cortes-Ballesteros, M. Davies, M. Zech, C. Bödefeld and A. H. Barber. In situ tensile testing of nanofibers by combining atomic force microscopy and scanning electron microscopy, Nanotechnology, 22 (36), 2011.

A.H. Barber, I. Jimenez-Palomar. Effect of environment on mechanical properties of micron sized beams of bone fabricated using FIB. MRS Conference Proceedings 1274-QQ07-04, 2010.

Submitted

I. Jimenez-Palomar, A. Shipov, R. Shahar, A.H. Barber. The dependence of structural orientation on sub-lamellar bone mechanics. (*submitted*)

In preparation

I. Jimenez-Palomar, A.H. Barber The effect of strength and toughness of bone at the sub-lamellar level via in situ AFM-SEM mechanical testing.

I. Jimenez-Palomar, A.H. Barber Measuring the effect of osteoporosis in ovariectomized on the bone mechanics at the sub-lamellar level using in situ AFM-SEM methods.

Chapter 1. Introduction

Bone is generally acknowledged as a prevalent example of a biological hierarchical material with corresponding structural and mechanical properties that vary across a range of length scales as shown in Figure 1.1. In order to understand the intrinsic material properties of bone, the simplest unit that incorporates all of the components would need to be isolated from whole bone. The isolation of this unit would allow the study of bone as a composite material, ignoring the effect of larger geometrical and structural features found at higher hierarchical levels. The aim of this Ph.D. thesis is to therefore isolate bone material at a scale that allows consideration of the discrete unit as a composite material and measure corresponding mechanical properties. Such activity will thus determine the intrinsic mechanical properties of the bone as a material, which is distinct from larger scale mechanical tests requiring information on the complex structural hierarchy of bone, and evaluate the effects of both composition and the organization of these components on mechanical properties.

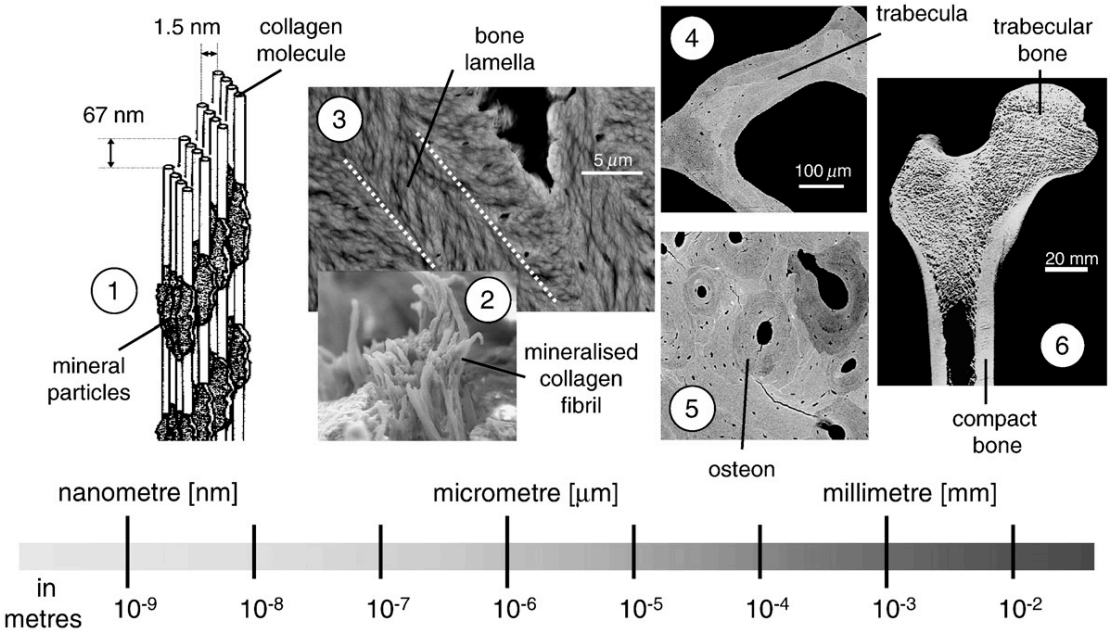

Figure 1.1 The hierarchical structure of bone. From left to right: 1) the nanocomposite of collagen and mineral particles; 2) exposed mineralized collagen fibrils of a fracture surface; 3) lamellar arrangement of bone around an osteocyte lacuna; 4) trabecula consisting of several bone packets; 5) osteons forming compact bone and 6) longitudinal cross-section through a proximal femur showing trabecular bone at the top and compact bone at the bottom (Weinkamer & Fratzl 2011) used with permission from the publisher.

This thesis focuses on establishing bone as a composite material and examines existing literature on the structure of bone at different hierarchical levels as well as the effect of structure on the mechanical properties as detailed in Chapter 2. The justification for consideration of bone as a composite material is demonstrated when examining synthetic composite materials such as multi-walled carbon nanotubes in low density polyethylene in Figure 1.2. The failure surface of the synthetic nanocomposite in Figure 1.2 shows similarities with the fracture surface of bone material in Figure 1.1, insert (2), particularly the presence of ordered fibrous material extending from the fracture surface.

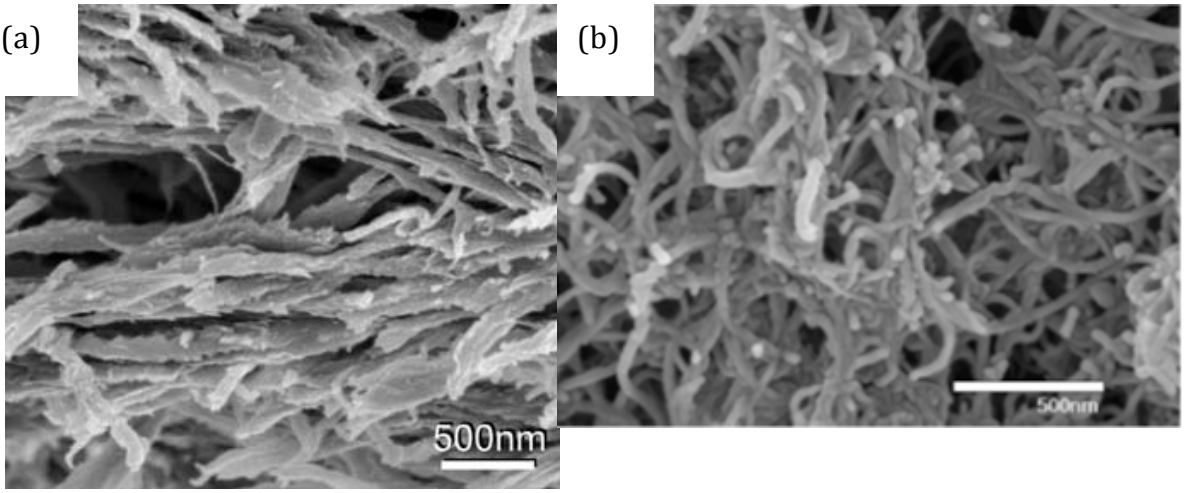

Figure 1.2 Scanning electron micrograph showing (a) bone at the sub-lamellar level with the mineralized collagen fibrils exposed at the surface fracture (Fantner et al. 2006) used with permission from the publisher and (b) the fracture surface of a composite of multi-walled carbon nanotubes in polystyrene (MWNTs in PS) (Zhang et al. 2009) used in accordance with the open access re-use policy.

Thus, resultant mechanical concepts developed in synthetic composites can be applied to bone materials to provide direct structure-property information. The similarity of bone and synthetic structures potentially allows us to use traditional mechanical testing methods and corresponding mechanical models in order to understand bone at the micron to sub-micron level shown in Figure 1.1.

The lamellar unit, as shown in Figure 1.3, is the smallest unit in bone that incorporates all of the components, namely fibrous collagen, nanoparticulate hydroxyapatite, amorphous non-collagenous proteins (NCPs) and water. The length scale of the lamellar units is therefore where bone can be considered a composite material. As has been studied extensively by Currey, the amount of

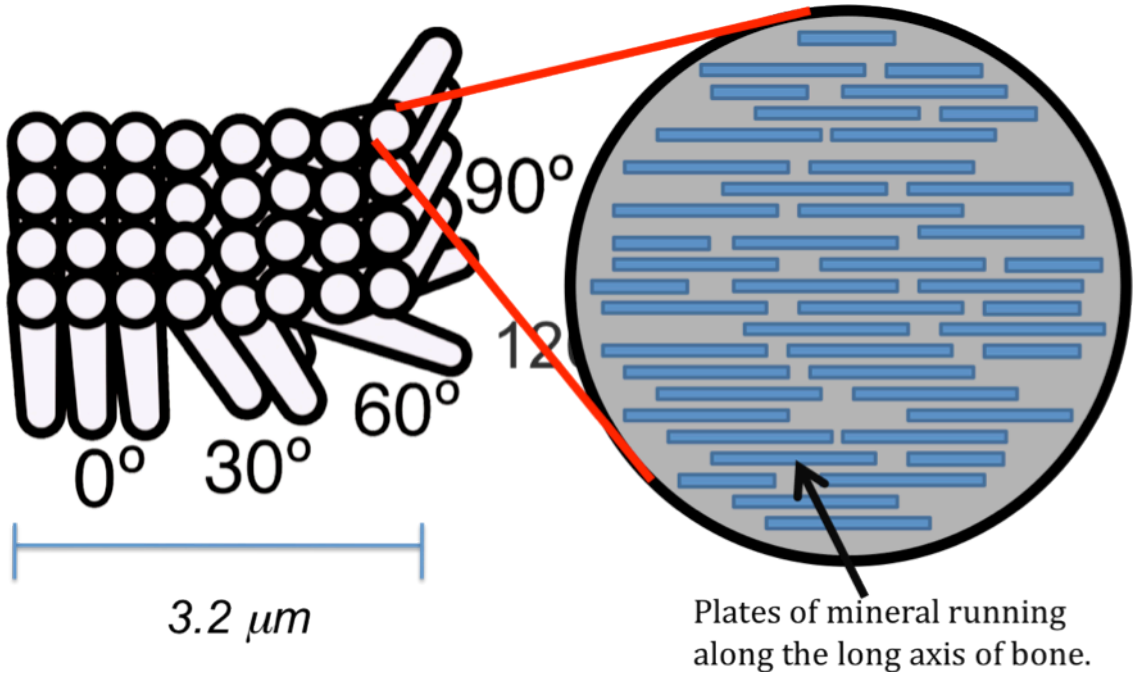

Figure 1.3 Schematic diagram of the lamellar unit in rat bone with the long axis of the mineralized collagen fibrils running parallel to the long axis of bone.

each component in bone affects resultant whole bone mechanics as has been studied across many different animal species including human, deer antler and whale bulla (Currey 1979; Currey 1988; Currey et al. 2009). The bone composition is directly related to its mechanical properties, which in turn is directly related to the mechanical function. The control of bone composition in different organisms therefore makes bone a particularly effective biological material for a range of mechanical functions where, for example, a combination of stiffness and toughness is required. The focus of this study is on testing the lamellar unit of bone, which incorporates all of the significant components of bone. Indeed, the basic lamellar unit must also interact with the other units to define the overall mechanical properties of whole bone.

Previous literature, subsequently described in Chapter 2, has exploited a range of testing methods to evaluate the mechanical properties of bone across the range of length scales shown in Figure 1.1. Perhaps the most straight-forward mechanical tests are to examine whole bone samples using tensile and compression testing machines. These larger testing methods evaluate bone across all of its hierarchical length scales and represent the complex synergy, as well as averaging, over all of the components and their geometric organizations. The structural complexity of bone thus makes determination of structure-property relationships difficult. Mechanical testing at smaller length scales simplifies the structural problem and has notably led to researchers using nanoindentation to evaluate bone mechanics (Rho, Tsui & Pharr 1997; Guo & Goldstein 2000; Silva et al. 2004; Fratzl-Zelman et al. 2009; Maïmoun et al. 2012). Although nanoindentation has the advantage of testing bone at the smaller hierarchical levels, the volume examined in bone samples and the evaluation of the heterogeneous structure is challenging. However, nanoindentation has been effective in making comparisons between different areas of bone (Rho, Tsui & Pharr 1997; Gupta, Stachewicz & Wagermaier 2006; Fratzl-Zelman et al. 2009), variations in bone types (Rho, Tsui & Pharr 1997), and the effect of disease (Guo & Goldstein 2000; Fratzl-Zelman et al. 2009; Maïmoun et al. 2012) on the mechanical properties of bone at smaller hierarchical levels. Yet these results have shown a significant disparity with results from earlier studies testing bone at higher hierarchical levels such as the architectural levels (Choi et al. 1990; Barengolts et al. 1993; Kasra et al. 1997; Cory et al. 2010) which Rho et

al. (1997) attributes to problems that arise when testing bone in 3-point bending. However Rho et al. (1997) also states that there could be an issue with the Poisson's ratio (Rho, Tsui & Pharr 1997) values of bone at the small length scales considered in indentation, which is required in order to interpret indentation data but is assumed, perhaps incorrectly, to be in the range of 0.28-0.33 (Shahar et al. 2007). Shahar et al. (2007) points out that the Poisson's ratio for cortical bone has been measured via a vast number of techniques and ranges from 0.12-0.63 (Reilly & Burstein 1975; Ashman et al. 1984; Pithioux, Lasaygues & Chabrand 2002). The values typically used therefore a somewhat 'averaged guess' and could have an influence on the validity of the results from nanoindentation techniques (Shahar et al. 2007). Studies by Fratzl-Zelman et al. (2009), also indicated how nanoindentation is insensitive to organic matrix mechanics, specifically the non-collagenous proteins (NCPs), as they are unable to explain why a decrease in mineral content did not seem to cause a corresponding decrease in the elastic modulus tested using nanoindentation (Fratzl-Zelman et al. 2009).

To resolve the issues of testing bone volume at lamellar length scales, techniques are developed for this study involving a combination of the Scanning Electron Microscope (SEM), the Focused Ion Beam (FIB) microscope and the Atomic Force Microscope (AFM). These three techniques were used collectively in order to clearly identify the sample, isolate the sub-lamellar unit and provide subsequent *in situ* mechanical testing as shown in Figure 1.4 and detailed in Chapter 3. Particular care is taken in justifying the use of the techniques in evaluating bone in a more natural state while

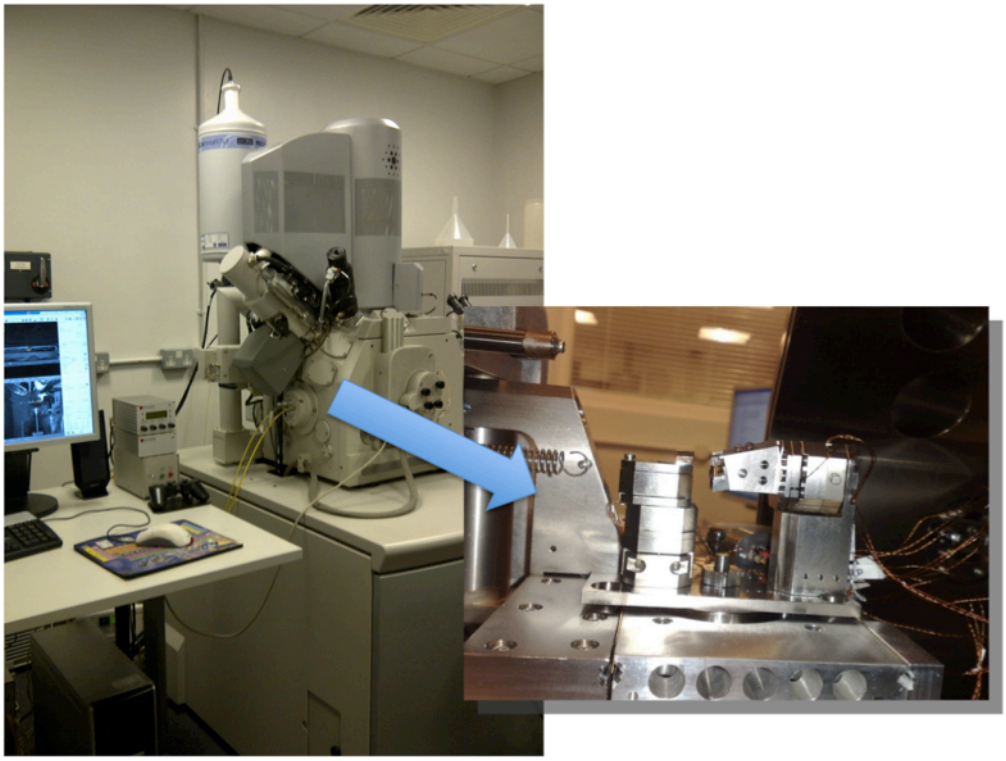

Figure 1.4 Photographs highlighting the experimental setup used to combine AFM, SEM and FIB techniques within a single instrument. The left image shows a standard SEM-FIB dual beam system (Quanta 3D FEG, FEI, USA/EU) whereas the right image indicates a custom built AFM that sits inside the SEM vacuum chamber and therefore allows in situ mechanical testing of small volumes of bone.

collecting appropriate mechanical information, which will be addressed throughout the thesis. In brief, the advantages of the combination of these three techniques are that the sample can be adequately identified and monitored using SEM imaging, with FIB methods allowing the isolation of discrete bone volumes for subsequent mechanical testing using in situ AFM techniques. An obvious potential disadvantage of such a system is the exposure of bone samples to the vacuum conditions of the SEM chamber. In

particular, testing the mechanical properties of bone inside the SEM vacuum chamber may dry the bone material and significantly affect mechanical performance.

Though the drying of bone is known to have an effect on its mechanical properties, as will be further discussed in Chapter 4, it is still unclear if water at the micron length scales can be removed by the SEM vacuum pumps as the water found in this level is tightly bound to the mineralized collagen structure. This concern is fully reviewed in Chapter 4, which validates the methods used across the thesis to shows how the vacuum chamber of the SEM does not remove the bound water at the submicron level.

Once a suitable set of experimental parameters were defined, different micron-length scale features in bone could be observed, isolated and mechanically tested. This sample preparation and resultant mechanical testing allowed established composite mechanical theory for laminates to be applied to micron-sized bone volumes as described in Chapter 5. Laminate theory is particularly useful for bone as structural variations occur due to changes in the orientation of the mineralized collagen fibrils within the material. The relationship between the proposed bone structure from the literature and measured mechanical properties are further discussed in Chapter 6 where fracture mechanical properties of bone are considered.

The mechanical properties of bone are therefore tested directly and show that both the elastic and fracture properties vary with this (structural) fibre orientation. Understanding the material properties of bone can give a better

insight into the effect of the quality of bone in overall mechanical properties and in turn is applied to study the effect of disease on the quality of bone such as in the case of osteoporosis as discussed in Chapter 7. Osteoporosis is known to affect the overall structure of bone, and is related to a reduction in volume and therefore in bone quantity, but little is known on the effect it has on bone quality. The results of Chapter 7 demonstrate how a disruption in the stiffness vs. toughness balance in the basic unit of bone can compromise the mechanical properties of bone and increase bone fragility as in osteoporosis.

In summary, the aim of this work is to examine the mechanical properties of bone at length scales where the bone material itself can be considered as a composite material, at the sub-lamellar level.

The experimental methods used in order to examine the mechanical properties of bone at the sub-lamellar level include the isolation of discrete volumes of bone corresponding to this sub-lamellar unit via Focused Ion Beam (FIB) methods later to be mechanically tested using an *in situ* Atomic Force Microscope (AFM) while monitoring using Scanning Electron Microscope (SEM) as detailed in Chapter 3.

Flow charts of the experimental methods used are shown in Figure 1.5. For the purpose of this work four rat femora, three healthy and one osteoporotic were used. Bone samples were taken from 8 month old sprague dawley rats, the diaphysis of the femora for all four samples were isolated and stored wrapped in gauss soaked in Hank's Buffer solution.

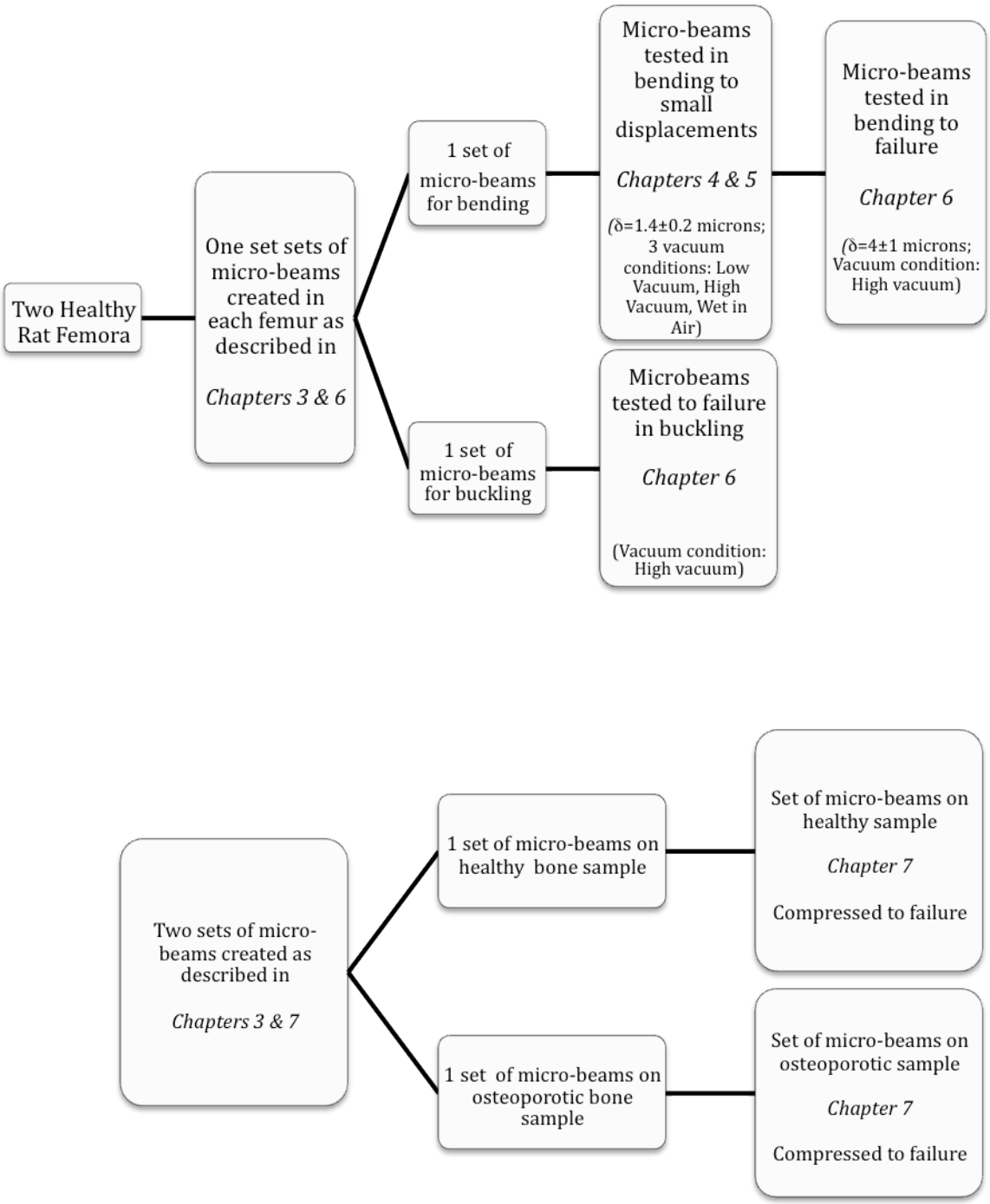

Figure 1.5 Flow charts of the testing conducted on each of the rat femora samples.

The rat femora were sliced into rectangles with dimensions of ~1x2x10 mm along the long axis of bone using a circular saw with constant water irrigation to prevent damage and later stored in 70% ethanol. The rectangular slices of bone were then dehydrated using solutions with increasing concentrations of ethanol in water as detailed in Chapter 3, Table 3.1. After dehydration, the rectangular slices were mounted on to a metal plate using an epoxy glue and gold coated for 30 seconds. Inside the SEM vacuum chamber, small discrete volumes of bone were isolated using FIB methods using parameters detailed in Chapter 3, Table 3.2. Care was taken in order to make sure that the rectangular slices were taken from the same place from each of the femora and that the FIB milling was done in similar locations across all samples.

Eight micro-beams were FIB milled on one of the healthy rat femora. Of these eight discrete volumes of bone, five were tested in bending to small displacements of ~1.4±0.2 μm in order to determine the elastic modulus of sub-lamellar bone units. Three of the five beams were tested in three different hydration conditions in order to determine the effect of the vacuum environment on the elastic mechanical properties of bone at this level as is detailed in Chapter 4, the other two were tested in high vacuum only. The structural effects of collagen fibril orientation on the elastic modulus in bone sub-lamellar units was analysed from the testing of these five micro-beams tested to small displacements as described in Chapter 5.

The bending mechanical testing was continued on the same eight micro-beams. This time, bending was done to failure in order to further understand the mechanical properties of bone at this level as described in Chapter 6. Only six of the eight micro-beams originally made were successfully tested in bending to failure. Eight more micro-beams were FIB milled on the second healthy rat bone femur. These new eight micro-beams were milled to be tested in buckling, only six of the eight beams were tested successfully as described in Chapter 6.

Final experiments were done on the third healthy rat femur and on the osteoporotic rat femur as to examine the mechanical properties of osteoporotic bone samples versus healthy samples at small scales. Compression tests were performed on similar discrete volumes of bone as the ones used for the bending tests in order to determine the effect of osteoporosis on bone mechanical properties at this level as described in Chapter 7. For the purpose of the compression tests eight micro-beams were milled on the healthy rat femur of which only five were successfully tests, while four micro-beams were milled and successfully tested on the osteoporotic rat femur.

This work uses small scale mechanical testing using AFM and SEM to determine the influence of structural organization, specifically collagen fibril orientation, and compositional changes induced by osteoporosis on resultant bone material behaviour by performing direct bending and compression mechanical tests on sub-lamellar units of bone.

Chapter 2. Bone as a natural composite material

2.1. Composites

2.1.1. General

Composites are materials that are made out of at least two materials. A composite is usually comprised of a reinforcing phase, often with a large aspect ratio as found in fibrous materials, embedded within another softer material referred to as the matrix material. The mechanical properties of a composite depend on a number of parameters including the volume fraction of the components, shape and orientation of the reinforcement, elastic properties of both components and the strength of the interface between components (Hull & Clyne 2001). A notable property of composite materials is their typical structural anisotropy when incorporating high aspect ratio reinforcements, which provide property variations when measured in different directions. Mechanical anisotropy is commonly encountered in fibre reinforced polymer composites when a stronger and stiffer fibrous reinforcing component is aligned preferentially in a particular direction, with mechanical properties deviating from the alignment axis (Hull & Clyne 2001).

The material properties of composites are not only defined by the orientation and distribution of reinforcement but also, critically, on the ability of the composite to share applied mechanical loads between the matrix and the reinforcement material. The proportion of the load carried by each

component in the composite is expected to be dependent on the proportion of composite volume occupied by reinforcement and matrix, with comparable load shared between the reinforcement and matrix based on their volume fraction in the composite.

Fibre architecture, describing the arrangement of the reinforcement in the composite, is an additional important parameter in defining the mechanical properties of composites. A number of fibre arrangements can be defined for the cylindrical geometries of fibres bound together in a surrounding matrix. For the simplest system of fibres aligned uniaxially in the composite, a lattice packing arrangement can be classified into two different types; hexagonal or square. Hexagonal packing is geometrically more efficient than square packing and, in theory, produce higher volume fractions of reinforcement in a composite. In practice, man-made composites are rarely within a hexagonal or square packing organization throughout the composite but can occur over small, localised regions. However, fibres aligned parallel to each other form an important composite classification known as unidirectional lamina (Hull & Clyne 2001).

Fibres arrange in pre-determined laminae layers of stacked fibres, they may be continuous or short and can be aligned in one direction or randomly. In order to simplify the study of laminates, each lamina is regarded as homogenous, meaning that the fibre arrangement and volume fraction are uniform throughout the layer. For definition purposes a ply is a unidirectional lamina and laminate is a stack of laminae. Two commonly

found stacking sequences are the cross-ply laminate and the angle-ply laminate. The cross-ply describes a laminate with alternating plies; each ply having fibres orientated 90° to each other. The second angle-ply describes a laminate stacking arrangement where each ply has fibres that orientated 60° of each other (Hull & Clyne 2001).

The axial elastic behaviour of a fibre reinforced composites can be simplified by treating the materials as two components bonded together, with thickness relative to the volume fraction of the matrix and fibre. The two slabs of material are constrained to have the same lengths parallel to the bonded interface and hence if a stress is applied along the fibre alignment both components exhibit the same strain along the same direction. This configuration is called the "equal strain" condition and valid for loading along the fibre axis providing there is no interfacial sliding between the fibre and matrix. Such a simplification allows the elastic modulus of the composite to be derived and can be summarized using the "Rule of Mixtures" shown in Equation 1 where the stiffness of the composite is a volume mean between the moduli of the two components.

$$E = E_f c_f + E_m c_m \qquad \text{Eqn. 1}$$

Where E is the overall elastic modulus of the composite, E_f is the elastic modulus of the fibre, E_m is the elastic modulus of the matrix, c_f is the volume fraction of the fibres and c_m is the volume fraction of the matrix. The "Rule of Mixtures" is considered to have a high degree of precision as long as the fibres are long enough for the "equal strain" assumption to apply. The equal

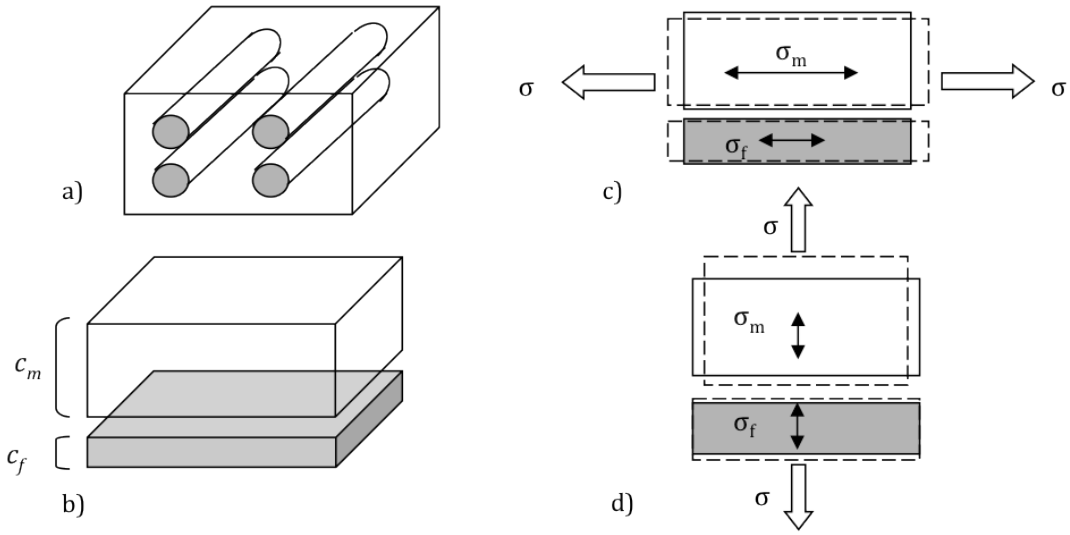

Figure 2.1 Schematic diagrams of a) a fibre composite b) the "slab model" used to represent composite materials in terms of volume fraction where c_f describes the volume fraction of the fibres and c_m describes the volume fraction of the matrix c) schematic of the Voigt model and d) the Reuss model. The white arrows represent the stresses, σ, applied to the composite and the black arrows represent the stresses transferred to each of the components. The dotted lines represent the deformation experience by each component.

strain treatment is often described as the "Voigt model" as shown in Figure 2.1 c). Even though the "Rule of Mixtures" equation has been shown to work for many composites with continuous fibres, there are minor deviations due to stresses that arise when the Poisson's ratios of the two components are not equal as will be explained later and shown in Figure 2.2 (Hull & Clyne 2001).

The Voigt model is sufficient to describe a continuous reinforcement aligned in the direction of the applied load and can be considered as an upper limit when describing the elastic modulus of the composite material using

Equation 1. Consequently, a lower limit on the elastic modulus of a composite can be determined from transverse stiffness. The simplest approach to define a lower limit for elastic behaviour is to represent the two components of reinforcement and matrix in the composite by the "slab model" explained previously and shown in Figure 2.1 a). A load applied orthogonally to the plane of the slabs will now produce variations in reinforcement and matrix phase strains, while each of these phases will be under an equal stress. This "equal stress" model is often called a "Reuss model" and can be used to calculate the elastic modulus of a composite using:

$$E = \left[\frac{c_f}{E_f} + \frac{c_m}{E_m} \right]^{-1} \qquad \text{Eqn. 2}$$

The strain and therefore stress produced when loading the fibres transversely is distributed in-homogenously within the matrix as opposed to when the fibres are loaded axially as shown in Figure 2.1 d). The in-homogeneity causes sharp concentrations of stress in specific regions around the reinforcing fibres which could lead to interfacial de-bonding, matrix plastic deformation and micro-cracking (Hull & Clyne 2001). This non-uniform distribution of stress and strain in transverse loading means that the "equal stress" model is often inadequate, giving an underestimate of the elastic modulus and can be treated as a lower boundary condition when calculating elastic properties of composites (Hull & Clyne 2001).

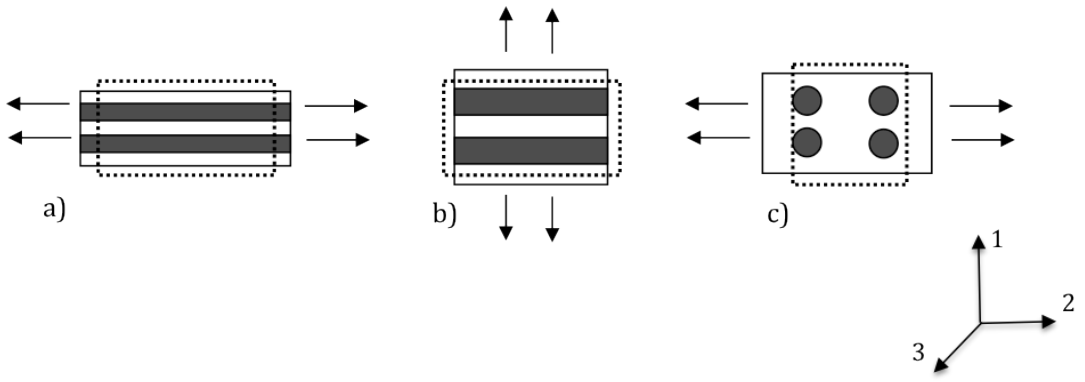

Figure 2.2 Schematic diagram, showing the effect of Poisson's ratio on fibre composites loaded in different directions: a) a load along the principal fibre axis leads to equal to applied strains but unequal Poisson strains; b) a load across of the fibres leads to unequal applied strains but equal Poisson strains; c) a load transverse of the fibres leads to unequal applied strains and unequal Poisson strains. Dotted boxes represent state of composite before loading.

The limits of the accuracy of the Voigt and Reuss models are due to the effect of the Poisson's ratio as the composite is loaded. The Poisson's ratio contraction effect is described by the matrix strain in the transverse direction caused by an axial stress. An aligned fibre composite has three different Poisson's ratios as shown in Figure 2.2. The first Poisson's ratio shown in Figure 2.2 a) describes how applying a load along the principal fibre axis leads to equal applied strains but to unequal Poisson strains. The second Poisson's ratio condition in Figure 2.2 b) describes how applying a load across of the fibres leads to unequal applied strains but equal Poisson strains and the third condition describes how applying a load transverse of the fibres as shown in Figure 2.2 c) leads to unequal applied strains and unequal Poisson strains.

Poisson's ratio can be described therefore by the following equations:

$$\nu_{ij} = -\frac{\varepsilon_j}{\varepsilon_i} \qquad \text{Eqn. 3}$$

$$\frac{\nu_{12}}{E_1} = \frac{\nu_{21}}{E_2} \qquad \text{Eqn. 4}$$

$$G_{23} = \frac{E_2}{2(1+\nu_{23})} \qquad \text{Eqn. 5}$$

Where ν_{ij} is the Poisson's ratio, where the *i*-direction is the direction at which the stress is applied and the *j*-direction is the direction of the deformation caused by the load in the *i*-direction; ε_i is the strain within the plane, ε_j is the strain normal to the plane, E is the elastic modulus and G is the shear modulus.

Using the slab model to estimate the Poisson's ratio value is unsuitable due to the fact that the contractions of the two components must match. Although all three Poisson's ratios can be identified using the slab model, the only calculation is for ν_{12} as the Poisson strains for the two components can be evaluated independently and summed. Therefore for long fibre composites in axial stress:

$$\nu_{12} = -\frac{\varepsilon_2}{\varepsilon_1} c_f \nu_f + (1 - c_f)\nu_m \qquad \text{Eqn. 6}$$

Where ν_f being the Poisson's ratio of the fibre and ν_m the Poisson's ratio of the matrix.

A fairly valid prediction for the other two ratios, as the long fibre composite is stressed transversely causing axial contraction to the transverse extension can be derived from Equation 4 so that:

$$\nu_{21} = \left[c_f \nu_f + (1 - c_f)\nu_m\right]\frac{E_2}{E_1} \qquad \text{Eqn. 7}$$

And

$$\nu_{23} = 1 - \nu_{21} - \frac{E_2}{3K} \qquad \text{Eqn. 8}$$

where K is the bulk modulus of the composite. In order to estimate the bulk modulus of the composite an equal stress assumption can be used where:

$$\sigma_H = \Delta_f K_f = \Delta_m K_m \qquad \text{Eqn. 9}$$

and $$\Delta = c_f \Delta_f + (1 - c_f)\Delta_m \qquad \text{Eqn.10}$$

hence $$K = \frac{\sigma_H}{\Delta} = \left[\frac{c_f}{K_f} + \frac{(1 - c_f)}{K_m}\right]^{-1} \qquad \text{Eqn.11}$$

The bulk moduli of the components can be related to the other elastic constants as follows:

$$K_f = \frac{E_f}{3(1 - 2\nu_f)} \qquad \text{Eqn. 12}$$

Where σ_H is the applied hydrostatic stress, K_f is the bulk modulus of the fibre, K_m is the bulk modulus of the matrix and Δ is the overall volume change of the composite material due to the volume change of the fibre, Δ_f , and the matrix, Δ_m.

More accurate models used to calculate the elastic modulus of a composite have improved on the simply Reuss and Voigt analysis by including reinforcement orientation parameters as proposed by the Halpin and Tsai model (Halpin & Kardos 1976; Hull & Clyne 2001). Halpin-Tsai theory is a micromechanics relationship for the composite analogy of semi-crystalline polymers. The theory describes the reinforcing behaviour of reinforcing fillers in composite materials by considering both the volume fraction and, importantly, the alignment and the aspect ratio of the reinforcement (such as fibres) relative to the loading conditions. Halpin-Tsai equations predict and accurately correlate with experimental results to show how increasing the aspect ratio of a fibre increases overall composite stiffness by up to an order of magnitude and how the progression of a fibre to a tape or platelet also results in an order of magnitude increase in stiffness (Halpin & Kardos 1976) using:

$$E_1 = c_f E_f + c_m E_m \qquad \text{Eqn. 13}$$

$$E_2 = \frac{E_m\left(1 + \xi\eta c_f\right)}{1 - \eta c_f} \qquad \text{Eqn. 14}$$

Where

$$\eta = \frac{\frac{E_f}{E_m} - 1}{\frac{E_f}{E_m} + \xi} \qquad \text{Eqn. 15}$$

E_f is the elastic modulus of the fibre, E_m is the elastic modulus of the matrix, c_f is the volume fraction of the filler, c_m is the volume fraction of the matrix and ξ is an adjustable parameter according to the geometry factor of the transverse modulus, the shear modulus and the Poisson's ratio of the composite material as well as a function of the fibre geometry, their packing arrangement and loading conditions. ξ is determined by elasticity solutions and by fitting η to mechanical testing results (Hull & Clyne 2001).

The shear modulus of a composite can also be represented using the slab model and described by Halpin-Tsai model by considering the net shear strain produced when a shear stress is applied to the composite and the individual displacement from the two components. Neither the "equal stress" nor "equal strain" conditions are close to the actual conditions of a fibre composite in shear. Halpin-Tsai semi-empirical expressions are therefore used as follows:

$$G_{12} = \frac{G_m\left(1 + \xi\eta c_f\right)}{1 - \eta c_f} \qquad \text{Eqn. 16}$$

Where

$$\eta = \frac{\frac{G_f}{G_m} - 1}{\frac{G_f}{G_m} + \xi} \qquad \text{Eqn. 17}$$

The Halpin-Tsai expression has been shown to be accurate in calculating the axial shear modulus (G_{12}) as opposed to the slab model or the Eshelby model (Hull & Clyne 2001).

The Poisson's ratio of the composite can be defined as:

$$\nu_{12} = c_f \nu_f + c_m \nu_m \qquad \text{Eqn. 18}$$

$$\nu_{23} = \frac{\nu_{23}\left(1 + \xi \eta c_f\right)}{1 - \eta c_f} \qquad \text{Eqn. 19}$$

2.1.2. Laminates

Laminate composites describe a sequence of stacked and bound sheets of a composite material with different fibre arrangement within each lamina. These types of composites are useful for applications where there is an equal distribution of stresses along all the directions. A laminate, as opposed to a random fibre mat, allows higher fibre volume fractions of fibres aligned in different and specific directions and is therefore useful for the effective transfer of loads in different directions (Hull & Clyne 2001). The composite mechanics theories of Voigt, Reuss and Halpin-Tsai are therefore also critical in describing the mechanical properties of composite structure laminates containing arranged fibrous reinforcements but can additionally predict mechanical behaviour in materials that approximate to laminate structures, such as bone material.

2.1.3. Bone as a composite

Biological tissues such as wood, bone and shell can be considered fibre composites with a hierarchical structure. Bone is notable as appearing to have a high volume fraction of fibrous material. As can be seen in Figure 1.2, the fracture surface of bone is similar to the fracture surface of a man made fibrous composite material. However, being alive, biological composite materials have the ability to grow and remodel depending on the need to adapt to its environment and ultimately heal or self-repair. As with man-made composite materials, these natural composites are optimised for a particular purpose. In terms of mechanical properties, the main function of bone is to provide protection and support for the organism (Fratzl & Weinkamer 2007).

In order to further understand the mechanical properties of bone, different composite models have been used with different approaches. The simplest approach proposed by Currey (2002) is the use of a rule of mixtures in order to describe the mechanical properties of bone observed experimentally. Akiva et al. (1998) extended the work of Currey (2002) to apply the Halpin-Tsai model in order to incorporate the effect of the orientation of the mineralized collagen fibrils into the composite model in order to address bone's well-established mechanical anisotropy Akiva et al. (1998) measured using indentation. Jäger and Fratzl (2000) further improve the Wagner and Weiner (1992), Akiva et al. (1998) model (Wagner & Weiner 1992; Akiva, Wagner & Weiner 1998) by introducing the effect of the staggered

arrangement of mineral particles and distribution of the gaps in the collagen fibril in bone which was previously ignored in the parallel array of mineral platelets model of Weiner and Akiva. Jäger and Fratzl (2000) insist that this last model can predict the dependence of stiffness and fracture load on the volume fraction and spacing of mineral particles as seen experimentally. However, this last model only considers the structure of the mineralized collagen fibril and fails to model the influence of orientation in higher hierarchical structures such as in bone lamellae (Jäger & Fratzl 2000). Although the model by Wagner, Weiner and Akiva assumes details such as the thickness of the mineral platelet and considers a parallel array of mineral platelets, it gives a better fit of bone mechanical properties at higher hierarchical levels by considering the mineralized collagen orientation. This fit will be further discussed in Chapter 5 which focuses on the effect of mineralized collagen orientation on the mechanical properties of isolated bone lamellae and demonstrates how the Akiva model is accurate enough to predict mechanical bone behaviour due to mineralized collagen orientation.

Considering the three models presented above, the difficulties in describing bone mechanics become obvious as the structure of bone is more complex than a man-made composite. A range of different issues need to be considered in natural composites such as the properties of individual components, their interaction while mechanically loaded and how these components then assemble in order to create the different structures across all of the different hierarchical levels. Thus, the different hierarchical levels of bone have unique structural organizations that will be discussed in detail

in the next few sections. Importantly, each hierarchical level is composed of a different laminar arrangement. The next section will describe how these laminar arrangements aggregate in order to form the structure of bone.

2.2. Structure of bone

Bone is a complex material with distinct structural features over varying length scales. The structure of bone across these length scales defines the overall mechanical behaviour but, due to the complexity of bone structure, structure-function relationships are poorly understood. The following sections will describe the structure of bone at different lengths scales and will review the literature on its mechanical properties. Figure 2.3 below gives a general overview of the main structural features of bone.

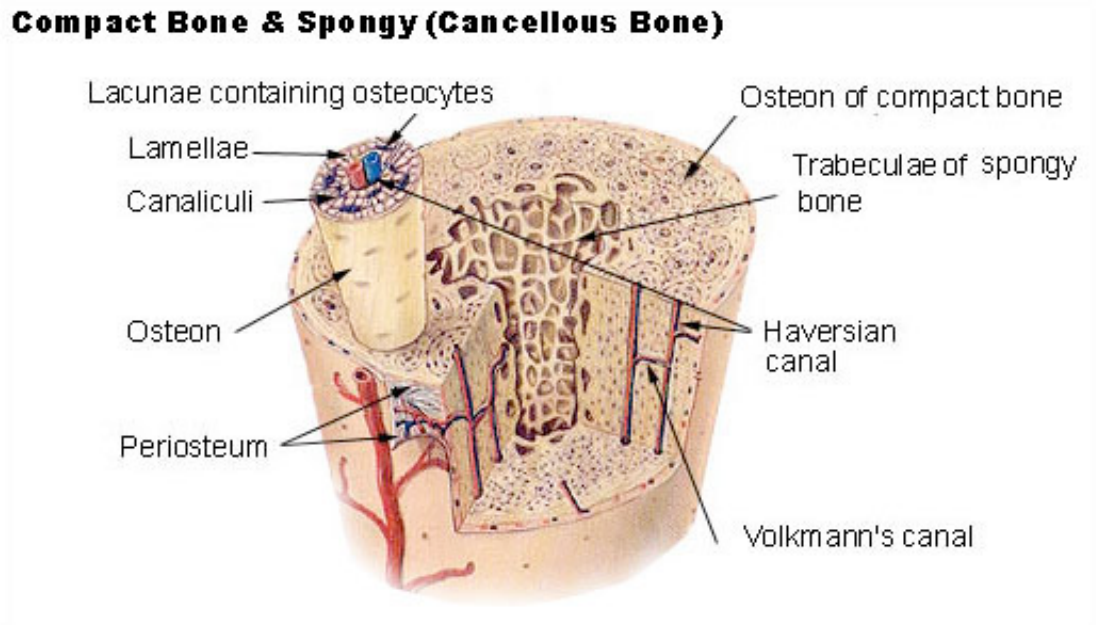

Figure 2.3 The structure of bone and its main structural features. (National Cancer Institute's SEER Program 2011) used in accordance with the fair use policy.

2.2.1. General properties of bone

Bone plays an important role in mechanical, biological and chemical functions, providing structural support, protection, and a reservoir of cells and mineral ions to sustain homeostasis (Rho, Kuhn-Spearing & Zioupos 1998). Bone varies with age, gender, anatomical location and between species; and within these different categories it performs tailored functions accordingly. Generally, bone consists of four main components: fibrous collagen, non-collagenous protein, nanoparticulate hydroxyapatite, and water. The resultant combination of these four main components form a natural composite that grows in complexity across a number of different length scales. The structural complexity allows bone to have a number of biological functions while sustaining required mechanical functions. As

opposed to typical man-made materials, cells are responsible for the formation and re-sorption of bone structure with the resultant biological function and the constant relocation, removal and re-deposition of material occurring due to physiological requirements. Bone materials are therefore structurally dynamic when compared to man-made materials.

2.2.2. Hierarchical structure

Five main hierarchical levels exist in bone from the smallest to the largest length scales, defined respectively as the ultrastructure (nanostructure: collagen fibrils, NCPs, mineral platelets), the sub-microstructure (lamellar level) the microstructure (osteonal or trabecular level), the architectural (tissue level), and the macrostructure (whole bone). These hierarchical levels are illustrated in Table 2.1 below.

Table 2.1 clearly shows a diversity of distinct structures operating at length scales ranging from nanometres towards centimetres. Each structural level can therefore be discussed independently.

Table 2.1 – The hierarchical levels of bone (Weinkamer & Fratzl 2011) used with permission from the publisher (Gould 2009) used in accordance to the fair use policy.

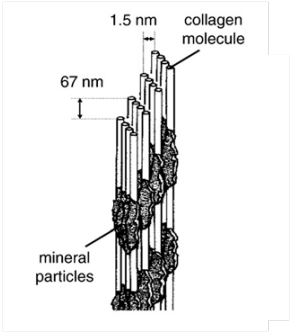	Ultrastructure (Collagen fibrils)	<1μm
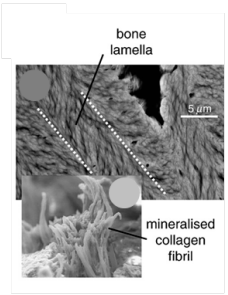	Sub-microstructure (Lamellar unit)	1-5μm
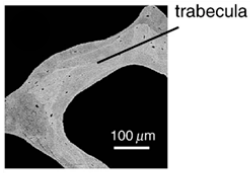 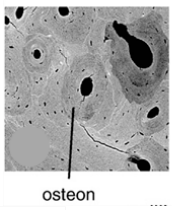	Microstructure (Primary and Secondary Osteons)	20-300 μm
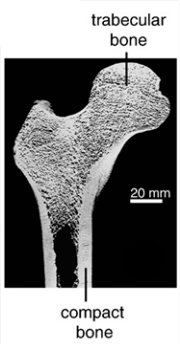	Architectural (Tissue level)	1-750mm
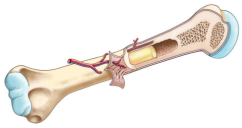	Macrostructure (Whole bone) (Gould 2009)	>1cm

2.2.2.1. Ultrastructure

The ultrastructure level refers to length scales of the order of nanometres. Collagen is the most frequently encountered protein in bone and is mainly composed of Type I collagen and consists of protein molecules called tropocollagen. Other types of collagen such as Type II, III, and V collagen can be found in growth plates and during bone formation (Bornstein & Sage 1980). The formation of discrete structures in bone is defined by the aggregation of collagen. Specifically, tropocollagen molecules self-assemble on ribosome inside the cell and aggregate to form fibrous microfibrils consisting of three polypeptides of the same length, of which two have the same amino acid composition. The three chains are held together by hydrogen bonds in a left-handed triple helix. The arrangement of the tropocollagen molecules within a collagen microfibril is a staggered pattern occurring at one fourth of the tropocollagen length, known as the quarter-staggered model (Hodge 1989), as shown in Figure 2.4. The gap between the ends of the tropocollagen molecules is called the hole region and is approximately 67 nanometres long. The microfibrils are held and stabilized by intermolecular cross-linking (Currey 2002).

Collagen microfibrils are perhaps unique in that they exhibit a crystalline structure, unlike most proteins, but do not aggregate or behave as such. Two main contradictions exist in the observable roundness of the collagen microfibril and their growth from paraboidal tips as the collagen microfibrils with an apparent crystalline structure should not allow for these two

observations (Prockop & Fertala 1998). Ramachandran (1967) has addressed before these two issues in 1967 and suggested a cylindrical structure where the tropocollagen monomers were orientated in a spiral formation (Ramachandran 1967). Galloway (1985) further explained that the monomers were in cylindrical arrays and the outer layers develop into lattice-like structures that allow packing of some of the monomers in a quasi-hexagonal unit cells (Galloway 1985). Prockop and Fertala (1998) continues to explain that both models are insufficient although not incorrect and suggests that the structure has specific binding sites on the collagen monomer that direct the self-assembly of the monomers into fibrils. The entropy-driven process that Prockop and Fertala (1998) describes resembles crystallization giving collagen microfibrils properties of both a crystalline structure and a liquid crystal. Within the collagen microfibrils there may be both crystalline areas and more flexible liquid like regions; the degree of crystallinity varying with changes in temperature, tension and other conditions (Prockop & Fertala 1998).

In any small volume of bone, the collagen microfibrils are approximately parallel in organization. Crystals of apatite both surrounded and are found within the fibrils. This apatite mineral present in bone is more accurately termed a calcium phosphate $Ca_{10}(PO_4)_6(OH)_2$ known as hydroxyapatite in the form of crystal units found throughout bone structures (Currey 2002). Hydroxyapatite mineral contains impurities, predominatly the presence of carbonate groups that make the mineral overall a carbonate apatite. The impurities reduce the mineral crystallinity and are mainly found around the

edges of the bone near the vascular and marrow spaces (Ou-Yang et al. 2001). The exact morphology of the hydroxyapatite mineral is controversial. However, two different models are generally proposed to describe the shape of the apatite crystals being either needle shaped (Ascenzi et al. 1978) or platelet shaped (Landis et al. 1993; Landis et al. 1996). The main reason for this dispute is that high-resolution electron microscopy can only observe crystals in 2D and some experimental preparations have a damaging effect, which changes the composition and structure of the crystals. In vivo, the crystals are in wet conditions yet typical electron microscopy analysis of crystals requires a vacuum. Since the crystals are reactive to their environment, due to their size and high surface area to volume ratio, changing the environmental conditions most probably will have an effect on the mineral crystal morphology (Currey 2002).

Wagermaier et al. (2007) were able to overcome one of the issues associated with TEM observation and obtained three-dimensional orientation distribution of the crystallographic c-axis at sub-lamellar resolution by scanning texture analysis of lamellar bone using micro-beam synchrotron x-ray radiation (Wagermaier et al. 2007). This work correlated with previous 3D TEM work and indicated a platelet mineral geometry of hexagonal crystal symmetry, with the plate long axis aligned along the collagen fibrillar direction (Landis et al. 1996; Fratzl et al. 2004; Wagermaier et al. 2007).

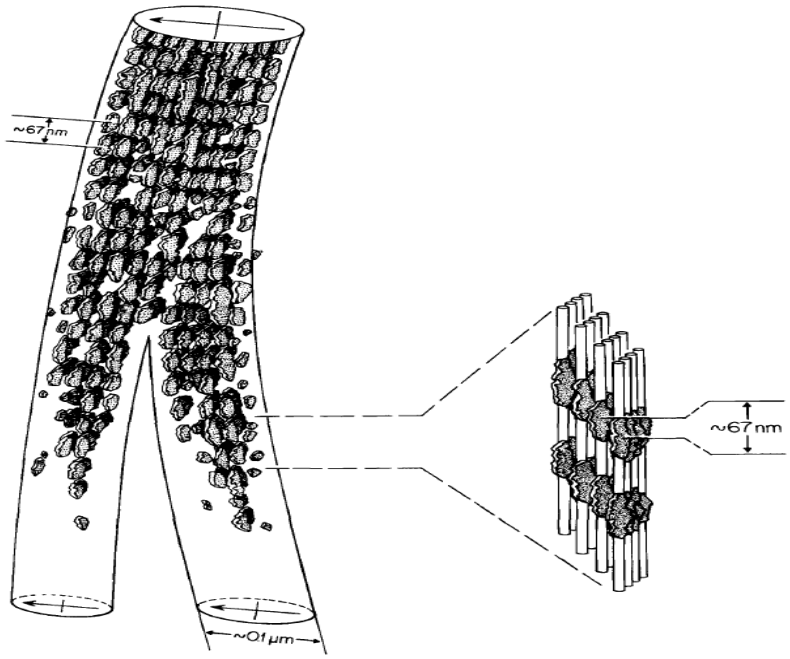

Figure 2.4 Schematic diagram showing the organization of mineral phase within collagen fibrils found in mineralized turkey tendon which is often used to represent the structure of bone material (Landis et al. 1996) used with permission from the publisher.

The geometry of the mineral plates has been identified accurately using x-ray (Bonar et al. 1983; Grynpas, Bonar & Glimcher 1984), TEM techniques (Landis et al. 1996; Prostak & Lees 1996) and AFM (Eppell et al. 2001) and are 1-8 nm thick, 10-80 nm wide and around 15-100 nm long. The observed size variation in the mineral platelets is due to the different analysis techniques ranging from X-ray diffraction (XRD), back scattering electron imaging (BSEI), scanning electron microscopy (SEM), transmission electron microscopy (TEM) and most recently AFM which characterized the crystals to be in the smallest range 12x10x1 nm (Rubin et al. 2003).

Landis et al. (1996) describes the mineral apatite crystals to be continuously distributed along a collagen fibril as shown in Figure 2.4, with their size and number increasing in a tapered fashion from a relatively narrow tip containing smaller and infrequent crystals to wider regions having more densely packed, larger crystals (Landis et al. 1996). The mineral plates are oriented with their long axes parallel to the direction of the adjacent collagen fibril. The crystals are found within and around the collagen fibrils. The arrangement is periodical along the fibrils and corresponds to the collagen hole and overlap zones which have a 67 nm repeat distance as shown in Figure 2.4 (Wainwright et al. 1982; Landis et al. 1996). The arrangement of the collagen molecules most probably helps the nucleation of the mineral crystals. The process of mineralization will be explained in following sections.

Non-collagenous proteins (NCPs) refer to the minor protein content in bone (An & Draughn 2000) representing about 10% of the organic component in bone (Roach 1994). The two major NCPs are sialoprotein and osteopontin and generally accumulate in cement lines and in the spaces between the mineralized collagen fibrils (Nanci 1999). The amount of NCPs has been correlated to the type of bone tissue, cementum types, speed of formation and packing density of collagen fibrils (Nanci 1999). NCPs control and initiate bone re-sorption and formation as they are involved in cell signalling, cell attachment, collagen fibrillogenesis and mineralization. The importance of NCPs is not only related to bone mechanical properties but also on cell

signalling and mineralization, which directly affects bone structure organization. The effect of NCPs on mineralization will be further discussed.

2.2.2.2. Sub-microstructure

Mineralized collagen fibrils aggregate and organize into different arrangements forming a higher structural level called the sub-microstructure level. Bone at the sub-microstructure level can be broadly classified into two basic types of bone, woven and lamellar, depending on the level of organization of the mineralized collagen fibrils. This work is particularly focussed on the sub-microstructural level as mechanical properties will be determined by bone material behaviour. Therefore, bone at the material level only exists in woven or lamellar form.

2.2.2.2.1 Woven bone

Woven bone unlike lamellar bone has randomly orientated mineralized collagen fibrils. Woven bone is laid down quickly by the osteoblasts and is usually found on young bone such as foetal and callus as a fracture repairs. Collagen in woven bone is thinner; fibrils are 0.1-3 μm in diameter and are orientated randomly resulting in a less dense bone. Crystals of hydroxyapatite are also randomly arranged and the mineralization process leaves mineral free spaces, and therefore a porous structure at the microstructure level. The cells in woven bone are sub-spherical unlike those in lamellar bone (Currey 2002). Woven bone can be deposited without

previous pre-existing structure such as hard tissue or cartilage and provides a fast, sufficiently strong framework to maintain bone function (An & Draughn 2000; Currey 2002; Boyd & Nigg 2007). Woven bone is later transformed into a more organized system, commonly known as primary lamellar bone.

2.2.2.2.2 Lamellar bone

Lamellar bone on the other hand is produced more slowly than woven bone and in turn is neatly arranged into regular layers. These layers are called lamellae and are thought to aggregate in domains of 30-100 μm with fibril orientation changing between domains. Collagen fibres in lamellar bone form branching bundles, 2-3 μm in diameter and have higher content of amorphous calcium phosphate and a higher mineral to organic content ratio. Overall lamellar bone is less mineralized than woven bone at the final degree of mineralization (Wainwright et al. 1982; Currey 2002). Lamellar bone is arranged in a repeating pattern, with each repeating unit called a lamellar unit. The lamellar unit in bone is a common feature at the micron level and can be considered the building block of cortical bone (Gupta, Stachewicz & Wagermaier 2006). The thickness of the lamellae varies but is usually found to be 5 μm on average. In long bones, the lamellae usually run along the length of the long axis of bone and rarely have their 5 μm short axis running parallel to this long axis (Wainwright et al. 1982).

The model of the lamellar unit of bone currently accepted was suggested by Weiner (1999) and Wagner (1998) but was effectively considered earlier by Giraud-Guille (1988) when describing a twisted or rotated plywood model, otherwise known as the helicoidal structure (Giraud-Guille 1988; Weiner, Traub & Wagner 1999). The helicoidal description is important and allows the organization of the components of bone to be related to synthetic fibre composite laminates and resultant composite theory described at the beginning of the chapter. This helicoidal model of bone has been more recently proven by Wagermaier (Wagermaier et al. 2006; Wagermaier et al. 2007) by measuring the variation in orientation of the fibril with a special resolution of 1 μm using a novel synchrotron x-ray texture measurement method. The helicoidal structure describes lamellae arranged in different layers with fibres pointing all in the same direction within each layer. These types of helicoidal arrangements can also be found in other biological structures such as insect cuticles, plant cell walls, wood etc. (Currey 2002; Fratzl & Weinkamer 2007).

The plywood model explains how the lamellar unit is composed of five subunits, with each subunit composed of an array of aligned mineralized collagen fibrils. The orientation of the sublayers show a rotated plywood-like structure with a 30 degree angle variation from one sublayer to the other (Weiner, Traub & Wagner 1999) as shown in Figure 2.5 below. The plywood model was theorized and proven by Weiner (Weiner, Traub & Wagner 1999),

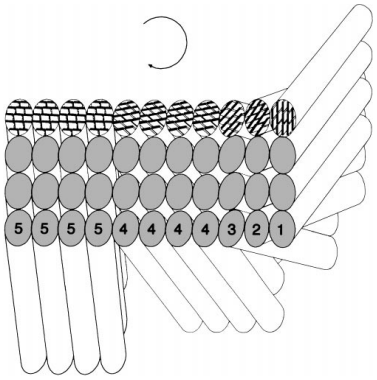

Figure 2.5 Schematic diagram of a lamellar unit showing the plywood structure of five fibril bundle sheets with 30° orientation steps (Weiner, Traub & Wagner 1999) used with permission from the publisher.

Marotti (Marotti 1993), Liu (Liu, Weiner & Wagner 1999), Xu (Xu et al. 2003)and Gupta (Gupta, Stachewicz & Wagermaier 2006) using as organization where the lamellar unit can be divided into two subunits; the 'thick' and the 'thin' subunit as shown in Figure 2.5. The 'thick' sub-lamellar units are around 4 μm thick and the minerals usually have their long axis parallel to the long axis of bone (Wainwright et al. 1982; Currey 2002). This larger proportion of fibres orientated along the long axis of bone is reflected in an increased elastic modulus along the long axis direction. The 'thin' lamella is around 1 μm thick and has the mineral oriented normal to the long axis of the bone. The 'thin' lamella also has a lower mineral content (Marotti 1993; Gupta, Stachewicz & Wagermaier 2006). Weiner comments on the polarized light images taken by Riggs who explains that the osteoblasts could be receiving strain signals to vary the structure by varying the thickness of the sub-layers (Riggs et al. 1993; Weiner, Traub & Wagner 1999). Weiner stresses his opinion by adding that he has seen a variation in thickness of

each sub-layer in different animals who inherently have different adaptation needs (Weiner, Traub & Wagner 1999).

Bone material can exhibit a number of different lamellar arrangements but are grouped into woven bone, primary lamellar bone, fibrolamellar, primary osteon and secondary osteon bone. These lamellar arrangements can be seen in Figure 2.6 below. The lamellar arrangement correlates to the speed at which a particular bone has to be produced and therefore different types of arrangements are found in different anatomical locations in bone (Currey 2002).

Primary lamellar bone or circumferential lamellar bone is composed of lamellae sheets oriented parallel to the long axis of bone around the endosteal and periosteal circumference of bone. Primary lamellar bone is associated with marrow and vascular tissue such as that found around trabeculae and in the epiphyses of long bones. The proximity to the vascular tissues allows for the rapid exchange of calcium between bone and serum and could explain why regions of cancellous bone are the first to exhibit osteopenia or reduced bone mass. The mechanical properties of primary lamellar bone are physiologically sufficient but calcium homeostasis is critical and may override the mechanical requirements (Boyd & Nigg 2007).

Plexiform or fibrolamellar is similar to primary lamellar bone as it is deposited on pre-existing surfaces. Fibrolamellar bone is produced rapidly as with woven bone but without compromising the mechanical properties. Plexiform bone has similar morphology to that of highly oriented cancellous

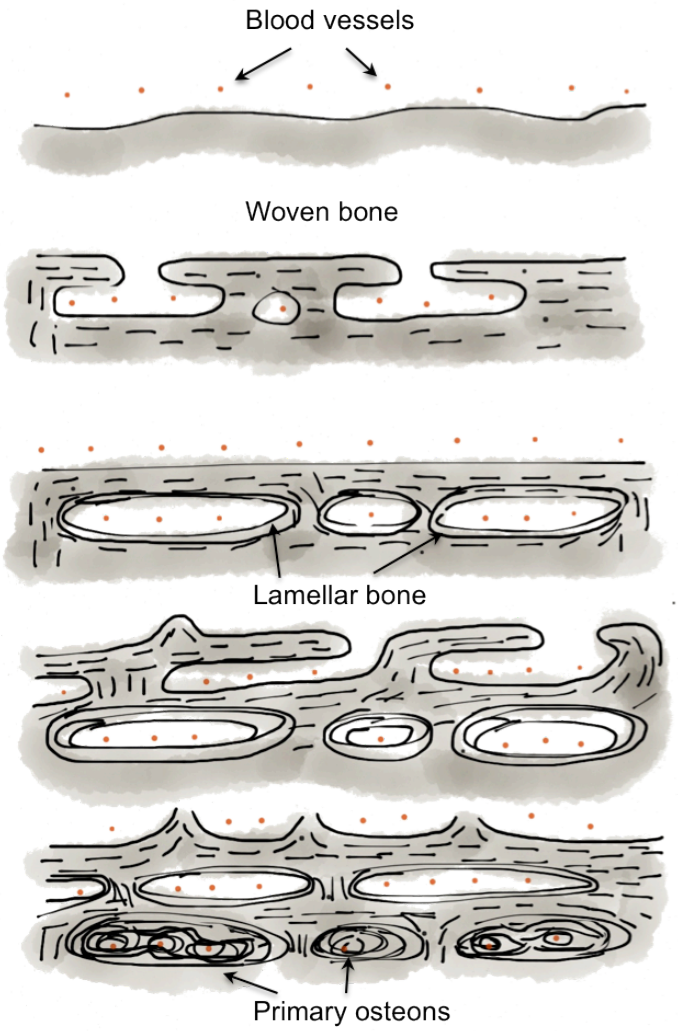

Figure 2.6 Different types of lamellar arrangements and their role in bone development. Bone starts by enveloping the blood vessels with quickly laid, randomly orientated material known as woven bone. As it continues to grow, bone is resorbed and produced more slowly so that organized lamellar bone is formed. Lamellar bone continues to be redeposited around the blood vessels into what is referred to as Primary osteons. Figure was inspired by Currey (2002).

bone and is a combination of alternating layers of parallel-fibered or woven bone and lamellar bone tissue. This type of bone is usually found in rapidly growing large animals (such as cows and horses) as the rapid growth demands mechanical competence (Boyd & Nigg 2007).

2.2.2.3. Microstructure

The primary lamellar bone material is able to change its structure by the action of cellular activity, referred to as remodelling, into more complex structures known as either primary osteons or secondary osteons depending on the structural requirements. Primary osteons develop through the sequential filling of vascular channels with layers of lamellar bone. The lamellae are arranged in concentric rings around a vascular channel. Primary osteons are found in thick trabeculae, which is also a well-organized primary lamellar bone as will be discussed later (An & Draughn 2000).

Secondary osteons are found mainly in cortical bone and occur as the result of bone material being resorbed and remodelled by cells. Secondary osteons are approximately 300 μm in diameter, 3 to 5 mm in length with their long axes parallel to the long axes of long bones. The cells resorb around the blood vessels and form elongated cavities filled with lamellar bone surrounding the blood channel, resulting in cylindrical laminated structures called osteons with Haversian canals running through the middle. The Haversian canals hold blood, nerve and lymph networks to supply bone cells. Further fluid transport for the distribution of nutrients to osteocytes sitting inside lacunae is achieved from canaliculi, which are small fluid-filled channels within the lamellae that radiate from the Haversian canals (Wainwright et al. 1982; Boyd & Nigg 2007). The distinguishing feature of secondary osteons are the presence of cement lines which separate osteons from surrounding bone

matrix such as interstitial bone or primary lamellar bone (Currey 2002; Boyd & Nigg 2007).

The outer layer of the osteon in secondary osteon bone is compositionally different to the bulk osteon and is called the 'cement line'. Cement lines are thin layers of calcified mucopolysaccharides lacking collagen. Cement lines form when the 'cutting cone' of the osteoclast stops its activity and before lamellar bone is laid down. The mechanical properties of cement lines are not fully understood as they are difficult to isolate, with researchers indicating that the cement line region is either highly mineralized or poorly mineralized but generally accepted as being deficient in collagen (Wainwright et al. 1982). Given that less canaliculi crosses the cement lines, the osteons are partially sealed from one another and could have an effect on the body's metabolism and cell survival (Wainwright et al. 1982; Currey 2002).

Four types of osteons have been previously identified by the different light patterns observed using optical polarized microscope images as shown in Figure 2.7. Longitudinal osteons with the collagen orientated along the long axis of bone can be identified as 'dark' under polarized light. Transverse osteons with collagen orientated perpendicular along the long axis of bone are typically shown as 'bright'. Alternating osteons, which have alternating lamellae sheets of longitudinal and transverse collagen orientations, exhibit intermittent 'bright' and 'dark' rings. Finally, hoop osteons contain collagen orientated longitudinally with an outer most ring of collagen orientated

transversely and therefore appear as 'dark' with a 'bright' ring on the outside of the osteon in polarized light microscopy. Thus, the brightness difference observed in polarized light microscopy is dependent on the arrangement of collagen fibrils in successive lamellae. The corresponding mechanical properties of the different types of osteons have been examined (Ascenzi & Bonucci 1972; Ascenzi & Bonucci 1976; Martin et al. 1996; Ascenzi et al. 2003; Bigley et al. 2006). The mechanical properties of each osteon type are critically dependent on the different orientations of the collagen fibrils within each lamellae and the arrangement around secondary osteons, which is the topic of future sections. The classic model of Gebhardt (1906) explains the optical pattern of osteons by assuming that the collagen fibrils have a helical course around the osteon axis, and that fibrils which have the same helical orientation form a lamella. The fibril course in one lamella is opposite and approximately perpendicular to the course in the adjacent lamellae (Gebhardt 1906). The plywood model as shown above suggests that the variation in the lamellar patterns in osteons depend partly on the direction of the section plane and that the lamellae derive from the arrangement of the fibrils according to either a 'cylindrical twisted plywood' pattern or 'cylindrical orthogonal plywood' which may coexist in the same osteon. Both these fibrillar arrangements will be discussed in the next hierarchical level. Scanning electron microscopy (SEM) images observed by Marotti (1993) show alternating collagen-rich and collagen-poor, or what he refers to as dense and loose lamellae respectively. The collagen-dense lamellae appear thinner than the collagen-poor. Under polarized ligh microscopy the

collagen-rich or dense lamellae appear bright and correspond to the tranverse lamellae, while collagen-poor or loose lamellae appear as dark and correspond to the longitudinal lamellae (Marotti 1993). The relative width of the two types of lamellae observed by Marotti (1993) agrees with other research which describe 'thick' and 'thin' lamellar subunits, with the 'thick' subunit oriented longitudinally and the 'thin' orientated transversely (Ascenzi, Benvenuti & Bonucci 1982; Liu, Weiner & Wagner 1999; Boyd & Nigg 2007).

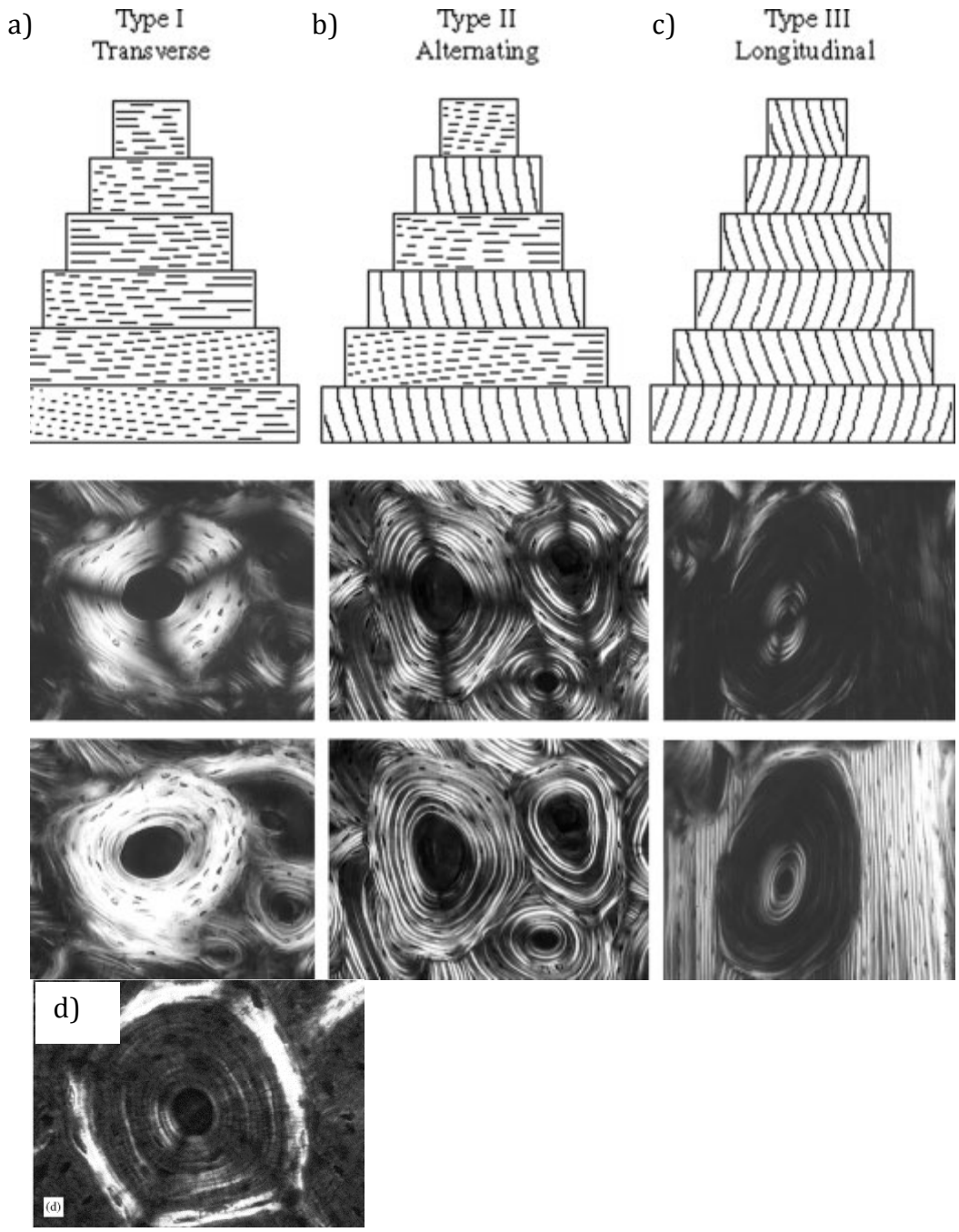

Figure 2.7 Polarized optical microscopy images showing the different types of osteons a) transverse b) alternating c) longitudinal and d) hooped (Martin et al. 1996; Bromage et al. 2003; Bigley et al. 2006) used with permission from the publisher.

2.2.2.4. Architectural

The architectural level refers to the tissue level and is divided into two distinct structures, cortical bone or cancellous bone.

Cortical bone is densely packed bone with no empty spaces except for blood channels and cells. Cortical bone can be found mainly in the diaphysis, which is the long portion of the bone (away from the joints) as well as all around the whole bone (Currey 2002).

Cancellous bone is porous and is composed of densely packed bone struts that form a larger bony structure. Cancellous bone is found where the bone needs to maintain a strength/density ratio such as at the ends of long bones and vertebrae. The bone in these areas needs to be strong enough to support loading stresses while maintaining material and metabolic efficiency. This ratio is maximised by a network arrangement made of trabecular struts. The struts are oriented according to the needs of the bone for specific requirements and loading conditions. The trabecular struts, or trabeculae, are usually around 0.1 mm in diameter and 1mm in length and connect to other struts typically at right angles as well as parallel oriented plates of bone. This type of cancellous bone is found under loaded surfaces with a constant stress pattern. A second type of cancellous bone is made of cylindrical struts with no particular orientation and is usually found deep inside bones away from loaded surfaces (Wainwright et al. 1982; An & Draughn 2000; Currey 2002).

Interestingly, when the trabeculae in cancellous bone are thick, around 300 μm, trabeculae can contain blood vessels and an osteonal arrangement. In appearance, these osteons found in thicker trabeculae are similar to primary lamellar bone or secondary osteonal, yet mechanically, bone found in trabeculae is different from bone found in cortical (Wainwright et al. 1982; An & Draughn 2000; Currey 2002). The osteonal arrangement found in these thicker trabeculae have been more recently characterized as primary osteons, which are a set of lamellae arranged in concentric rings around vascular channels as opposed to the entire bone cortex. The greatest difference between primary osteons and secondary osteons is the lack of cement lines found in primary osteons. (An & Draughn 2000; Boyd & Nigg 2007).

2.2.2.5. Macrostructure

All of the previously discussed components, structures and geometrical features contribute to resultant whole bone. In terms of the macrostructural level, bone has both mechanical and physiological functions. Mechanically, bone acts as a support for the body, assisting locomotion, and providing protection for internal organs. Physiologically, bone contributes to the body's mineral homeostasis, and in the formation of blood cells (haematopoiesis). Bone as a calcium storage is critical; the maintenance of calcium homeostasis takes priority over its own structural requirements. Calcium is important as it regulates major processes inside the body such as normal behaviour of heart muscles, nerves and blood clotting. Hormones regulate bone calcium

homeostasis: para-thyroid hormones (PTH), calcitonin (CT), cholecalciferol (vitamin D), reproductive hormones and growth hormones (Boyd & Nigg 2007).

At the macrostructural level bone can be classified into different geometric types; long bones, short, flat, irregular and sesamoid bones depending on the structural function of the part of the body. Despite this variety in shapes, the morphology of bone at a material level is the same and has a consistent organization as it is laid down by the same cells yet guided by the different forces that go through the structure (An & Draughn 2000; Boyd & Nigg 2007).

2.2.2.6. Water

Water is worthy of discussion as a separate structural feature of bone that is present across all of the structural length scales. Indeed, the solid components are almost certainly dependant on water for their structural and other properties. However, direct evaluation of the location and effect of water on bone behaviour is still not well understood but has been broadly categorized as existing in three states. The first state is as free water, in the Haversian and Volkmann's canals, in canaliculi, lacunae and other pores. The second state is as water loosely bound to collagen via hydrogen bonds. The third state is as water in the hydration shells of apatite mineral (Yan et al. 2008). Without the water molecules forming a highly ordered network the triple helix of tropocollagen would lose stability. The stability arises from the

formation of additional water-mediated hydrogen bonds in the remaining backbone peptide groups. The additional hydrogen bonds would not exist without water due to spatial constraints (Bella, Brodsky & Berman 1995; Beck & Brodsky 1998; Yan et al. 2008).

The mechanical properties of bone have been shown to decrease (Nyman et al. 2006) when water is lost from the bone material. Specifically, toughness and strength are sensitive to the amount of water present in bone, while there is contradicting evidence on how water content defines the bone's elastic modulus (Sedlin & Hirsch 1966; Hoffler et al. 2005; Chen, Stokes & McKittrick 2009; Currey et al. 2009; Morais et al. 2010; Wolfram, Wilke & P.K. Zysset 2010). The effect of water on the mechanical properties of bone will be discussed in Chapter 4.

2.2.3. Bone formation

Bone is formed by cells depositing an initial collagenous matrix in which mineral is later deposited. The initial collagenous matrix is later remodelled in order to obtain a more organized structure depending on the requirements, being chemical-biological or structural-mechanical.

2.2.3.1. Organic phase deposition and cellular function

Several types of cells are responsible for bone formation and different specific tasks in bone remodelling. The most significant cells are osteoblasts, osteocytes, osteoclasts and bone-lining cells. Osteoblasts are responsible for

bone formation and induce mineralization by laying down the initial collagenous matrix in which mineral is later deposited. Osteoblasts that become trapped in bone tissue during the formation of bone are known as osteocytes and can provide communication with neighbouring osteocytes and bone-lining cells through canaliculi and gap junctions. Osteoclasts are large bone resorbing cells that dissolve bone by latching on to the bone surface, leaving vesicles containing both organic and mineral debris behind. Bone resorption is important in both physiological and mechanical aspects. In the physiological aspect, bone is the largest ion reserve for the body; resorption allows the ions to be utilized when needed. In mechanical aspects resorption allows bone to be removed and produced according to the mechanical requirements of the body. Finally, bone-lining cells derive from osteo-progenitor cells and can be considered as dormant osteoblasts that cover the surface of bone and control the movement of ions between the body and the bone (Currey 2002).

Fratzl et al. (2004) describes bone formation as a process requiring coupling between remodelling, through the continuous resorption of old bone matrix, and replacement by new bone via the activities of bone cells. The osteoclasts form what is described by Currey as a 'cutting cone', which advances through bone material leaving a cavity of around 200 μm wide. As the cavity is forming, the walls are smoothed and osteoblasts occupy the cavity space while depositing bone material in a concentric lamellae shape but maintaining a central cavity for blood vessels and nerves (Currey 2002). The second part of the bone formation process is the mineralization of the newly

formed bone matrix following a characteristic time course. Typically, the collagenous matrix starts to mineralize rapidly after 13 days and reaches 70% of full mineralization capacity a few days later. The remaining 30% of the mineralization process occurs over several years and is called secondary mineralization (Fratzl et al. 2004).

2.2.3.2. Mineralization of bone

The mineralization of bone follows a typical crystallization process, favoured due to (thermodynamic) energy efficiency, within the collagen matrix. Nucleation of crystals occurs in both gap and overlap zones in energetically favourable sites of the collagen molecule. Formation of apatite crystals occurs at the gap and overlap zones of the ordered tropocollagen arrays in an asymmetric pattern corresponding to the polarity of the collagen molecule. The gap zone is less hydrophobic than the overlap zone and therefore corresponds to the localization of mineral (Maitland & Arsenault 1989). After the initial nucleation, mineral is further deposited all around and within the collagen fibrils. The gap zones of the fibril appear to expand to accommodate the growing hydroxyapatite crystals until they cannot be accommodated within the gap zones and therefore start to form in the spaces between tropocollagen molecules.

The growth of mineral crystals in bone can be further examined by consideration of the effect of NCPs. Non-collagenous proteins (NCPs) play an important role in mineralization and formation of collagen fibrils. These

proteins have been known to have an impact on the quality, speed and organization, necessary for normal bone remodelling (Ingram et al. 1996; Nanci 1999; Arteaga-Solis et al. 2011). As stated by Roach (1994), not all bone has the same composition and amounts of NCPs, possibly due to the required structures depending on the function of the particular type of bone (Roach 1994). NCPs contain many different proteins including the more significant components of osteocalcin, osteonectin, osteopontin, bone sialoprotein, fibrillin-1 and fibrillin-2. Osteopontin and bone sialoprotein are known to function as nucleators in the mineralization process as the collagen on its own would be too slow. Other proteins such as osteocalcin, osteonectin and osteopontin prevent further mineralization growth, thus controlling the size and the speed of mineral growth (Roach 1994). The function of bone sialoprotein (BSP) is not fully known but has been found in the initial phase of mineralization and is thought to aid cell attachment to mineralized matrices (Ganss, Kim & Sodek 1999). Fibrillin-1 and -2 gives rise to the assembly of the microfibrils and therefore has an effect on the morphology, mechanical properties and the material quality of long bones (Arteaga-Solis et al. 2011). None of these protein functions have been strongly identified.

2.3. Structure and function – Mechanical properties of bone as a composite material

Bone as a complex biological composite material performs a variety of mechanical functions, most notably load bearing and resistance to

catastrophic fracture. Bone achieves this mechanical function both through the use of a variety of component phases and organization of these phases across a range of different length scales.

Bone has been mechanically tested at different length scales using a range of different testing methods from large tensile testing of whole bone to nanoindentation of an individual lamella. Each of the levels introduces different mechanical properties directly affected by their structure. At the architectural level for example, the density, porosity, and the orientation of collagen fibres, osteons and trabeculae determine the mechanical properties of bone. At the microstructural level, the loading direction affects the properties i.e. maximum strength along the long axis. At the sub-microstructure level, the mechanical properties are also affected by the orientation of the lamellar sheets and large collagen fibres. The orientation is expected to define the maximum and minimum strength for a primary loading direction. At ultrastructural length scales, the composite formed by the rigid hydroxyapatite and the flexible collagen provides bone with superior mechanical properties (Les et al. 1994; Rho, Tsui & Pharr 1997; An & Draughn 2000). As with other biological materials, bone is not perfectly elastic, with mechanical testing of bone showing a slight degree of non-linear load-deformation and stress-strain behaviour. This non-linear behaviour is mainly influenced by the loading rate and temperature and is commonly referred to as viscoelastic behaviour resulting from internal energy losses due to friction in the structure (intrinsic viscoelasticity), or fluid flow (fluid-dependent viscoelasticity). Although there is this slight viscoelastic

behaviour, bone is usually treated as linear elastic or Hookean material (An & Draughn 2000).

Perhaps the most significant mechanical consideration of bone is its anisotropy. Bone stiffness is found to be at a maxima the longitudinal direction (along the long axis of the bone defined as the 0° angle) but lowest the lateral direction (perpendicular to the longitudinal direction defined as the 90° angle) (Liu, Weiner & Wagner 1999; Currey 2002; Boyd & Nigg 2007).

At the architectural level cortical bone is mechanically heterogeneous and has specific mechanical properties depending on the location of the bone. The mechanical properties of cortical bone are more homogenous along the length than around the circumference, due to the loading conditions of bone in vivo, the variations around the cross-section are small. For example, the middle third of the femoral shaft has the highest ultimate strength and elastic modulus, the lower third has the lowest ultimate strength and elastic modulus, the lateral quadrants have the highest ultimate tensile strength and the anterior quadrants the lowest ultimate tensile strength (An & Draughn 2000; Boyd & Nigg 2007). These distinct mechanical properties in different bone locations are due to the adaptation of bone to the types of forces that go through the specific quadrant.

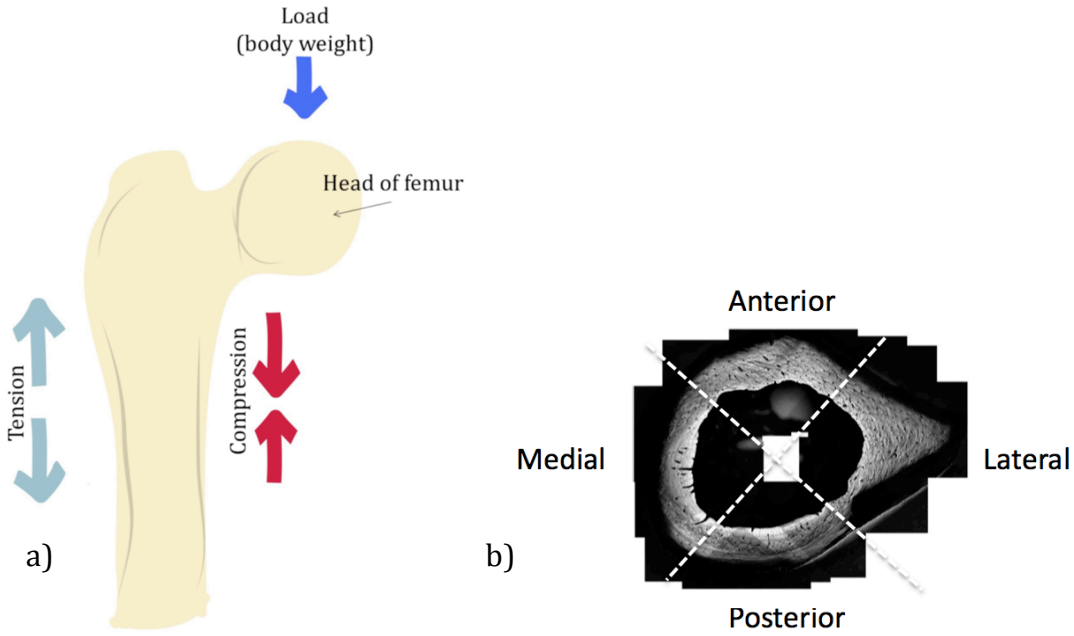

Figure 2.8 a) Schematic diagram indicating the forces acting on a bone femur and b) SEM micrograph of a femur cross section showing the anterior, posterior, medial and lateral quadrants. As shown in a) forces acting on the bone produce a range of loading conditions, thus each quadrant has distinct compositions and mechanical properties to resist these applied forces.

Figure 2.8 a) shows the forces acting on the femoral shaft in physiological conditions and highlights how the front of the femoral shaft is in tension, the lateral quadrants are in tension but the anterior quadrants are in compression (Rubin & Lanyon 1984; Riggs et al. 1993; Rho et al. 2001) and Figure 2.8 b) shows a cross-sectional area of a rat femur with the different quadrants depending on the anatomical location.

In terms of the mechanical properties at the microstructural level, osteons use a range of structures incorporating both collagen fibril orientation and mineral content to best resist the forces that predominate in specific segments of the skeleton. As assessed by polarized light microscopy osteons

with alternate 'bright' and 'dark' rings are the most resistant to bending stress and weaker in tension whereas longitudinal osteons, with collagen orientation mainly parallel to the long axis of the bone are stronger in tension. Transverse osteons, with collagen orientation mainly perpendicular to the long axis of the bone are stronger than the alternate and longitudinal osteons in compression (An & Draughn 2000; Ascenzi et al. 2003; Bigley et al. 2006). Later Martin et al. identified what he called a fourth type of osteons, hooped osteons (type O) (Martin et al. 1996). Type O osteons are characterised by having the outermost lamellar layer orientated transversally while the inner lamellae oriented longitudinally. Martin et al. describes that these hoop osteons are less likely to pull out as the other type of osteons indicating that they are more tightly bound to the surrounding bone and therefore would increase the overall elastic modulus as well as act as a barrier for micro-cracks (Martin et al. 1996).

Overall, taking into account the polarized microscopy, the dark, thin, collagen rich, isotropic osteons would best to resist tensile forces while the bright, thick, collagen poor, highly calcified, anisotropic osteons would be best to resist compression forces. In order to explain the osteon mechanics further, consideration of the collagen fibril orientation within the osteon needs to be considered as shown in Figure 2.7. The Type I transverse osteons show the collagen orientation perpendicular to the long axis of the long bone, while Type II and Type III osteons show collagen to be orientated mainly parallel to the long axis of bone. The collagen orientation along with the mineral content affects the mechanical properties. In Type III osteons, the collagen is aligned

along the long axis and allows bone to resist stresses in tension acting along the long axis of the collagen fibrils, indicated as lines in Figure 2.7. Applied forces acting on the osteon cause plastic deformation of the less mineralized collagen fibres, allowing energy to be absorbed and reducing crack propagation. In Type I osteons, the collagen aligned perpendicular to the long axis would not resist forces in tension, as the collagen fibrils would be more likely to break apart from each other. The perpendicular orientation of the fibres and the higher mineral content allows bone to deal with stresses in compression. The specific distribution of the different osteon types within the skeleton reflect the forces which predominate in the segment according to the specific needs, being either resisting stresses in compression or tension (Martin et al. 1996).

In terms of the mechanical properties at the sub-microstructural level, bone has been studied using nanoindentation techniques (Rho, Tsui & Pharr 1997; Guo & Goldstein 2000; Silva et al. 2004; Fratzl-Zelman et al. 2009; Maïmoun et al. 2012) to evaluate the influence of quality and quantity of the components, the organization and orientation and their interaction. As has been discussed earlier in Chapter 1 and will be discussed all throughout this thesis, nanoindentation results vary considerably and the interpretation of small scale bone behaviour is contentious.

A solid mechanics approach can define bone components predominantly as a soft collagen organic matrix incorporating a stiffer mineral phase. The mechanical properties can therefore be directly related to the amount of

mineral phase within the bone (Currey 1999). For example, deer antler (MVf =300; E=8.1GPa) is a form of bone with a relatively low volume fraction of mineral resulting in a low elastic modulus whereas larger mineral volume fractions (MVf) in Horse Femur (MVf =395; E=24.5GPa)(Currey 2002) provide larger elastic modulus values. Currey (Currey 2002), has tested a range of different types of bones using the same setup and dimensions allowing him to compare the mineral volume factor (MVf), elastic modulus, ultimate stress, ultimate strain and work to fracture. This work highlighted how increasing MVf produced an increase in the elastic modulus, shown across a large series of samples, but a decrease in ultimate stress and strain and therefore the work to failure.

The organic collagen and the mineral component, as well as their geometrical arrangement, is increasingly apparent as major contributing factors in bone mechanics (Fratzl et al. 2004). However, experimental evidence has also shown that NCPs have an effect on the mechanical properties of bone (Ingram et al. 1993; Fantner et al. 2005; Arteaga-Solis et al. 2011) both by regulating morphology which affects bone's mechanical properties (Arteaga-Solis et al. 2011) and by acting as a glue between collagen fibrils (Fantner et al. 2005). The NCPs are mainly thought to serve metabolic functions (Currey 2002) but can be crucial for defining bone mechanical properties as Ingram et al. (1966) observed while studying Paget's disease in which bone shows an abnormal architecture. Ingram found that NCPs played an important role in the organization, speed of formation and density of collagen fibrils and mineralization of the bone matrix by promoting cell-matrix interactions

necessary for normal remodelling (Ingram et al. 1996; Nanci 1999). Different types of bone further distorts the study of the effects of NCPs on bone mechanics, such as in cortical and trabecular bone, having varying composition and amounts of NCPs. This variation of NCPs in bone is thought to be due to the structures required by the organism depending on the function of the particular type of bone (Roach 1994). Fibril separation experiments were performed on bovine trabecular bone and it was found that this extra-fibrillar matrix seems to show properties similar to a glue layer between the fibrils which seem to be able to deform and break therefore acting as "sacrificial bonds" (Fantner et al. 2005; Fratzl & Weinkamer 2007). The glue like behaviour of NCPs allows bone to dissipate energy through these sacrificial bonds and improve toughness and stiffness by resisting separation and slippage of the fibrils (Fantner et al. 2005).

In terms of the mechanical properties at the ultrastructural level, each one of the components of bone have been investigated by a series of experiments such as nanoindentation (Tai et al. 2007), AFM scrapping and indenting (Wenger et al. 2007; Wenger, Horton & Mesquida 2008) and tensile testing of individual mineralized collagen fibrils (Hang & Barber 2011).

2.4. Conclusion

This chapter gives an introduction to the structure and function of bone at the different hierarchical levels as well the different components of bone. Bone has a complex structure and has a direct relationship to its function and

mechanics. Traditional composite mechanics can be used in order to study bone as a composite material. The lamellar unit, the unit block of bone, can give an insight to the overall mechanical properties of bone. The thesis attempts to isolate these lamellae in order to mechanically test and apply composite theory. Thus, by studying the mechanics of bone at the smallest length scale, which incorporates all of the components, the bone material behaviour can be evaluated.

Chapter 3. Materials and methods

3.1 Introduction

This chapter provides an overview of the materials and methods used throughout the thesis. As bone can be considered as a fibre-reinforced composite at micron length scales, a number of techniques are required to both prepare bone samples at micron length scales and mechanically characterized such length scales. This work therefore uses a combination of focused ion beam (FIB) for the sample preparation and scanning electron microscopy (SEM) and atomic force microscopy (AFM) for mechanical testing, with techniques described in detail here before application in subsequent chapters.

3.2 Imaging

The scanning electron microscope (SEM) was first developed in the 1940's and is a technique that uses electrons focussed onto a sample's surface to produce a two dimensional image (Ubic 2005). The setup of a typical SEM is shown in Figure 3.1. The electron microscope used in this work is a dual beam microscope (Quanta 3D FEG, FEI, USA/EU), which uses a field emission gun (FEG) as an electron source for higher resolution imaging, in this case down to <1 nm. The electrons from the FEG are accelerated on to the surface of the sample and three condenser lenses focus the electron beam to a diameter of the order of 1 nanometre.

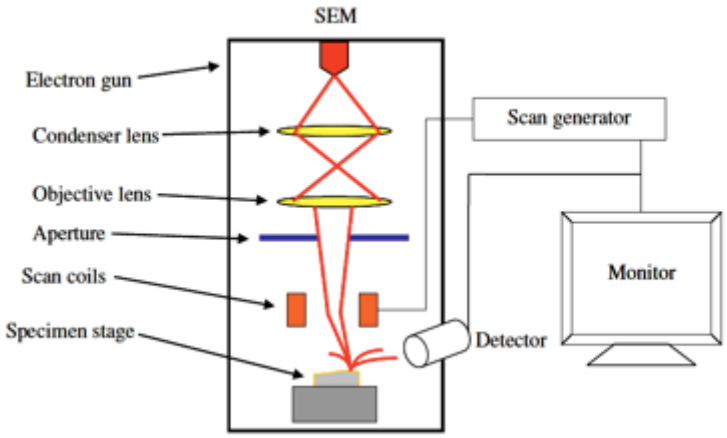

Figure 3.1 Schematic of a typical scanning electron microscope (SEM) (Ubic 2005).

Secondary electrons and backscattered electrons are scattered from the surface of the sample during raster-scanning of the primary electron beam and are counted by the detectors. The number of electrons detected at each position of the primary beam on the sample's surface produces a resultant 2D image. The most common electron detector is an Everhart-Thornley detector, which is a scintillator-photomultiplier sitting at the side of the specimen chamber inside the SEM. Everhart-Thornley detectors operate by attracting scattered low energy secondary electrons (SE) to the small positive voltage (+250 V) on the screen of the detector. SE pass the screen and are accelerated in order to impact the scintillator in order to cause light emission, which is then detected by a photo-multiplier (Ubic 2005). The initial acceleration voltages in this setup range from 0.2-30 kV with currents up to 200 nA.

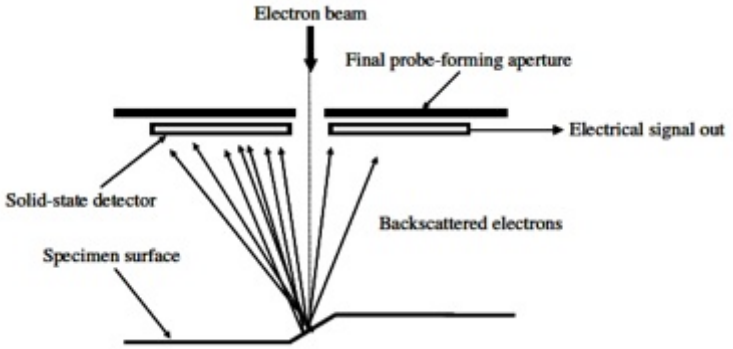

Figure 3.2 Schematic of a typical backscattered electron detector (BSED) (Ubic 2005).

The collection of scatter (backscattered) electrons using a detector is shown in Figure 3.2. Backscattered electron detector (BSED) imaging was also used in this study as it provides contrast between different materials. Image contrast using backscattered electrons is particularly useful and is given by the number of backscattered electrons produced, which is dependent on the atomic number of the elements in the specimen at the surface of the sample (Ubic 2005). Thus, high atomic number elements scatter a relatively large number of backscattered electrons, resulting in a bright image, whereas low atom number elements scatter a small number of backscattered electrons, resulting in a dark image.

The production and scattering of electrons typically requires a vacuum system so that electrons do not scatter off air molecules. The sample must therefore be mounted inside a vacuum chamber. The SEM system in this work, allows for the vacuum chamber to be adjusted to different states. The two main states used in this study are high vacuum HV and low vacuum LV

with pressures of <6 x 10^{-4} Pa and 10-130 Pa respectively. The details of actual chamber pressures used for the in situ testing in this study are given in Chapter 4.

Scanning electron microscopes have been widely used for the study of bone and the different hierarchical levels that it incorporates. Although there is controversy on the possible damage the electron beam and the vacuum chamber can have on the bone sample, it has been widely agreed that SEM is a suitable method for imaging bone (Boyde & Jones 1996). Chapter 4 strengthens the suitability of the SEM to study bone by determining the effect of the SEM vacuum chamber on bone at small length scales such as at the sub-microstructural level.

3.3 Sample preparation

The aim of the sample preparation was to produce bone samples with volumes suitable for probing micromechanical properties. The instrument of choice for this sample preparation was focused ion beam (FIB) microscopy. FIB is able to remove material using a beam of Gallium ions that are focussed to a point on the sample. While FIB has been used extensively in the preparation of thin samples for TEM (Giannuzzi & Stevie 1999) and was originally developed for patterning of semi-conductor materials (Brown, Venkatesan & Wagner 1981), the technique is particularly adept at removing material to define a discrete volume from a parent material.

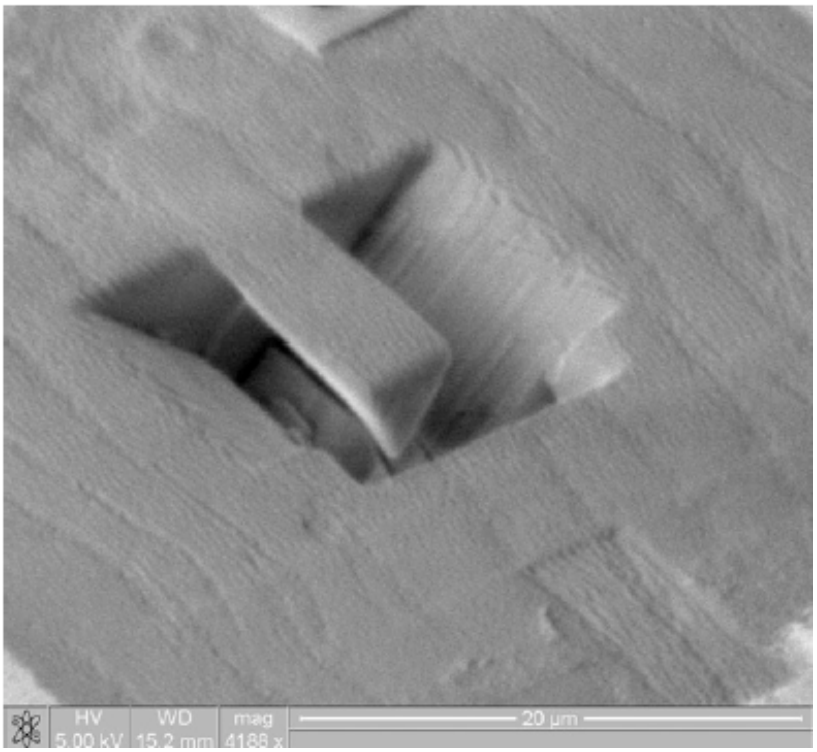

Figure 3.3 FIB preparation of cantilever micro-beam with a triangular cross-section in human primary molar sliced sections (Chan, Ngan & King 2009)

FIB applications in biological systems for mechanical testing are limited, with perhaps the only previous work fabricating triangular cross-section beams in tooth enamel for subsequent bending to failure experiments (Chan, Ngan & King 2009). The sample preparation in the work of Chan et al. is shown in Figure 3.3 above and indicates a beam with a length of approximately 10 μm and a width of 2 μm. FIB milled beam dimensions in Figure 3.3 are of interest as they approach, or even exceed, the dimensions required to study an individual bone lamellar unit. Thus, in principle, FIB can be used to isolate volumes suitable for understanding the composite mechanical behaviour of bone lamellar units.

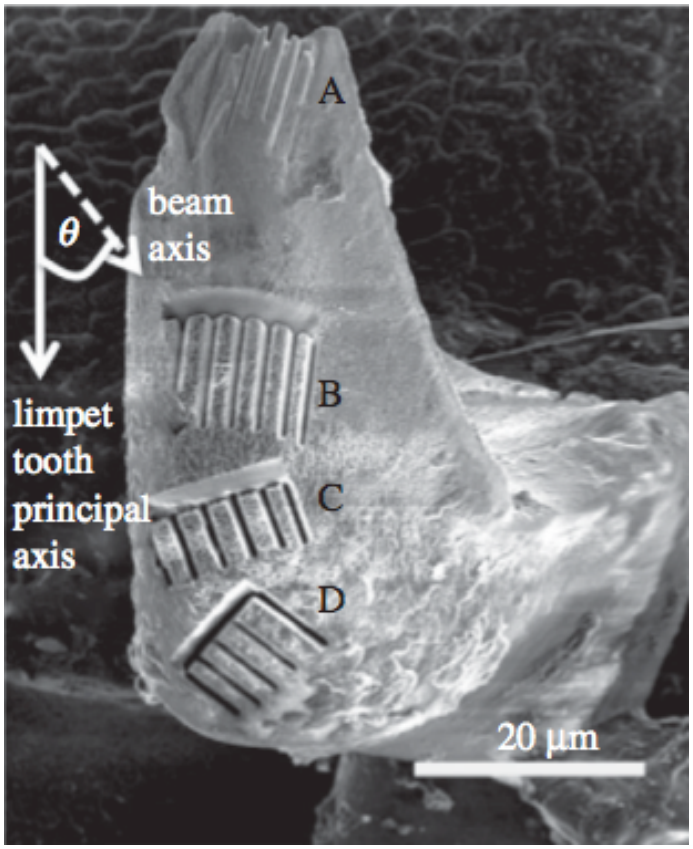

Figure 3.4 FIB milled micro-beams produced in the tooth of a limpet. The production of beams at different orientations were used to study anisotropic effects in limpet tooth mechanics (Lu & Barber 2012).

More recent work has prepared more standard regular rectangular cross-section beams for the study of limpet tooth mechanics as shown in Figure 3.4. Rectangular cross-section beams are deemed to be suitable for studying elastic properties of materials at small length scales, especially as conventional continuum mechanical descriptions exist to describe bending experiments on such beams.

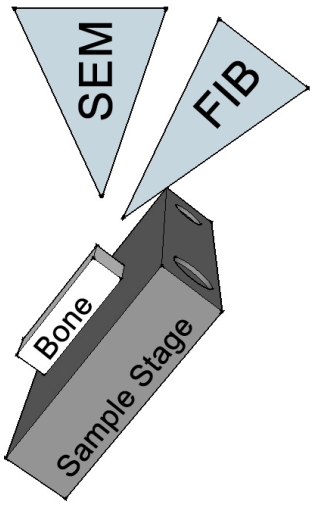

Figure 3.5 Schematic of dual beam chamber setup in Quanta 3D FEG (FEI, USA/EU). The SEM beam is above while the FIB is at a 52° angle.

Modern FIB setups are typically incorporated into scanning electron microscope (SEM) instruments known as a dual beam system. The SEM beam sits above the sample as shown in Figure 3.1 and the FIB sits at a 52° angle as shown in Figure 3.5. The sample has to be tilted at a 52° angle in order to align the FIB to the sample and proceed to mill parallel to the surface of the sample. Indeed, the orientation of the FIB is critical in order to limit the implantation of Gallium ions within the sample during preparation. An ion beam that is incident to a sample's surface will cause ion implantation, potentially changing the mechanical properties of the sample. Two factors are critical to protect the sample from defocused ions, the first one is to use a metal coating at the sample's surface and the second one is to orientate the FIB parallel to the sample surfaces produced, thus minimizing gallium ion implantation (Giannuzzi & Stevie 1999).

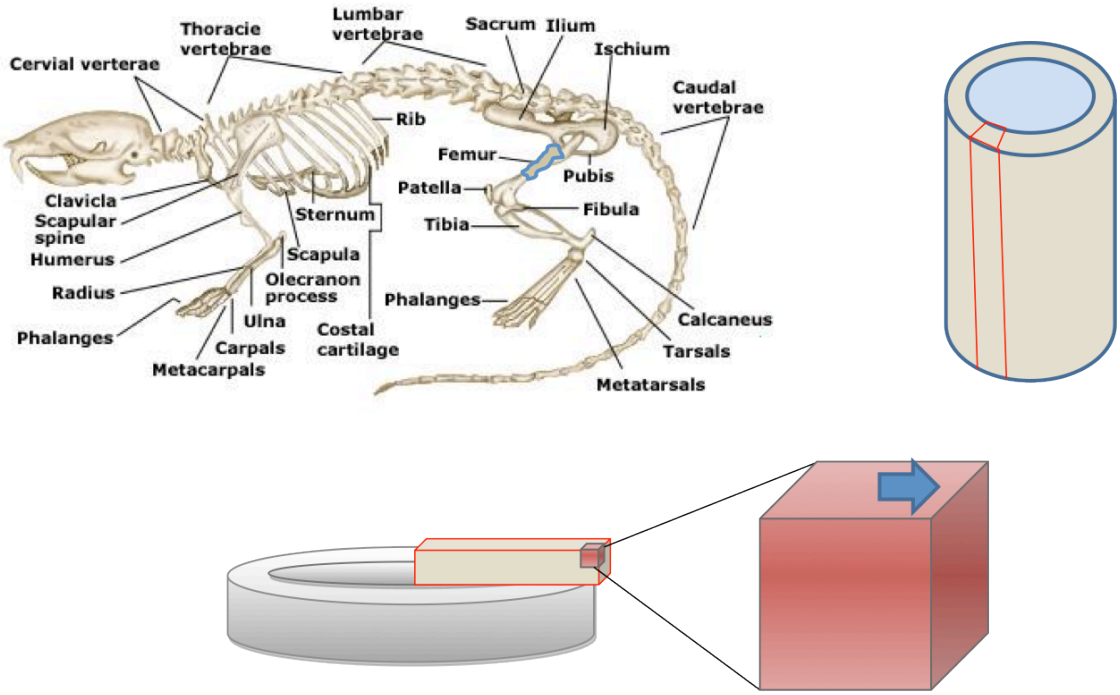

Figure 3.6 Diaphysis extracted from a rat femur sliced and mounted on to metal holder. Blue arrow indicates long axis of bone (TutorVista 2012) used as part of the fair use policy.

The strategy for sample preparation is therefore to exploit FIB methods in order to prepare beam geometries in bone for mechanical testing. We note that this appears to be the first attempts to produce such samples in bone materials.

Femora from 8-month-old sprague drawly rats were used in all of our investigations. The diaphysis from the extracted rat femur was first isolated using a water-cooled diamond blade slow speed circular saw (Buehler, U.S.A) as shown in Figure 3.6.

Table 3.1- Dehydration of bone using increasing concentrations of ethanol in water.

% Ethanol	Time/min
70%	Storage
90%	60
95%	30
100%	30
100%	30

Beams of cortical bone with dimensions of 12x1x1 mm were produced and stored in 70% ethanol. Bone samples were further dehydrated by submerging in a series of water/ethanol solutions summarized in Table 3.1 prior to FIB milling.

The dehydrated bone was gold coated for 30 seconds and fixed to the sample stage using a two part epoxy glue (Poxipol, Arg.) of a dual beam microscope (Quanta 3D FEG, FEI, USA/EU) incorporating both SEM and FIB. Dehydration of samples were then gold coated in the dual beam instrument to avoid charging effects that could interfere with the FIB milling process and to prevent drying cracks occurring in the sample from the vacuum pumping system. FIB milling was performed by a succession of processes summarized in Figure 3.7.

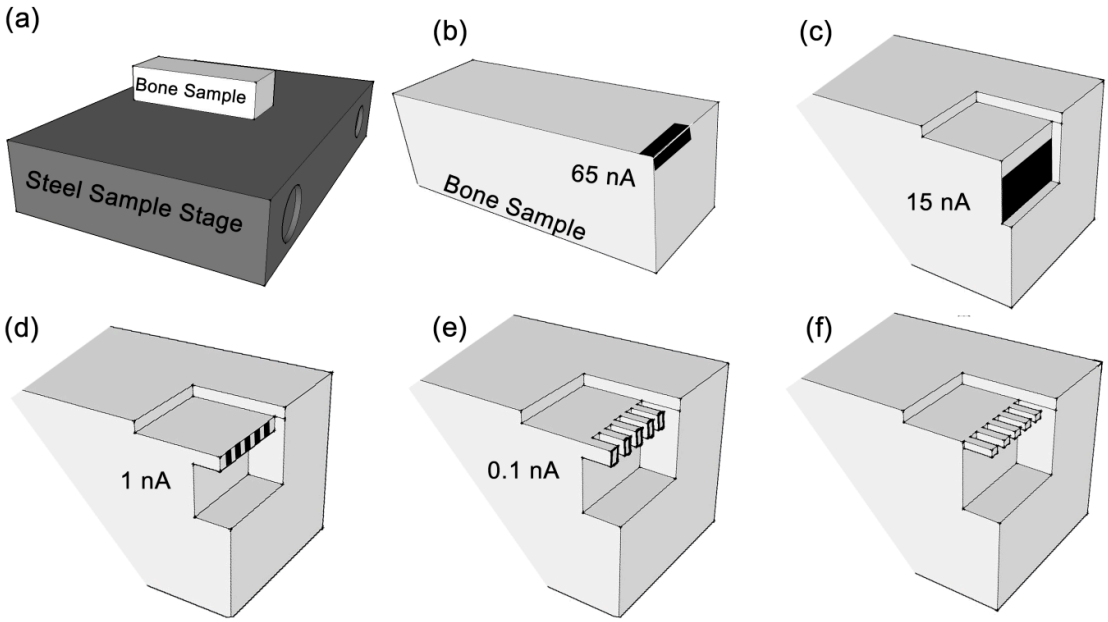

Figure 3.7 Schematic of the Focused Ion Beam (FIB) milling process. The black rectangles mark the FIB milled area. a) bone sample mounted on AFM steel sample stage, b) initial edge cleaning cut using a FIB current of 65 nA, c) separation of bulk from edge using a FIB current of 15 nA, d) isolation of beams using a FIB current of 1 nA, e) fine cutting and shaping of beams using a FIB current of 0.1 nA, f) finalised sample showing 8 beams across. All cuts performed with a FIB acceleration voltage of 30 kV.

Briefly, FIB was used to remove material in order to produce discrete beam volumes by first cleaning a bone sample edge using a high current ion beam of 65 nA and accelerating voltage of 30 kV as shown in Table 3.2. Flattening of the bone edges allows further removal of smaller bone volumes using smaller ion beam currents down to 0.1 nA. The smaller ion beam currents avoid observable ion beam damage. In addition, the FIB milling is always performed parallel to the produced sample faces to reduce embedding the impinging gallium ions from the FIB within the discrete beam volumes produced.

Table 3.2 – FIB conditions used to define the beam size for testing in Attocube system. The steps are chronological from top (high current) to bottom (low current).

Current /nA	**Dimension / μm x,y,z**	**Time / min**
65	100x20x2	20
65	100x20x2	20
15	100x10x1	10
1	5x10x1	10
0.1	Polish around the beam	5-10

A short column between each of the beams was left in order to prevent the re-deposition of milled material and gallium ions on to neighbouring beams. These particles redeposit on to the short columns instead of the sample beams. The resultant FIB process allowed the fabrication of cantilever micro-beams with dimensions 2x2x10 μm as shown in Figure 3.8, with the long axis of the cantilever beam parallel to the long axis of the bone.

Samples were rehydrated before mechanical testing by removal from the dual beam chamber and placing for two hours in a closed vessel containing a high vapour concentration of Hank's buffer solution. We note that bone samples have been observed to require only 45 minutes for rehydration (Utku et al. 2008), indicating that our hydration time is sufficient. Such a hydration process was considered superior to submerging the sample in water where the surface tension of the water may deform the relatively fragile cantilever micro-beams sufficiently to cause fracture.

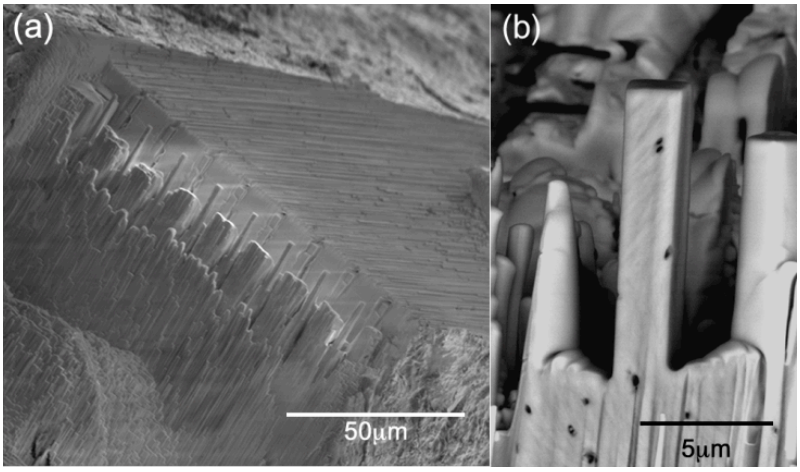

Figure 3.8 a) SEM SE image of a series of beams fabricated from the parent rat bone sample and b) BSED image higher magnification image showing an individual rat bone cantilever micro-beam.

3.4 Mechanical testing

Mechanical testing of the FIB fabricated bone cantilever beams was carried out using Atomic Force Microscopy (AFM). AFM allows characterization and manipulation of samples at the micro/nano scale and is a particularly important technique for deforming samples at low loadings. As the bone samples prepared using FIB have relatively small volumes, AFM has sufficient force resolution for the measurement of FIB prepared bone beams. AFM involves the use of a cantilever with a sharp tip at the end attached to a set of piezo-electric ceramics, usually used to scan the topography of a surface. This tip is placed near the surface of a sample where it interacts. Historically, AFM has been used to produce 3D topographic reconstructions of sample surfaces by exploiting the interaction between the AFM tip and sample surface (Binning et al. 1982; Aibrecht & Quate 1987) The interactions can vary depending on the application and need; these include Van der Waals

forces, capillary forces, chemical bonding, electrostatic forces, magnetic forces, Casimir forces and solvation forces (Butt, Cappella & Kappl 2005). Further work has also shown the possibility of measuring additional quantities simultaneously through the use of specialized AFM tips (Butt, Cappella & Kappl 2005).

An interaction between an AFM tip moved into contact with a solid surfaces in the most typical of cases can be described by a Lennard-Jones potential, which is a mathematical model describing the interaction of two neutral atoms, molecules or surfaces as they approach each other (Lennard-Jones 1925). The Lennard-Jones potential can be best described by a graph of the interaction versus the distance as shown in Figure 3.9. The curve describes the interaction between two objects across a range of distances. Two objects with a relatively large separation distance interact weakly but in attraction, indicated by a small negative interaction energy in Figure 3.9, which increases to an energy minima. Decreasing the separation distance beyond the energy minima causes a less favourable interaction energy, defined as a negative gradient, and therefore repulsion.

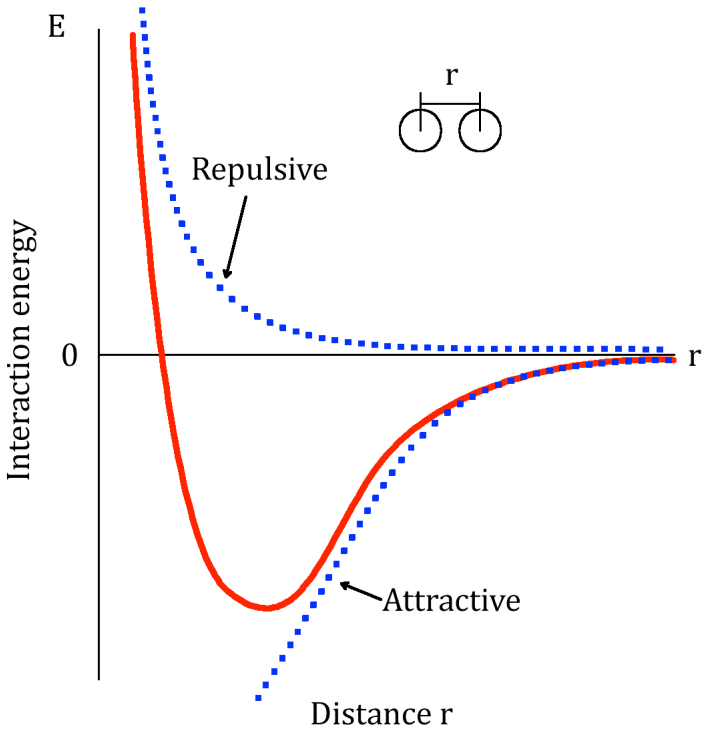

Figure 3.9 Lennard-Jones curve showing the interaction energy between two surfaces with separation r between the surfaces.

AFM microscopy for topography imaging uses this Lennard-Jones behaviour when an AFM tip is systematically scanned over a surface with piezoelectric positioners while monitoring the extent of the interaction. Changes in sample topography will cause a change in the interaction between the scanning tip and sample. These changes can be related to surface topography so that, for example, a high feature on a solid surface will increase the interaction between the AFM tip and sample whereas a hole in the sample will decrease the surface-AFM tip interaction as the sample is effectively far away from the AFM tip. An imaging AFM tip is able to measure tip-sample surface interactions by the cantilever system attached to the AFM tip such that repulsion and attraction causes a corresponding bending in the cantilever.

An optical system is additionally used to convert the AFM cantilever bending into a measurable electrical signal. AFM imaging exploits a feedback system so that, during scanning of the AFM tip across the sample's surface in an x-y plane, the AFM tip-sample interaction is monitored and the AFM tip moved towards or away from the sample surface using a z-piezo positioner in order to maintain the AFM tip-sample interaction. Thus, recording the piezo (x, y, z) co-ordinates during AFM tip scanning over the sample surface produces a topographic image of the sample. This same mechanism can be used to accurately measure forces when the AFM tip moves towards a sample into contact or away from a sample to perform a mechanical test as opposed to imaging. Forces acting between the AFM tip and a sample will cause a corresponding deflection of the AFM cantilever during the approach or removal of the AFM tip from the sample. According to Hook's Law, the bending of an AFM cantilever can be converted to force by consideration of the spring constant k of the cantilever, which is in turn defined by both the elastic modulus of the cantilever material (silicon) and the cantilever dimensions. An AFM standard technique calculates the spring constant of the AFM cantilever by the Sader calibration method included in the NT-MDT AFM software package, Nova (NT-MDT, Rus.), and uses the area of the cantilever, the resonance frequency, the quality factor of the AFM cantilever and the density and viscosity of the fluid in which these are measured, in this case air (Sader et al. 1995; Ohler 2007). These factors are then considered in the following equation:

$$k = 7.5246\rho_f w^2 L Q f_0^2 \Gamma_i(\mathrm{Re}) \qquad \text{Eqn. 20}$$

where:

$$\mathrm{Re} = \frac{2\pi\rho_f f_0 w^2}{4\eta_f} \qquad \text{Eqn. 21}$$

Where k is the spring constant, ρ_f is the density of the media around the AFM cantilever, w is the width of the cantilever, L is the length of the cantilever from the base to the apex, Q is the quality factor of the cantilever, f_0 is the resonance frequency of the cantilever, Γ is the imaginary component of the hydrodynamic function, which in turn is a function of the Reynolds number, Re, which is defined in Equation 21, where η_f is the viscosity of the fluid. Both the quality factor of the cantilever and the resonance frequency are determined by performing a power spectral analysis of the cantilever's thermally driven oscillations. The resonance peak is fit with the following harmonic model:

$$A = A_{white} + \frac{A_0 f_0^4}{\left(f^2 - f_0^2\right)^2 + \left(\frac{f \cdot f_0}{Q}\right)^2} \qquad \text{Eqn. 22}$$

Where A_{white} is the white noise fit baseline and A_0 is the zero frequency amplitude. The four parameters are fitted using a least-squares method (Ohler 2007). Overall, the Sader method is accurate for calibration of AFM rectangular cantilevers and has been determined to have only ~4% uncertainty, with the cantilever width as the major source of error (Ohler 2007).

Displacement of a sample during contact or separation from an AFM tip is further required in order to determine a sample's mechanical performance. A profile of the force acting on the AFM tip (with respect to the tip position relative to the sample) is required, known as a force-distance curve as shown in Figure 3.10. Two force-distance curves are required when evaluating the deformation behaviour of a sample when loading with an AFM tip. The first curve recorded is that of the AFM cantilever deflection as a contacting AFM tip is moved towards a rigid non-deformable surface, which is referred to as calibration curve, shown in red in Figure 3.10. This curve shows that z-piezo movement causes a corresponding deflection in the AFM cantilever. Thus, the cantilever deflection measured using the AFM optical setup can be directly converted to a length displacement. The second curve in Figure 3.10 corresponds to an AFM tip moving towards and into a deformable sample surface, therefore producing a mechanical test on the sample and is referred to as the test curve, shown in blue in Figure 3.10.

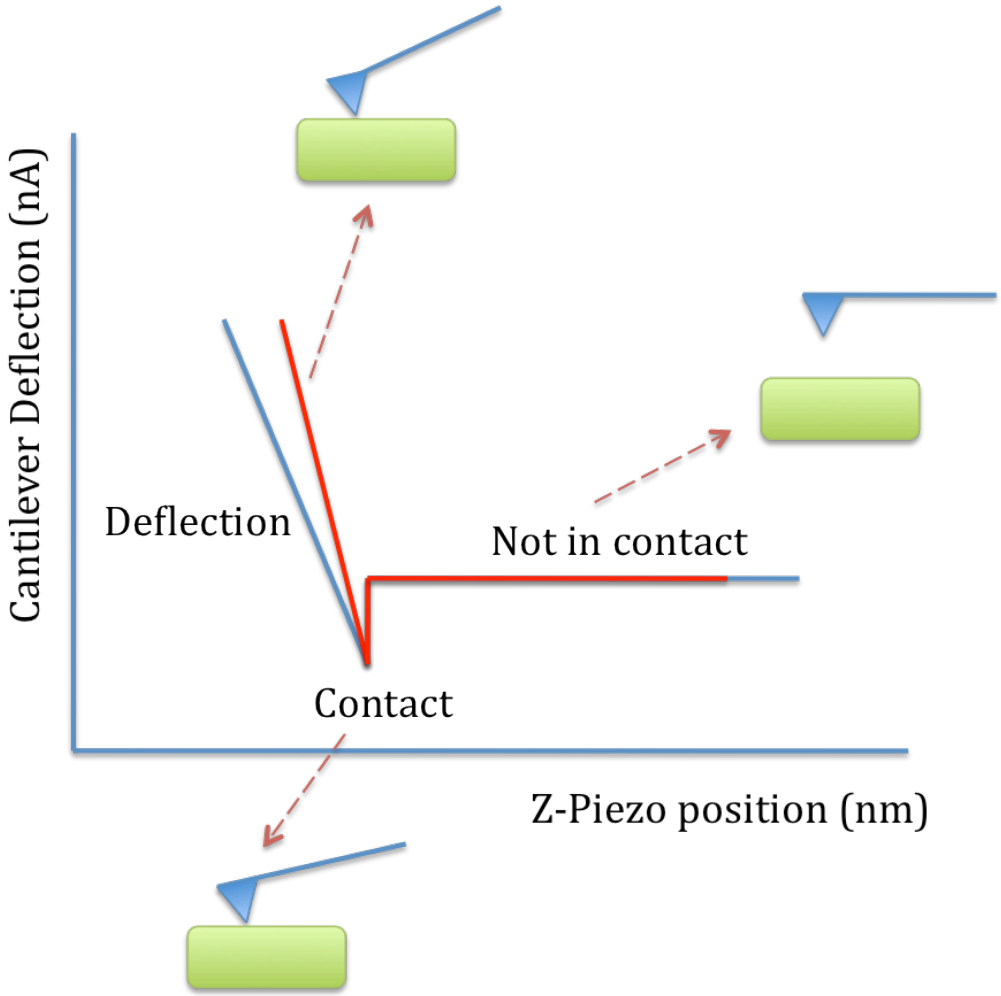

Figure 3.10 Schematic plot of AFM cantilever deflection against z-piezo position. The red line corresponding to the approach and contact of an AFM tip with a rigid non-deformable sample in order to carry out AFM cantilever deflection calibration. The blue line indicates approach and contact between an AFM tip and a deformable sample.

By assuming that the sample will behave differently to that of a rigid surface, the difference between the two curves gives the deformation of the sample that is being tested by:

Sample Deformation= Test curve – Calibration curve

The force can be then measured by the following relationship.

$$f = xk \qquad \text{Eqn. 23}$$

Where f is the force applied by the AFM tip, k is the AFM cantilever spring constant and x is the bending of the AFM cantilever under the applied force f in the calibration curve. The force applied by the AFM tip to the sample depends on the stiffness of the AFM cantilever being used and the displacement of the AFM cantilever.

Mechanical tests on the bone cantilever beams are performed on individual beams by applying a force using a custom built AFM setup. The custom built AFM (Attocube GmbH, Ger.) is installed inside the scanning electron microscope (SEM) chamber and can be later removed from the chamber in order to test the samples wet in air.

The AFM system is oriented to allow access of an electron beam from an SEM to image the AFM tip sample contact point as shown in Figure 3.11. Due to the limited space available in an SEM, the optical system required to measure AFM cantilever deflections is based on an optical interferometer that examines the interference of laser light emitted from a glass fibre optic positioned behind the AFM cantilever as shown in Figure 3.11 below.

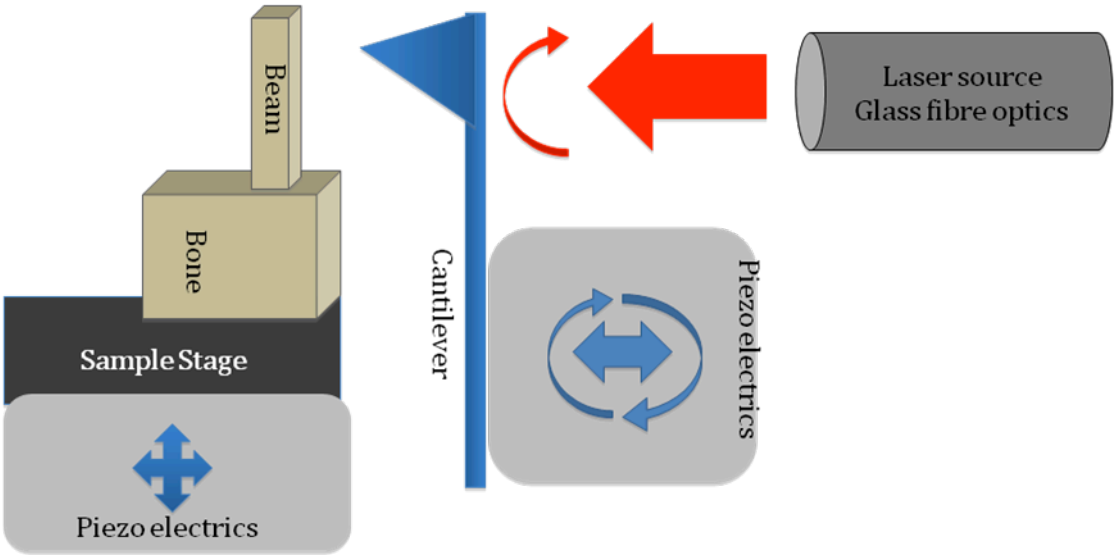

Figure 3.11 In situ AFM Attocube system setup within the SEM chamber.

The AFM system in Figure 3.11 is able to move a FIB fabrication bone micro-beam towards beam bending from contact with the AFM tip. The force applied by the AFM causes a corresponding deflection in the bone beam during the mechanical bending tests in all AFM systems. An interferometer system is preferred in Figure 3.11 due to its compact size required to fit within an SEM chamber. The change in distance between a deflecting AFM cantilever and optical fibre detector during mechanical testing produces a sinusoidal curve in terms of sample movement with change of the laser intensity reflected from the AFM cantilever in volts, as shown in Figure 3.12. The resultant sinusoidal curve is then translated into a force-distance curve with the help of a script specially written for this purpose and is described in detail in the Appendix.

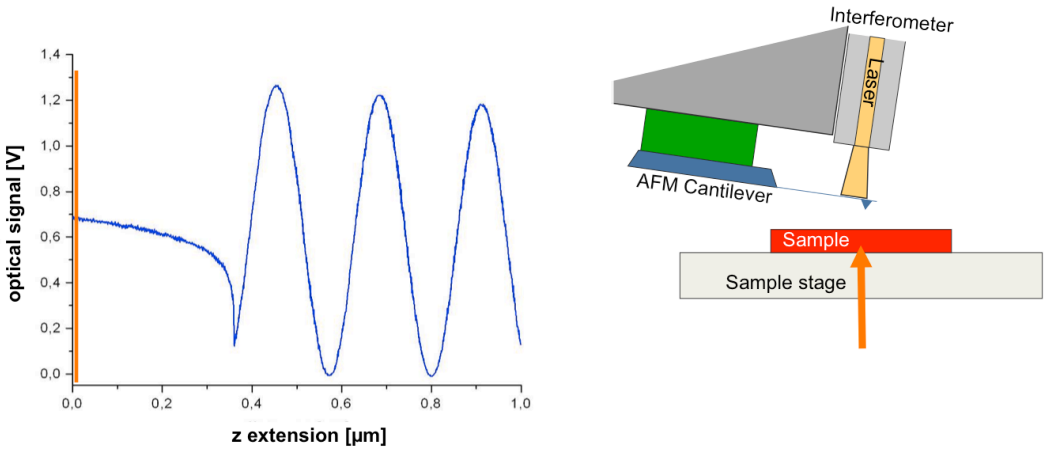

Figure 3.12 Schematic showing the resultant laser light reflected from the back of an AFM cantilever to the fibre optic detector during AFM mechanical testing. The optical signal varies sinusoidally as the reflected laser light interferes constructively or destructively with the incident light (left) as the sample fixed to the sample stage is moved towards the AFM cantilever system containing the interferometer (right).

3.5 Conclusions

This chapter details the methods used in order to isolate discrete cortical bone volumes of the order of 40 μm^3 using FIB. Further techniques based on AFM are described in order to apply forces to small scale objects and, ultimately, perform mechanical testing of bone at the sub-lamellar level. The techniques and transit protocols followed for the purpose of this work are shown in Figure 3.13 below. These methods will be continually referred to in the following chapters.

Sample preparation process

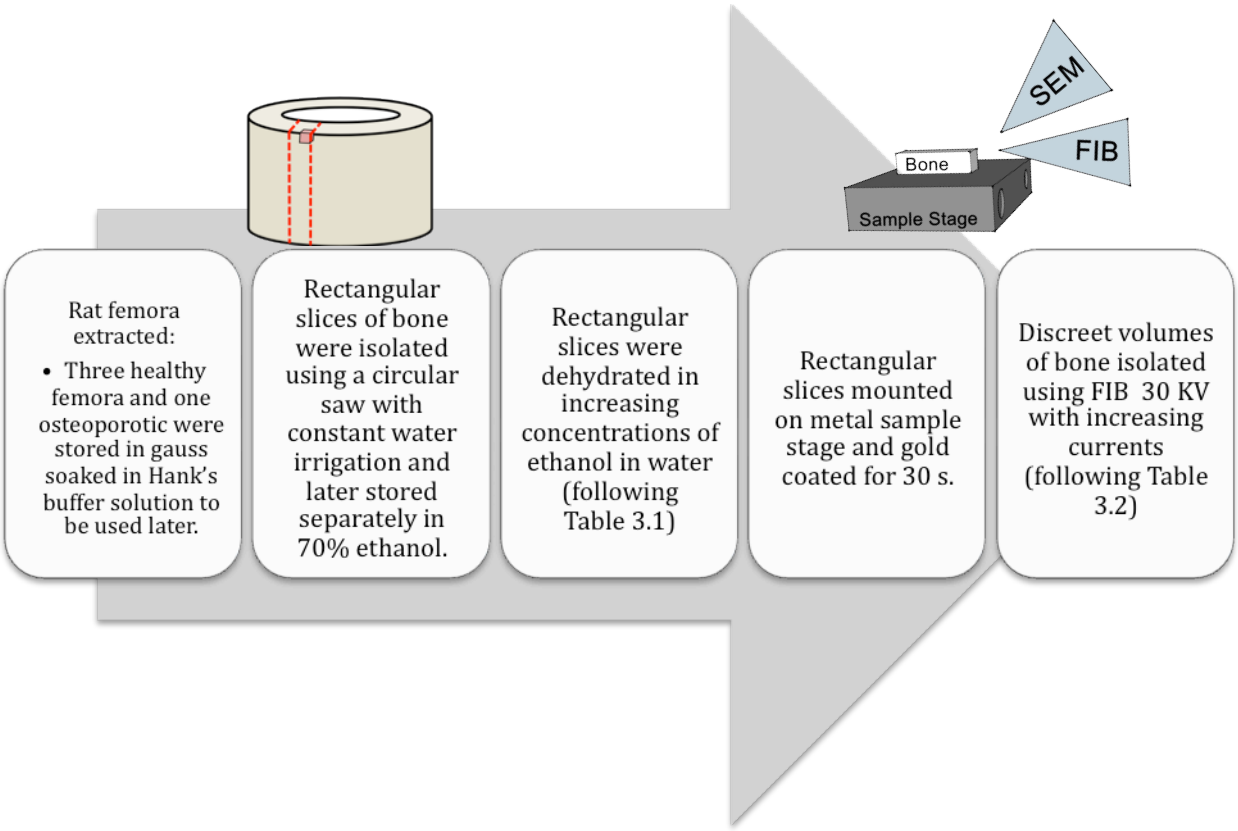

Healthy bone sample for bending tests to small deflections (Chapters 4 & 5) and bending to failure (Chapter 6)

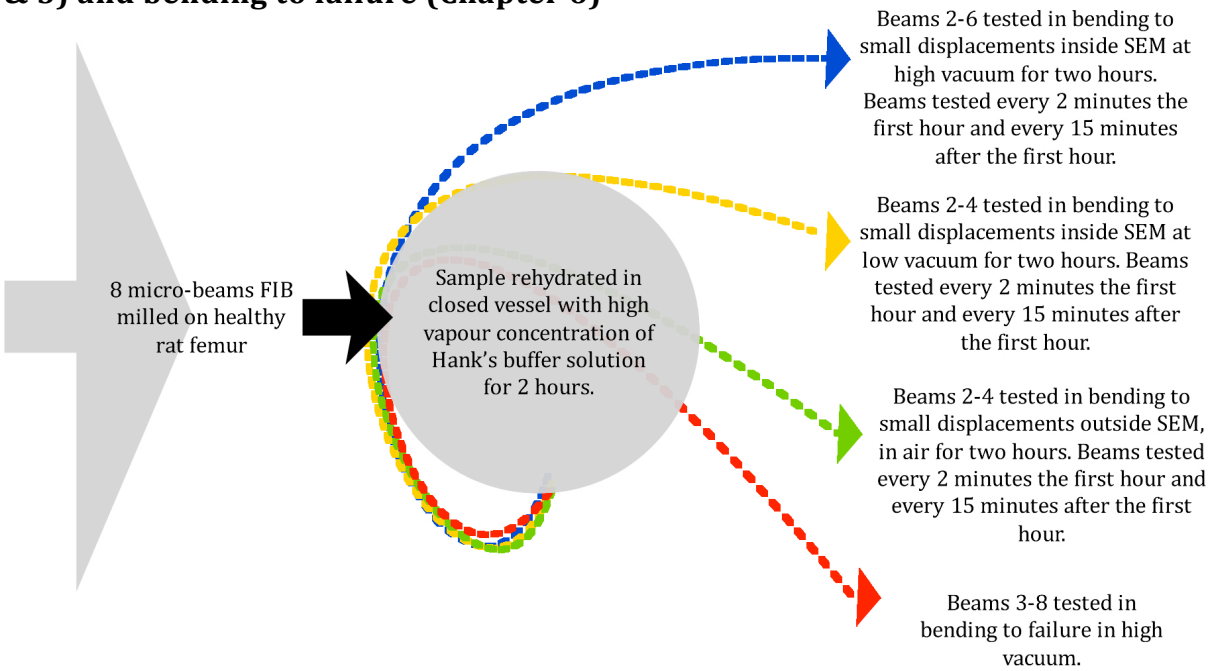

*Note: Beam 1 was not tested succesfully.

Healthy sample for buckling to failure tests (Chapter 6)

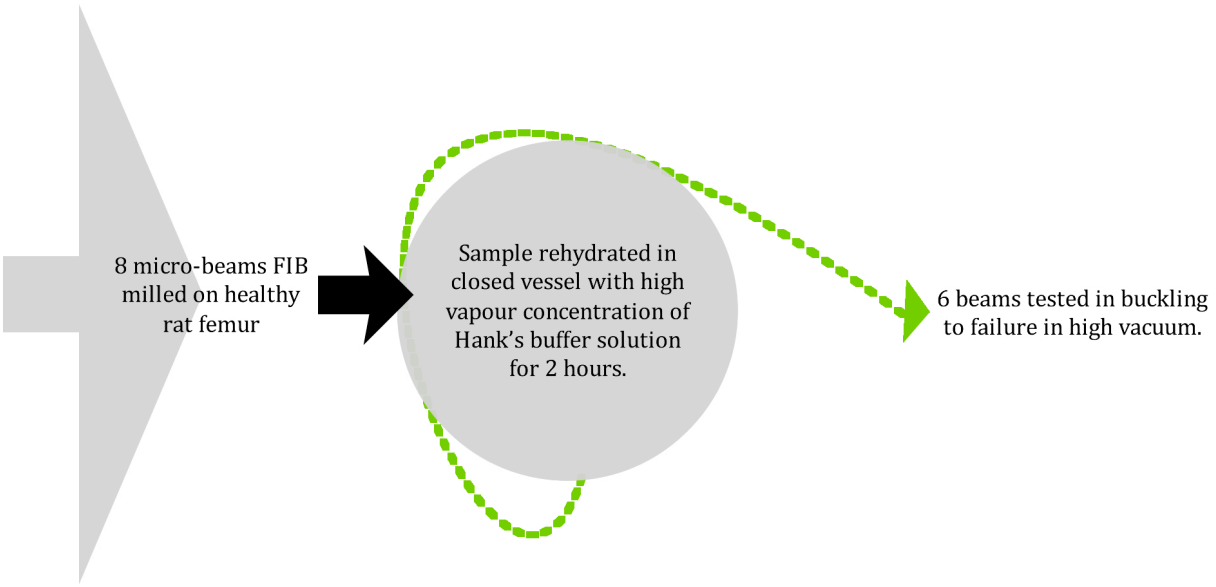

Healthy vs osteoporotic sample tested in compression to failure tests (Chapter 7)

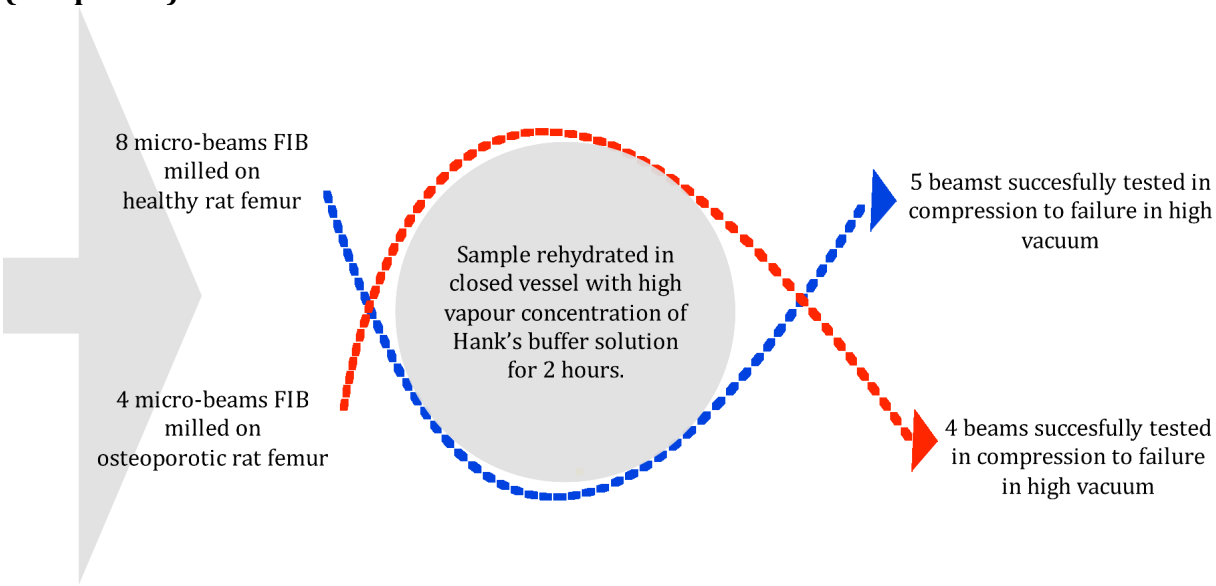

Figure 3.13 Flow chart of experimental methods used accross this work, starting from the sample prepartion and continuing with the transit and protocols followed for the specimens in each experiment.

Chapter 4. Effect of environment on elastic mechanical properties of bone

4.1 Introduction

The properties of bone are determined by the level of hydration (Currey 2002). Thus, evaluating structure-mechanical property relationships in bone using techniques that potentially employ vacuum conditions, such as FIB and SEM detailed in the previous chapter, may compromise measured mechanical behaviour. In order to determine the effect of the vacuum on the mechanical properties of bone at the sub-lamellar level, a series of mechanical tests on bone micro-beams at different vacuum conditions including wet in air were performed. The results of these tests are discussed in detail in the following sections.

4.1.1 Background

Bone is physiologically in a hydrated state, therefore a number of studies have attempted to define the effects of water on the mechanical properties of bone as summarized on Table 4.1. First investigations of bone mechanical behaviour by Sedlin and Hirsch revealed an increase in bone strength achieved with no change in elastic modulus for samples dried in air after one hour, with a significant increase in elastic modulus observed only after drying in an incubator at 105°C for a week (Sedlin & Hirsch 1966). Currey

later performed mechanical investigations to assess the effect of rehydrating bone after holding the sample in air for 25 days. Currey observed little change in bone mechanical properties between the initial hydrated state and the rehydrated state (Currey 1988). More recent work on deer antler has indicated an increase in the elastic modulus and strength, with a decrease in failure strain of dry antler bone relative to its hydrated state using bending mechanical testing (Currey et al. 2009). Morais et al. have indicated similar increases in elastic modulus but decrease in work of fracture for bovine cortical bone with dehydration (Morais et al. 2010). Further studies on elk antler bone also highlight the increase in strength and decrease in failure strain upon dehydration, although the elastic modulus of the bone showed little dependence on the hydration state (Chen, Stokes & McKittrick 2009).

Table 4.1 – Effects of hydration on the elastic modulus of bone taken from literature.

Literature source	Time	Temp /°C	Effect on elastic modulus	Testing method	Sample size /mm	Bone type
Nyman 2006	30 mins	21	8% decrease (stat. diff.)	3p-bending	30×4.2×2.1	Human
Nyman 2006	4 hrs	21	12.9% increase	"	"	Human
Nyman 2006	4hrs	50	10% increase	"	"	Human
Nyman 2006	4hrs	70	43% increase	"	"	Human
Nyman 2006	4hrs	110	23% increase	"	"	Human
Morais 2010	48 hrs	37	11% increase	Double cantilever beam (DCB)	20x3.5x2	Bovine
Currey 2009	72 hrs	70	58% increase	3p-bending and impact	45x4.5x2.5	Antler
Chen 2009	Unclear	Unclear	Statistical diff.	3p-bending and compression	30x3x2	Antler
Sedlin 1966	1 hour	Air	No difference	3p-bending	50 x 5 x 2	Human
Sedlin 1966	1 week	105	Significant change	"	"	Human
Hoffler 2005	Unclear	Air	22.6% increase	Nanoindent.	500 nm depth	Human

These previous works examined the effects of dehydration on bone mechanics by critically evaluating samples at relatively large length scales. Mechanical testing of bone at smaller length scales is advantageous when local property measurements and, particularly in this work, the mechanical properties of the lamellar unit material are required. Nanoindentation has proved to be the most widely used technique for probing mechanical

properties of bone at micron to sub-micron length scales with a comprehensive review of nanoindentation (Lewis & Nyman 2008) highlighting local mechanical property measurements and effects of dehydration. In particular, nanoindentation at numerous positions across an osteon within human cortical bone revealed a lower elastic modulus of the wet bone relative to the dehydrated state (Hoffler et al. 2005). Individual bone trabeculae from cancellous human vertebrae also showed an increase in elastic modulus with dehydration (Wolfram, Wilke & P.K. Zysset 2010).

The general trend in both large and small scale mechanical testing reveals an increase of the elastic modulus of bone with dehydration and a corresponding lowering of the work to fracture. This observation is irrespective of the testing method used, with bending tests employed extensively at macroscopic sample length scales and indentation employed at micron length scales. The lack of scaling effects in mechanical property changes in bone with dehydration suggests that water content affects the mechanical properties, as indicated by Nyman et al. (Nyman et al. 2006), and does not depend on bone structural hierarchy.

Nyman et al. proposed a mechanism to describe the effects on bone mechanical properties due to water loss during dehydration for human cortical bone (Nyman et al. 2006). Bone samples held at room temperature showed similar elastic moduli to hydrated bone with slight increases in bending strength and loss of toughness. Samples dried at higher temperatures showed an increase in the elastic modulus compared to

hydrated samples. Increasing temperatures had an accelerating effect on losses in bone toughness and a distinct decrease in strength. Nyman et al. proposed a mechanism where water loss in collagen causes a lowering of bone toughness but water loss at mineral surfaces decreases both bone toughness and strength. An energy-based approach explained how binding of water to mineral is stronger than water-collagen binding. Thus, higher temperatures remove water in collagen and at mineral surfaces but lower temperatures only remove water from the collagen.

Nuclear Magnetic Resonance (NMR) studies have provided further support for the model of Nyman by defining three states of water within bone (Wilson et al. 2006). The first state is free water found in bone pores such as Haversian and Volkmann's canals, canaliculi and lacunae (Yan et al. 2008). This water is expected to play only a minor role in the mechanical properties of bone and its removal during dehydration is not accounted for by Nyman et al. (Nyman et al. 2006). The second state is water loosely bound to collagen via hydrogen bonds; this water fraction can be removed at room temperature and acts as a plasticizer, which protects the collagen by reducing the stress transferred during mechanical loading of the bone (Nyman et al. 2006; Wilson et al. 2006). Reducing the stress transfer allows the components, in this case the collagen and the mineral, to slide and avoid failure. Conversely a high stress transfer indicates a strong binding of the components, which would be effective in transferring the loads throughout the bone. Failure of the bone composite will occur when these applied loads are high. The result of an increased stress transfer, from the loss of the second water state, is a

reduction in bone toughness due to lack of collagen plasticization. Finally, the third state of water is mineral-bound structural water that has been shown to exist in the imperfect carbonated apatite crystal lattice, providing stability via hydrogen bonding with neighbouring ions and by preventing the crystallites from collapsing or rearranging. The removal of this water occurs only at higher temperatures and has been shown to destabilize the mineral and cause significant strength reductions of the bone (Nyman et al. 2006; Wilson et al. 2006; Yan et al. 2008). The triple helix of tropocollagen additionally loses stability if the water molecules forming a highly ordered network with the tropocollagen were removed. The tropocollagen stability arises from the formation of additional water-mediated hydrogen bonds in the remaining backbone peptide groups, which would not exist without water due to spatial constraints (Bella, Brodsky & Berman 1995; Beck & Brodsky 1998; Wilson et al. 2006; Yan et al. 2008). Further dehydration models have been suggested based on the amount of mineral present within the bone material (Currey 1999; Wilson et al. 2006; Currey et al. 2009). Specifically, bone biomineralization occurs when mineral replaces water so that bone with low mineral content will contain more water than highly mineralized bone. Dehydration processes will therefore cause more structural, and thus mechanical, changes in bone with relatively low mineral content (Currey 1999; Utku et al. 2008).

The studies detailed above examine the dehydration of bone and the corresponding effects on its mechanical behaviour, yet little work has been done to examine the effects of vacuum conditions on bone structure. The

vacuum condition is important in many cases where electron microscopy is employed, such as in this work. Observation of water loss from various regions resulting in dimensional contractions in bone has been directly observed by environmental scanning electron microscopy (ESEM) (Utku et al. 2008) but the corresponding effects on mechanical behaviour have been lacking. The evaluation of bone mechanics using techniques involving SEM has distinct advantages compared to previous works. Principally, observation and manipulation of relatively small volumes of bone can be achieved using the SEM, potentially in conjunction with other testing methods such as in situ mechanical testing (Koester, Ager & Ritchie 2008; Hang et al. 2011), in order to evaluate the properties of bone material. The mechanical testing of these relatively small volumes is advantageous when compared to larger scale testing as structural hierarchy effects can be potentially ignored or simplified. Such simplification allows the study of the material properties of bone and not whole bone behaviour. Discrete bone volume mechanical testing can also be used in order to assess the effects of the SEM vacuum chamber on potential structural changes in bone due to water removal as is the main focus of this chapter.

Recent literature has additionally illustrated the use of focussed ion beam (FIB) microscopy to isolate micron-sized cantilevers from teeth for subsequent bending tests (Chan, Ngan & King 2009). The dual beam system setup allows FIB technology to be incorporated with a scanning electron microscope (SEM) which is typically used for structural investigations (Utku et al. 2008). The capacity to isolate discrete bone volumes within a dual

beam system using the FIB and observe structural changes using SEM is therefore persuasive, especially as typical mechanical testing at relatively small length scales provides mechanical information while this setup allows for structural features to be examined concurrently. Critically, dual beam instruments operate in partial vacuum, which could dehydrate bone material. Previous work has used an atomic force microscope (AFM) within a dual beam system to mechanically test individual collagen fibrils from antler bone within a vacuum environment (Hang & Barber 2011). Experimental data from Hang and Barber was shown to be similar to fully hydrated antler bone deformation behaviour recorded using small angle x-ray scattering (Krauss et al. 2009), indicating that dehydration of bone in a vacuum chamber does not have an effect on the mechanical properties at nanometre length scales. This thesis extends mechanical testing of bone material further by using a combination of AFM and dual beam system to bend cantilever micro-beams of bone. Chapter 4 examines the effects of different environmental conditions on the mechanical properties of bone at micron length scales using AFM while observing in situ using SEM. The results and discussions in this chapter will validate the testing performed throughout this thesis.

4.2 Materials and methods

Tensile testing is the typical mechanical test employed in order to characterize a material but there are often associated difficulties in performing this test at small length scales approaching the micro level.

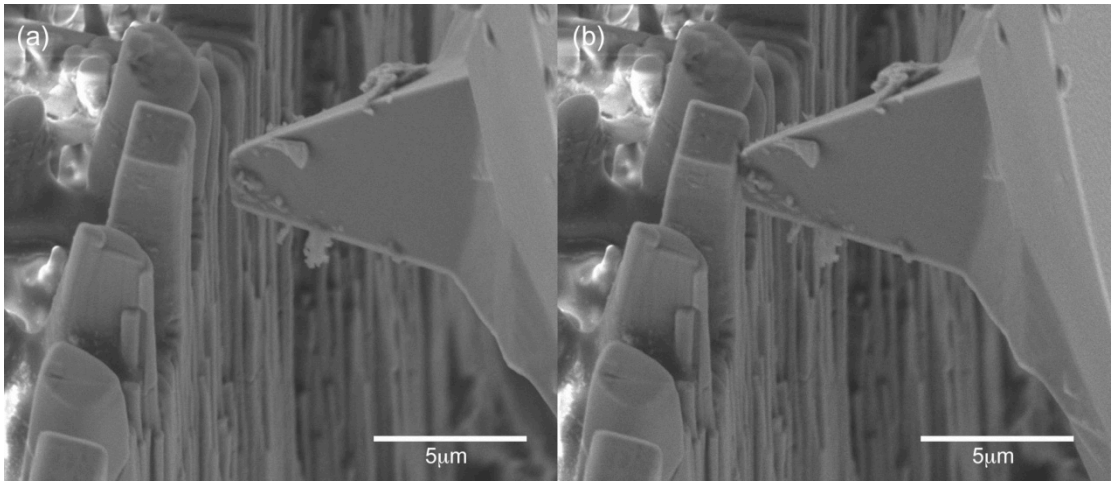

Figure 4.1 SEM micrographs showing a) the AFM tip before contact with an individual rat bone beam and b) contact of the tip with the rat bone beam for mechanical bending tests.

Therefore, most researchers select bending as a more suitable testing method, primarily because gripping of the sample is not required is bending (An & Draughn 2000). A cantilever-bending mode was chosen due to the constraints of the sample size and ability to produce a cantilever in the bone material detailed in the previous chapter. Figure 4.1 shows an SEM image of the AFM bending tests on an individual bone micro-beam. The bone micro-beam was deformed using a FIB flattened AFM tip, to avoid AFM tip indentation into the sample.

In order to test the effect of different environmental conditions on the mechanical properties of bone material, cantilever micro-beams were created following the methods described in Chapter 3. The rat bone sample with patterned micro-beams was fully rehydrated as described in the previous chapter and placed on the sample stage of the custom built AFM

system (Attocube GmbH, Ger.). The AFM was then moved to within the SEM chamber for subsequent AFM mechanical testing while monitoring in situ using the SEM. Mechanical testing of the bone micro-beams was performed using a bending configuration as shown in Figure 4.1 and Figure 3.11 using the AFM. Each bending test was performed to small micro-beam deflections of ~1.5 μm, at a rate of 0.04 $\mu m.s^{-1}$ with a FIB flattened AFM cantilever tip with a spring constant of 28 $N.m^{-1}$.

Mechanical bending testing of the bone micro-beams was performed at two minute intervals for an initial period of 1 hour followed by testing every 15 minutes for another hour. All bending experiments were performed in each of the following environments: i) high vacuum ($5.25x10^{-4}$ Pa) in the chamber of the dual beam system, ii) low vacuum (120 Pa pressure provided by water vapour within the SEM chamber operating under environmental mode) in the chamber of the dual beam system and iii) wet in air, which was achieved by the removal of the sample from the vacuum chamber for beam bending in air. This last 'wet in air' environment was achieved by removing the sample and AFM system from the vacuum chamber and covering in a closed vessel containing paper soaked in Hank's buffered solution. The covered environment was allowed to saturate with water vapour for 2 hours before bending of the micro-beams in the water vapour environment. A total of three cantilever micro-beams were tested in all three environments. The testing procedure took a total of 12 hours for each beam: two hours of testing in each environment with intervals of two hours inside the closed vessel with

a high vapour concentration of Hank's buffer solution in order to rehydrate the samples before each test.

In order to assess the rehydration processes used in this thesis, the weight of whole 2 mm thick cross-sections of diaphysis of rat femora were measured following the same preparation process as described for the micro-beam samples in Chapter 3. Table 4.2 records the weight loss measured for three different rat femora cross sectional slices subjected to the various environments used in the experimental preparation. Bone samples were initially held in Hank's buffer solution for 2 hours. The bone samples were removed from the solution and, after removing excess surface water with filter paper, weighed using an electronic analytical microbalance (Sartorius, Ger.) to 4 significant figures. The weights of these bone samples were taken as fully hydrated bone weight. Further preparation processes were recorded by the percentage of weight lost by the bone samples relative to this fully hydrated bone weight as shown in Table 4.2.

The bone samples were first exposed to ethanol treatments, as indicated in Table 3.1, and resulted in a bone weight loss of approximately 3%. Exposure to the vacuum conditions of the SEM chamber used for FIB milling caused a further 9% weight loss in the bone samples.

Table 4.2 – Change in weight, as a percentage of the weight difference relative to bone rehydrated in Hank's Buffer solution. The cycle of hydration represented by the table was repeated on three separate rat bone femur cross sections.

	Time	**Loss in bone weight relative to when hydrated in Hank's buffer solution (%)**
From Storage in Ethanol 70%	Storage (few months)	2.29±1.07
Soaked in Hank's buffer solution	2 hours	0
Dehydrated (see Table 3.1)	3.5 hours	3.29±0.5
Vacuum dried (High Vacuum $1.51x10^{-3}$ Pa)	2 hours	9.27±0.47
Rehydrated in closed vessel with high vapour concentration of Hank's buffer solution	2 hours	3.63±0.49
Vacuum dried (High Vacuum $1.51x10^{-3}$ Pa)	2 hours	9.97±0.55*
Rehydrated in closed vessel with high vapour concentration of Hank's buffer solution	2 hours	3.7±0.27*

*We note that samples placed in vacuum and rehydrated three times gave these repeatable weight loss values.

The total weight loss from the bone samples during the ethanol and vacuum exposure was 12.56±0.97%. Previous literature indicates that up to 12% weight loss during dehydration of bone is due to the removal of free water from pores such as Haversian and Volkmann's canals, canaliculi and lacunae (Nyman et al. 2006; Yan et al. 2008). The initial bone weight loss of 3% during ethanol treatment therefore indicates a partial removal of the free water in bone whereas exposure to the SEM vacuum removes the remaining free water. Rehydration of bone samples for two hours in a high vapour concentration of Hank's buffer solution recovers some of the free water and reduces the weight loss of bone to 3.63±0.49% relative to the fully hydrated

bone weight. Repeating the bone exposure to vacuum conditions removes all of the contained free water, resulting in the total bone weight loss of 12%. Repeating the rehydration of bone and subsequent vacuum exposure produced repeatable weight loss values, as would be expected if the rehydrating conditions replacing water and the bone vacuum conditions removing the water were consistent. We therefore conclude that the rehydration and dehydration processes remove free water only and not the other, bound states of water in the bone.

4.3 Results and discussion

The force-displacement curves for one of three rat bone beams tested in bending in high vacuum, low vacuum and wet in air after 10 minutes of exposure to each environment are shown in Figure 4.2. The bending tests were conducted up to beam displacement of ~1.5 μm, and show a linear force-displacement relationship. The gradient of the linear region ($df/d\delta$) of the force-displacement curves in Figure 4.2 can be used to calculate an effective elastic modulus of the rat bone beam E, using:

$$E = \frac{12l^3}{3bh^3} \cdot \frac{f}{\delta} \qquad \text{Eqn. 24}$$

Where *l*, *b* and *h* are the length from the base of the sample to testing contact point, breadth and height of the rat bone beam respectively. Typical geometric values of the rat bone beam are *l*=10 μm, *b*=2 μm and *h*=2 μm.

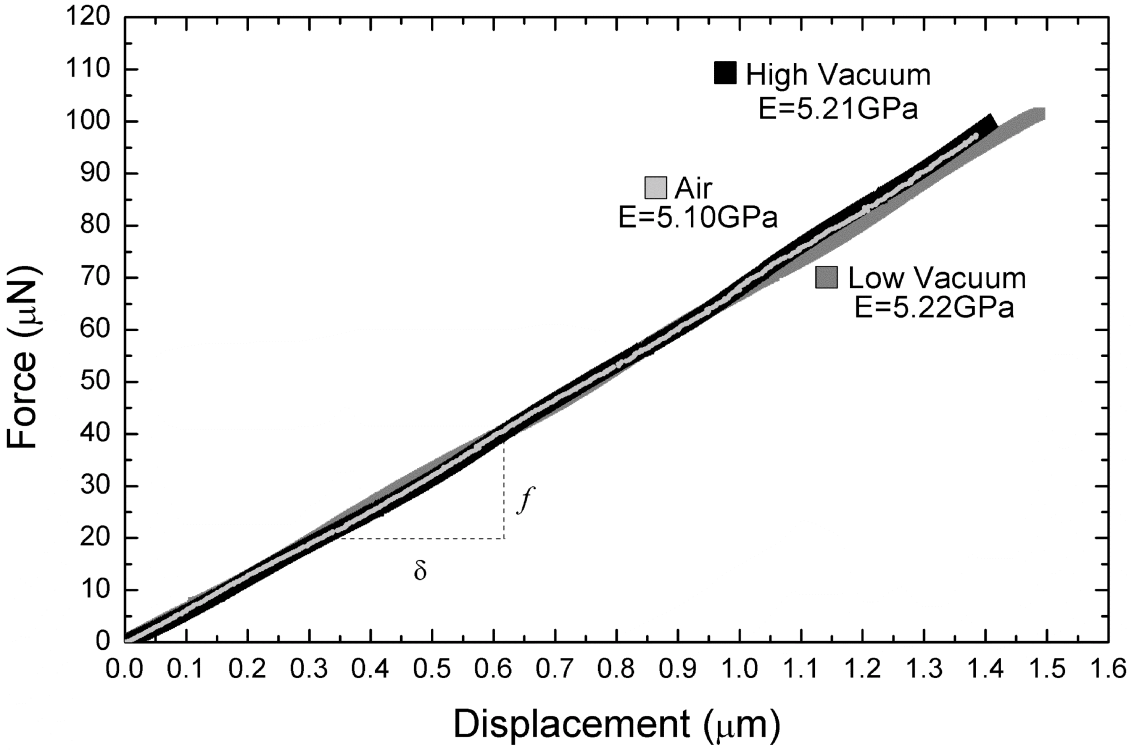

Figure 4.2 Force-displacement plot for AFM mechanical bending of a rat bone micro-beam tested under high vacuum, low vacuum and wet in air environments.

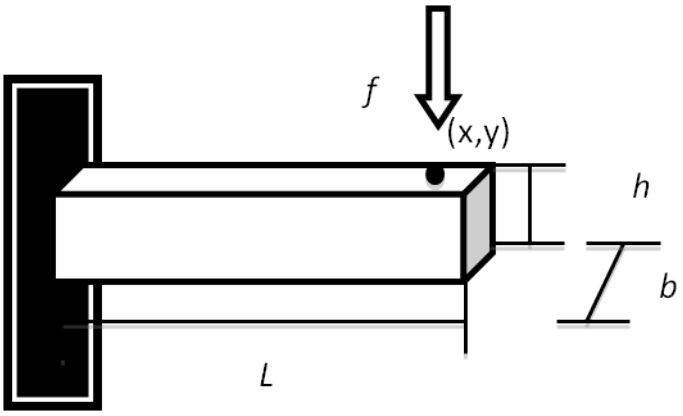

Figure 4.3 Schematic of a rectangular beam of length *L*, breadth *b* and height *h* bending under an applied load *f*.

The elastic modulus of a deflected beam can be found by knowing the dimensions of the beam and the applied load *f* as shown in Figure 4.3 above. Liu, 1999 (Liu, Weiner & Wagner 1999) used Equation 32 below to calculate the bending modulus of small cylindrical bone cantilever beams. If (*x, y*) are the x and y coordinates for the applied load on the micro-beam respectively, δ is the micro-beam deflection, k_b is the spring constant for the bone micro-beam in bending and Slope is the gradient from the AFM force-displacement (f/δ) curve in Figure 4.2, then we can derive:

$$\sigma = \frac{My}{I} \qquad \text{Eqn. 25}$$

where $$M = f(L - x) \qquad \text{Eqn.26}$$

and $$I = \frac{1}{12} bh^3 \qquad \text{Eqn. 27}$$

$$\delta = \frac{k_b f l^3}{EI} \qquad \text{Eqn.28}$$

$$Slope = \frac{f}{\delta} \qquad \text{Eqn. 29}$$

$$E = \frac{1}{3} \cdot \frac{l^3}{I} \cdot \frac{f}{\delta} \qquad \text{Eqn. 30}$$

$$E = \frac{1}{3} \cdot \frac{l^3}{I} \cdot Slope \qquad \text{Eqn. 31}$$

Therefore for a cylindrical cantilever beam in bending, the formula for the bending modulus is:

$$E = \frac{64 l^3}{3\pi D^4} \cdot Slope \qquad \text{Eqn. 32 (Liu, Weiner \& Wagner 1999)}$$

But, as mentioned before, for a rectangular cantilever beam in bending the formula to calculate the bending modulus is:

$$E = \frac{12 l^3}{3 b h^3} \cdot \frac{f}{\delta} \qquad \text{Eqn. 24}$$

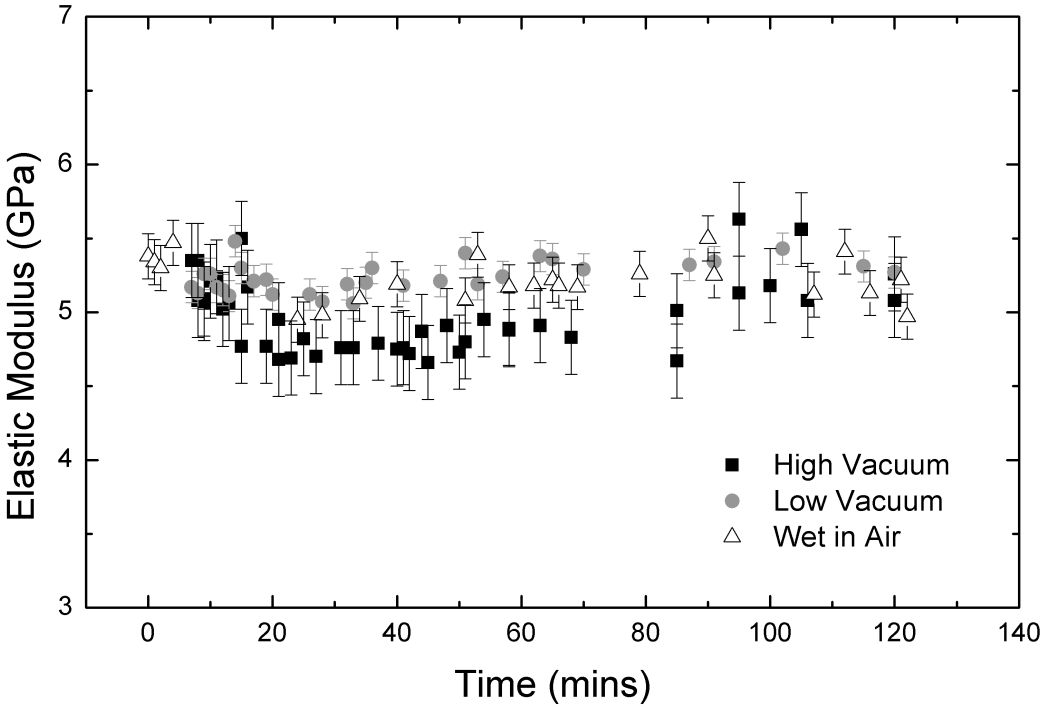

Figure 4.4 Plot of elastic modulus calculated from Equation 24 and determined from AFM bending of one of the three rat bone beams, with time under high vacuum, low vacuum and wet in air environments.

Typical force-displacement curves for bending rat bone beams in high vacuum, low vacuum and air after 10 minutes of exposure to each environment are shown in Figure 4.2. The calculated elastic modulus values for the rat bone beam tested under different environmental conditions are shown in Figure 4.4, with the error in E values calculated from the standard deviation of the values for the elastic modulus arising from the changes of

the contact point during testing. The elastic modulus shows little change either with environment or time of exposure in the SEM chamber. This observation is true for all micro-beams tested in cantilever bending.

The results of the effect of the environment on the elastic modulus of bone discussed in this chapter are somewhat surprising as an increase in the elastic modulus is expected because of dehydration effects (Hoffler et al. 2005; Nyman et al. 2006; Wilson et al. 2006; Lewis & Nyman 2008; Currey et al. 2009; Morais et al. 2010). Figure 4.4 indicates that the elastic modulus of the rat bone beam in high vacuum is 4.98±0.25 GPa, low vacuum is 5.24±0.11 GPa and air is 5.22±0.15 GPa and does not vary greatly over the time period examined. Previous mechanical testing on fully hydrated whole rat bone femur using 3-point bending configuration gives an elastic modulus of 5.12±0.77 GPa (Kasra et al. 1997), 8.0±0.4 GPa (Barengolts et al. 1993), 6.88±0.31 GPa (Jorgensen, Bak & Andreassen 1991), and 4.9±0.4 GPa (Ejersted et al. 1993) which is similar to the calculated elastic modulus values in our work and indicates that the vacuum chamber does not have an effect on elastic modulus of the samples over the time period investigated. Interestingly, the similarity between the elastic modulus of our relatively small bone volumes and whole bone testing suggests an effective transfer of stresses throughout bone. Potential errors in the determination of the elastic modulus of the bone micro-beams from bending tests may arise due to the aspect ratio of the bone beams produced and AFM tip penetration into the micro-beam during bending testing. Specifically, bending of beams with an aspect ratio of at least 10:1 are typically used for 3-point bending (Sedlin & Hirsch 1966; Chen, Stokes & McKittrick 2009; Currey et al. 2009). Beams with potentially smaller aspect ratios may give inaccurate calculated elastic modulus values using Equation 24 as shear within the beam may be

significant. Using classic beam bending theory (Blodgett 1991), the deflection of the beam consists of a deflection due to shear and a deflection due to bending. The total deflection can therefore be written as:

$$\delta = \delta_{bending} + \delta_{shear} = \frac{fl^3}{3EI} + \frac{6fl}{5AG} \qquad \text{Eqn. 33}$$

Where δ is total beam deflection, f is the force applied to the beam, l is the beam length, E is beam elastic modulus, I is the moment of inertia of the beam, A is the beam cross sectional area and G is the beam shear modulus which is calculated theoretically from $G=E/[2(1+\nu)]$, with ν = 0.35 (Akiva, Wagner & Weiner 1998). The beams used in this work have an aspect ratio of 5:1. Therefore, using Equation 33 above, the shear contribution to the total deflection is ~3.5%. This shear contribution is much smaller than the bending contribution, indicating that the majority of beam mechanical deformation results from pure bending. We believe that therefore that the aspect ratio of the bone beams used here is sufficient for bending experiments, as the shear contribution is minor. The second source of error when calculating the elastic modulus of the micro-beams in bending using AFM is possible indentation of the AFM tip with the bone beam sample. However, neither direct SEM imaging of the mechanical testing procedure or subsequent SEM examination of the AFM tip-sample contact point showed evidence of indentation on the surface of the cantilever bone beams being tested.

4.4 Conclusions

Small scale mechanical testing of bone materials was performed in a variety of different environments. The lack of environmental influence on the mechanical properties of the bone micro-beams indicates that the water content is constant in all mechanical testing cases. Samples exposed to the high vacuum would be expected to provide the largest removal of water but the similar bone elastic modulus in all cases shows that the vacuum driving force is not sufficient to remove the water within the tested beam volumes. While previous work has shown changes in the elastic modulus with dehydration time (Hoffler et al. 2005; Nyman et al. 2006; Wilson et al. 2006; Lewis & Nyman 2008; Currey et al. 2009; Morais et al. 2010), the attempted vacuum drying of bone in this work and oven drying in previous literature cannot be directly compared due to the different dehydration process. However, Utku et al. (2008) have shown that water is lost from bone in vacuum chambers by measuring the changes in dimension with time inside the chamber, attributing the expansion and shrinkage of the bulk bone sample cross section to water content. Our recorded bone elastic modulus values suggest that water removal responsible for mechanical property changes during dehydration operate at length scales above the micro-beams used in this work. Thus, while dehydration removes water in whole bone, with a resultant increase in the elastic modulus of bone, the smaller bone volumes mechanically tested in this work do not contain such water. The discrete volumes tested in this work must therefore contain bound water, which is not removed in any of the environmental states. Our results

indicate that the second and third states of bound water, as defined by Nyman et al (Nyman et al. 2006), in collagen and at mineral surfaces in bone respectively are not removed even with the highest vacuum conditions of the SEM. The SEM high vacuum conditions must also be less evasive than higher temperatures reported in the range of 60-140°C used to remove water during complete collagen dehydration (Renugopalakrishnan et al. 1989). We can conclude that the environmental conditions used for mechanical testing of the bone micro-beams are adequate within the timescales examined in this chapter. Subsequent chapters will exploit the robust AFM mechanical testing procedure to examine the lamellar unit of bone in detail and develop structure-mechanical function relationships.

Chapter 5. Effect of bone lamellae orientation on elastic properties of bone

5.1 Introduction

Bone is a natural composite material and possesses a structural complexity across a range of length scales. This structural complexity allows bone to maintain biological function while performing a number of mechanical roles (Wainwright et al. 1982; Fratzl & Weinkamer 2007). The different structural organizations found at various length scales makes the determination of bone mechanics challenging. Of all the structural features, the lamellar unit present over micron length scales is of significant importance in bone mechanics as this unit is used extensively to build many larger bone structures. Lamellae also contain the fundamental components of bone, including collagen predominantly in the form of fibrils, hydroxyapatite platelets, non-collagenous protein and water, and is often referred to as the building block of bone (Gupta, Stachewicz & Wagermaier 2006). The lamellar unit can be considered as a three phase composite material with plate-like hydroxyapatite minerals reinforcing collagen fibrils bound together in a relatively small volume fraction of non-collagenous proteins (Akiva, Wagner & Weiner 1998). These hydroxyapatite minerals are plate-shaped and embedded within and around the collagen fibrils, with the principal axis of the mineral oriented in the same direction as the long axis of the collagen fibrils (Wagner & Weiner 1992; Landis et al. 1996; Fratzl et al. 2004;

Wagermaier et al. 2006). Thus, the organization of the collagen fibrils within the lamellar unit defines the mineral orientation within this same unit. The orientation of collagen fibrils and, thus, the mineral phase in the lamellar unit can be described by five subunits, with each subunit composed of an array of aligned mineralized collagen fibrils with an offset of around 30° to each other as shown in Figure 5.1. The orientation of the sub-layers has been shown to conform to a rotated plywood-like structure and can be generally grouped into two subunits (Liu, Weiner & Wagner 1999; Gupta, Stachewicz & Wagermaier 2006; Boyd & Nigg 2007); the 'thick' subunit where the collagen fibrils run parallel or at 30° to the long axis of bone, thus contributing significantly to the elastic modulus (Ascenzi, Benvenuti & Bonucci 1982), and the 'thin' subunit for fibrillar arrays oriented at 60°, 90° and 120° to the long axis.

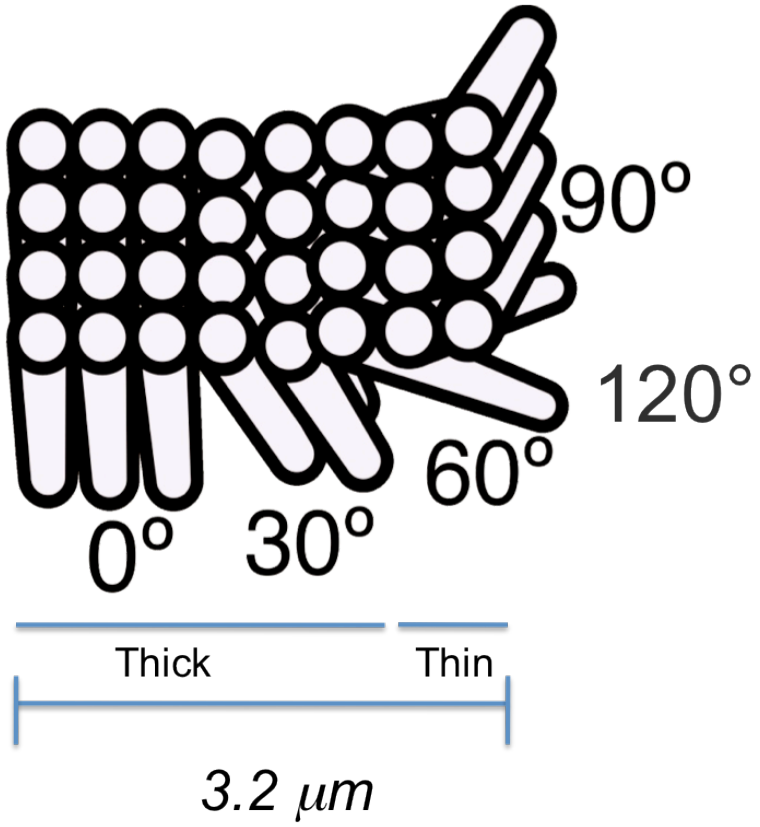

Figure 5.1 Schematic showing mineralized collagen fibril layers at 0°, 30°, 60°, 90° and 120° orientations relative to the long axis within the lamellar unit of bone.

The overall mechanical properties of bone depend on both the volume fraction of components, most notably mineral phase, and the organization of these components represented by the lamellar unit. Previous works have indicated the importance of the mineral phase in defining overall bone mechanical behaviour by direct investigations on mineral volume fraction in a variety of different bone samples (Currey 2002). A general increase in the elastic modulus of bone was correlated with an increase in the mineral volume fraction but a number of exceptions were noted where the mineral volume fraction alone does not determine the mechanical properties of bone.

Currey suggested a mineral organizational factor that further defined the effectiveness of the reinforcement in bone, which has also been considered by Rho et al. (Rho, Kuhn-Spearing & Zioupos 1998) and Sasaki et al. (Sasaki, Ikawa & Fukuda 1991). The mechanical properties of bone are therefore not determined solely by mineral volume fraction but by both the mineral content and the mineral platelet orientation defined by the collagen fibril orientation (Sasaki, Ikawa & Fukuda 1991). This fibril orientation will therefore give rise to mechanical anisotropy in bone material.

The influence of component organization on bone mechanical behaviour was conclusively highlighted in studies on individual osteons. Polarized light microscopy was previously used to identify collagen fibril orientation and related to the mechanical properties of individual osteons in tension (Ascenzi, Benvenuti & Bonucci 1982), bending (Ascenzi & Bonucci 1990) and compression (Ascenzi & Bonucci 1968). Increases in the elastic modulus of individual osteons were found to occur when the majority of the collagen fibrils were oriented in the loading direction and supported theories that established the existence of lamellar orientations in bone material (Ascenzi, Bonucci & Ds. 1965) (Giraud-Guille 1988). Further works have more specifically highlighted the relationship between overall bone mechanics and collagen fibril orientation, including increased tensile strength (Martin & Ishida 1989) and higher elastic modulus (Riggs et al. 1993; Ramasamy & Akkus 2007) when collagen fibrils are predominantly oriented along the longitudinal, as opposed to the transverse, loading direction. The importance of the collagen fibril orientation in determining overall bone mechanical

properties led to mechanical testing at smaller sub-microstructural length scales. In particular, direct mechanical testing of bone at sub-millimetre length scales using indentation has been previously achieved in order to determine the effect of lamellar orientation on the mechanical properties of baboon tibiae (Liu, Weiner & Wagner 1999). The results of this work indicated a clear anisotropic behaviour at different spatial positions along a bone fracture surface, and inferred lamellae orientation from mechanical behaviour. Further improvements to measure the mechanical properties of bone at the sub-microstructural level have been attained through nanoindentation, which allows localized testing to be performed on individual components such as individual lamellae (Xu et al. 2003; Gupta, Stachewicz & Wagermaier 2006; Lewis & Nyman 2008). The plywood collagen organisation within the lamellar unit has also been shown to act as a crack blunter to enhance toughening mechanisms at this sub-microstructural level (Gupta, Stachewicz & Wagermaier 2006; Peterlik et al. 2006). However, structural heterogeneities in bone coupled with the complex stress analysis formed from indentation of bone surfaces make direct understanding of bone component mechanics particularly fraught (Xu et al. 2003; Gupta, Stachewicz & Wagermaier 2006; Isaksson et al. 2010). A comprehensive review of nanoindentaton in mineralized tissue particularly emphasizes problematic issues of indentation-sample contact area, critical in determining mechanical properties of samples, as an unexplored area of study (Xu et al. 2003; Gupta, Stachewicz & Wagermaier 2006; Lewis & Nyman 2008). Further determination of mechanical properties of components has been more

recently available with the advent of more sophisticated, and higher force resolution, techniques that are able to elucidate component mechanics directly. Such components have been investigated by a series of experiments such as nanoindentation (Tai et al. 2007), AFM scraping and indenting (Wenger et al. 2007; Wenger, Horton & Mesquida 2008) and tensile testing of individual mineralized collagen fibrils (Hang & Barber 2011).

Variations in the mechanical properties of bone when testing at different orientations to the bone's long axis are considered to be mainly due to the alignment of the collagen fibrils and mineral plates relative to the loading axis, and highlight the influence of the lamellar unit on overall bone mechanical behaviour (Martin & Ishida 1989; Riggs et al. 1993; Fratzl et al. 2004; Ramasamy & Akkus 2007). Understanding the mechanical properties of the lamellar unit and the effects of orientation within the lamellae therefore provides a link between component and overall bone mechanical performance. While mechanical properties of components are instructive in defining overall bone behaviour, testing of bone at larger length scales approaching a few microns perhaps best represent the synergy between the components in bone material but ignore the higher order structural effects such as osteonal canals or the curvature of whole bone. However, the synergy between the individual bone components even at these relatively small length scales is poorly understood. This chapter attempts to evaluate the mechanics of the sub-lamellar unit through the study of rat femora. Considering that the width of a lamellar unit of rat bone is ~3.2 μm (Weiner

et al. 1997; Akiva, Wagner & Weiner 1998), mechanical testing on discrete units of bone below this length scale is attempted. These sub-lamellar units will provide understanding of bone mechanics as a composite material both through consideration both of the bone components and the organization of these components within the lamellar unit.

5.2 Materials and methods

Rat femora where sliced, dehydrated, mounted, gold coated, FIB milled and tested in situ in cantilever bending as described in Chapter 3 and 4, sections 3.3, 3.4 and 4.2. The mechanical testing follows the same procedure as the one described in Chapter 4 section 4.2 except that only the data from the bending tests at high vacuum were used for the purpose of the analysis in this chapter. The results of the sample preparation are shown in Figure 5.2 below and indicates the location of the micro-beams in reference to the whole sample.

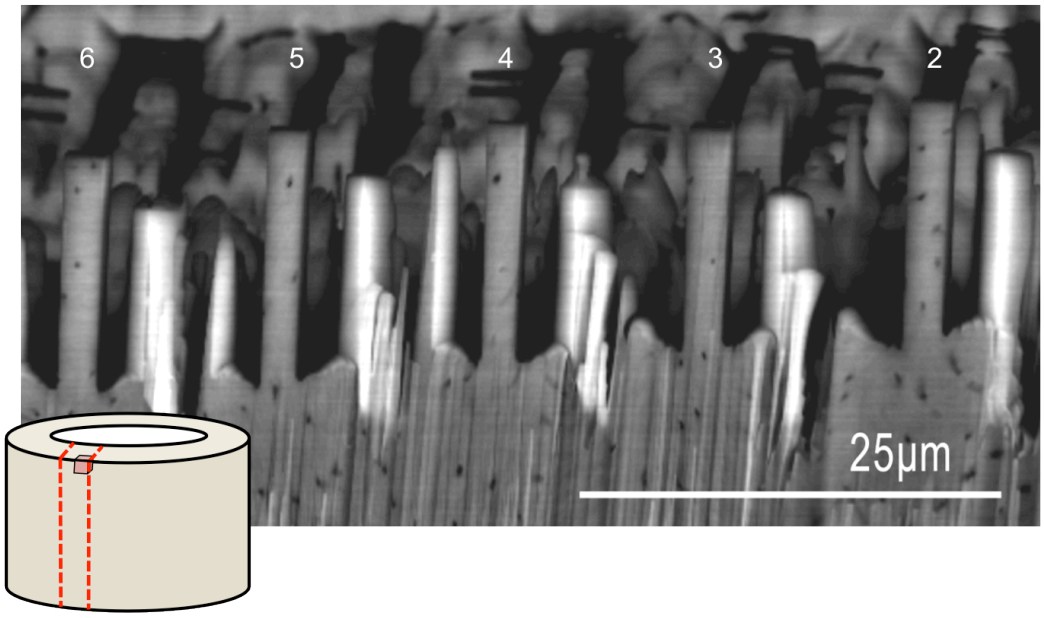

Figure 5.2 SEM back-scattered image of bone micro-beams produced at the edge of a bone sample as indicated in the insert. The dotted line marks how the diaphysis of the rat femur was sliced and the cube on the top edge of the slice shows where the micro-beams were milled. The beams shown are micro-beams 2-6 from right to left.

The key element of the sample preparation in this chapter is the polishing step that reveals fine details in the bone structure using SEM back-scattered electron imaging as shown in Figure 5.3. Details of the FIB milling are given in Chapter 3, with particular emphasis on the final FIB milling step at a low current of 0.1 nA, as it resembles polishing, which provides particularly flat surfaces for back-scattered imaging. All images were taken before mechanical testing with a BSED detector inside the SEM (FEI, U.S.A./E.U.) operating at an accelerating voltage of 10 kV.

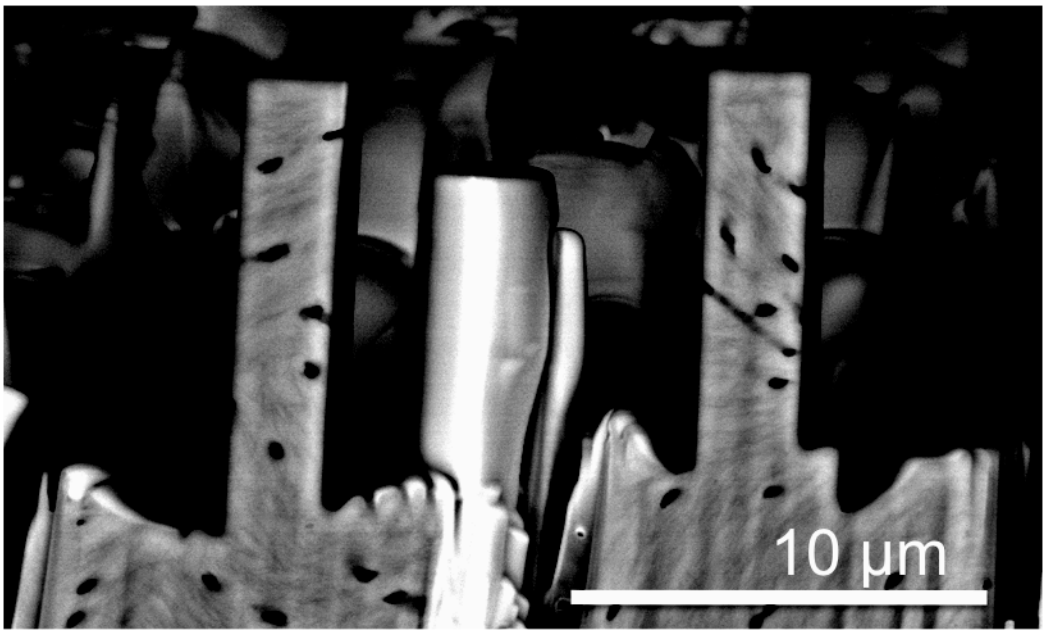

Figure 5.3 SEM back scattered secondary electron image of bone micro-beam samples.

The resultant FIB process allowed the fabrication of micro-beams with dimensions of ~10x2x2 µm as shown in Figure 5.4, with the long axis of the cantilever beam parallel to the long axis of the rat femur. Testing of the beams within the SEM chamber was carried out within a time-frame of 2 hours. Chapter 4 and published work (Jimenez-Palomar et al. 2012) has indicated that micro-beams of bone remain hydrated within the vacuum chamber of an SEM within the testing time-frame of this work.

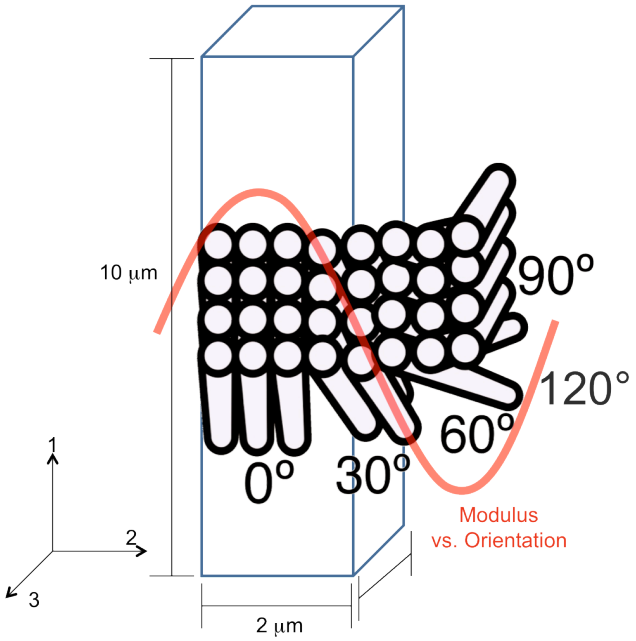

Figure 5.4 Schematic showing the approximate dimensions of the sub-lamellar unit in bone material produced using FIB techniques. The FIB milled bone micro-beam width is 2 μm, which is below the width of a single lamellar unit, thus indicating that the testing is sub-lamellar. In the diagram, the micro-beam contains part of the lamellar unit with the collagen fibril orientation predominantly along the long axis of the micro-beam, which will result in a elastic modulus maxima for the micro-beam.

The bone micro-beams were deformed using a FIB flattened AFM tip (ACT, AppNano, U.S.A.), using an AFM cantilever spring constant of 28 $N.m^{-1}$, measured using the Sader calibration method (Sader et al. 1995). FIB was used to flatten the tip of the AFM tip prior to mechanical testing to avoid AFM tip indentation into the sample. Bending of the micro-beams was achieved by applying a beam displacement of up to 1.7 μm at an approximate testing rate of 0.04 $\mu m.s^{-1}$. Each beam was tested 25 times over a period of 2 hours.

5.3. Results and discussion

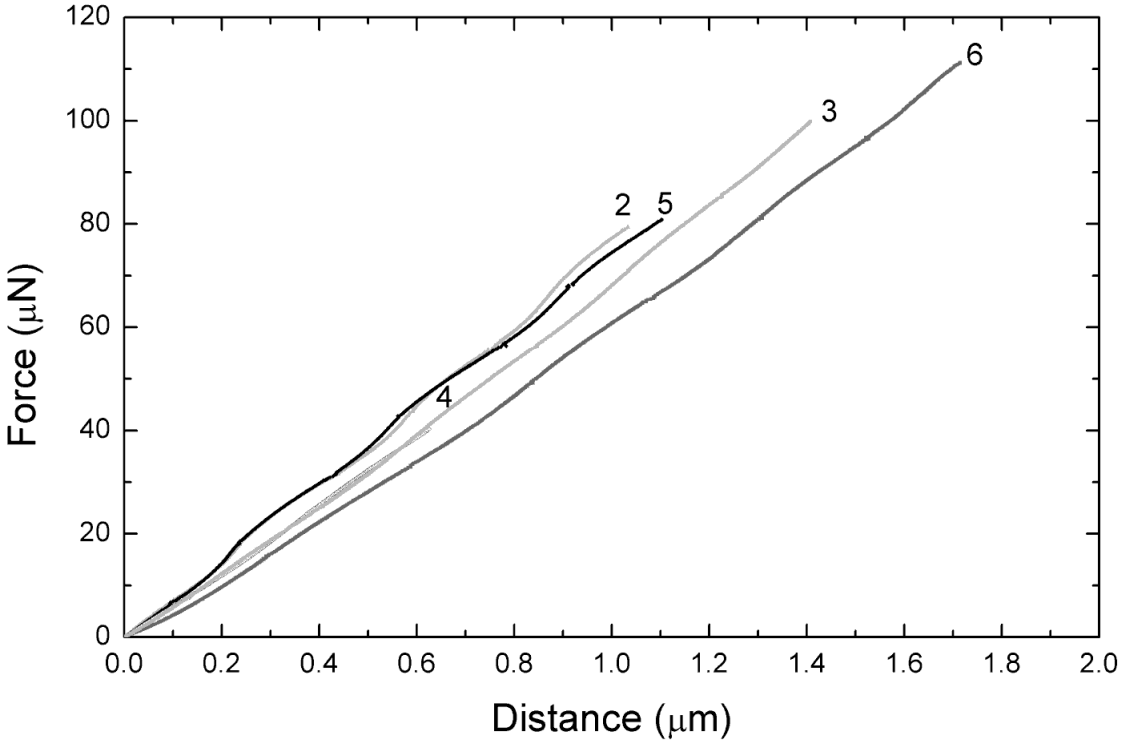

Figure 5.5 Force distance curves of the 5 micro-beams tested in cantilever bending, corresponding to the results in Table 5.1.

Force-displacement curves for the 5 micro-beams tested using AFM are shown in Figure 5.5. A linear force-displacement relationship was observed during beam bending, indicating elastic behaviour. The gradient of the linear region ($df/d\delta$) of the force-displacement curves can be used to calculate an effective elastic modulus of the rat bone beam, E, using Equation 24 found in Chapter 4 section 4.3. Typical geometric values of the micro-beam are l=10 μm, b=2 μm and h=2 μm.

The elastic modulus values calculated from Equation 24 for the five different micro-beams against the distance between each beam are shown in Figure 5.6. The error in E values was calculated from the standard deviation of the

values for the elastic modulus caused mainly by small changes in contact point along the length of the micro-beams.

Figure 5.6 is a plot of the variation in elastic modulus against beam position at the edge of the bone sample as measured from the SEM image. The expected structural periodicity arising from the mineralized collagen fibril layer orientations is fitted to the plot as shown by the red sine curve. There is a clear correlation between the variations of the elastic modulus with distance and the expected theoretical periodicity of the lamellar unit of rat bone, which has been identified as a repeating unit of 3.2 μm. This repeating unit of fibre orientation, rotating from 0° to 90° where 0° is along the long axis of the bone and 90° perpendicular to the long axis of bone. This changing fibre orientation causes a change in elastic modulus as demonstrated in Figure 5.6 and by previous research by Gupta et al. (Gupta, Stachewicz & Wagermaier 2006).

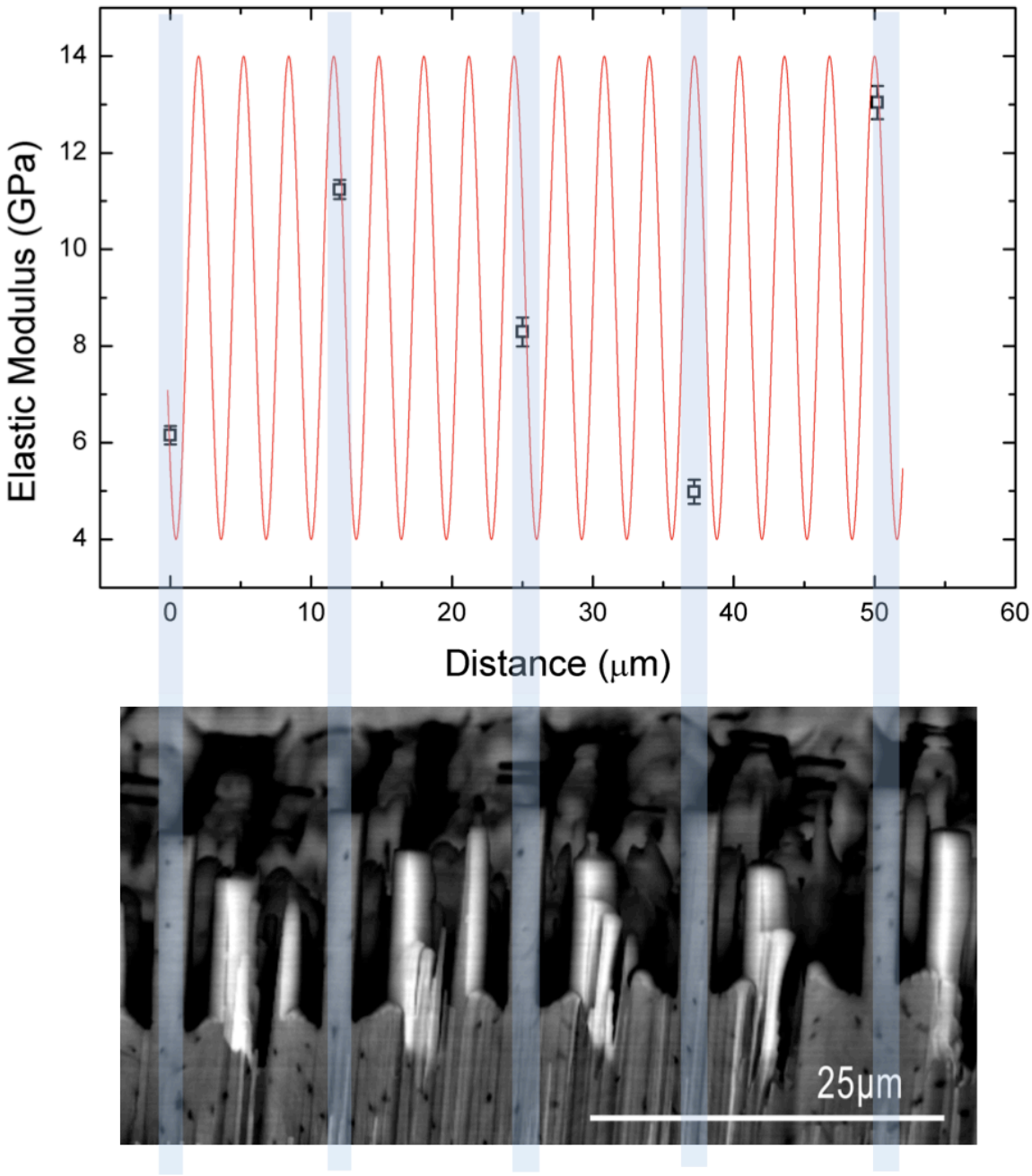

Figure 5.6 Plot of the variation in elastic modulus against beam position at the edge of the bone sample shown in the SEM micrograph. The expected structural periodicity arising from the mineralized collagen fibril layer orientations is fitted to the plot as shown by the sine curve.

The red line sine curve fitting was plotted with a periodicity similar to that of the repeating lamellar unit in rat long bones as measured by Weiner et al. (Liu, Weiner & Wagner 1999) and is similar to the fit by Gupta et al. (Gupta, Stachewicz & Wagermaier 2006). The curve fitting to the points on a sine curve was achieved using $y=y_0+A\sin(2\pi(x-x_c)/w)$ where $y_0=8.38\pm0.87$, $A=3.52\pm1.04$, $x_c=6.90\pm1.54$ and $w=18.49\pm1.15$. This fit was then adjusted to the 3.2 μm periodicity of the lamellar unit of rat long bones, and simulated onto the plot with the following values $y_0=9$, $A= 5$, $x_c=7.6$ and $w=3.2$. Though only 5 points are plotted over a length of 50 μm, the sine curve with the appropriate periodicity fits the lamellar unit periodicity as observed in previous research by Weiner et al. (Weiner et al. 1997) as shown in Figure 5.6. It is noted that one of the points in Figure 5.6, at a distance of 37 μm, fits poorly to the sine curve. Potential reasons for this poor fit are due to the cantilever beam showing a slight off axis alignment or poor local mineralization, which would provide a low elastic modulus calculated from bending relate to the predicted high elastic modulus.

The measured changes in the elastic modulus of the bone micro-beams are expected to be due to the collagen fibril orientations within the beam. In particular, a micro-beam consisting predominantly of collagen aligned mainly along the long axis of the micro-beam will give a large elastic modulus whereas a micro-beam composed mainly of collagen oriented perpendicular to the long axis of bone will give a low elastic modulus value. To validate this assumption, SEM back-scattered imaging was used to examine the FIB

polished surfaces of the micro-beams as shown in Figure 5.3. Back-scattered imaging provides atomic number contrast at relatively flat samples. Thus, orientation in mineralized collagen fibrils can be quantified using back-scattered imaging due to the orientation of the relatively high atomic number mineral phase along the collagen fibril length. Figure 5.7 shows an individual bone micro-beam with a series of linear patterns observed from the base of the beam to the end of the beam. Linear patterns in bone material in this work show similarities to fibrillar patterns observed in transmission electron micrographs (TEM) collected by Weiner et al. from demineralised lamellar rat femur and tibia samples (Weiner et al. 1997; Weiner, Traub & Wagner 1999). The linear patterns observed in back-scattered SEM are expected to correspond to the mineral in the oriented collagen fibrils and are seen to change from the micro-beam base to free end in Figure 5.7. An overall fibril orientation in the micro-beam is potentially difficult to define and is not expected as a range of subunits with differing orientations are present in the micro-beam. However, an average mineralized fibril orientation in the micro-beams can be defined by measuring the linear pattern angle in the micro-beam at 10 equidistant points along the length of the micro-beam as shown in Figure 5.7. A total of 4 beams, labelled as beams 2, 4, 5 and 6 in Figure 5.3, were examined with the fibril orientation angle relative to the length of the micro-beam along the length of each beam shown in Table 5.1.

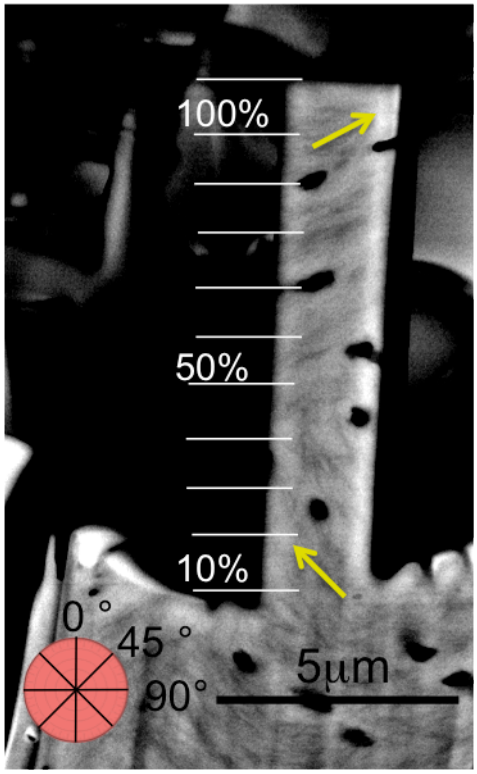

Figure 5.7 SEM micrograph of an individual FIB polished bone micro-beam with markers indicating the percentage distance along the beam where the fibril orientation angle was measured.

Table 5.1 – Comparison of the elastic modulus of the FIB milled bone micro-beams with the fibril angle in degrees of the orientation along the length of the micro-beam, as indicated by the percentage of the total micro-beam length from the base.

	Beam 2	**Beam 3***	**Beam 4**	**Beam 5**	**Beam 6**
Modulus (GPa)	13.04±0.34	4.98±0.25	8.29±0.30	11.24±0.20	6.15±0.19
Percentage from base					
10%	27°	N/A	41°	32°	66°
20%	43°		54°	40°	90°
30%	30°		47°	42°	63°
40%	56°		36°	34°	71°
50%	57°		25°	49°	61°
60%	53°		35°	38°	65°
70%	62°		33°	40°	75°
80%	57°		47°	27°	90°
90%	N/A		44°	37°	76°
100%	N/A		N/A	N/A	N/A
Total average orientation	48°		40°	38°	73°

*Beam 3 was not sufficiently polished and did not show any features in BSED SEM.

Finite element analysis (Abaqus FEA, Dassault Systemes, Fra.) of an individual bone micro-beam under bending was carried out in order to determine which orientation along the micro-beam length contributed significantly to the overall beam bending behaviour.

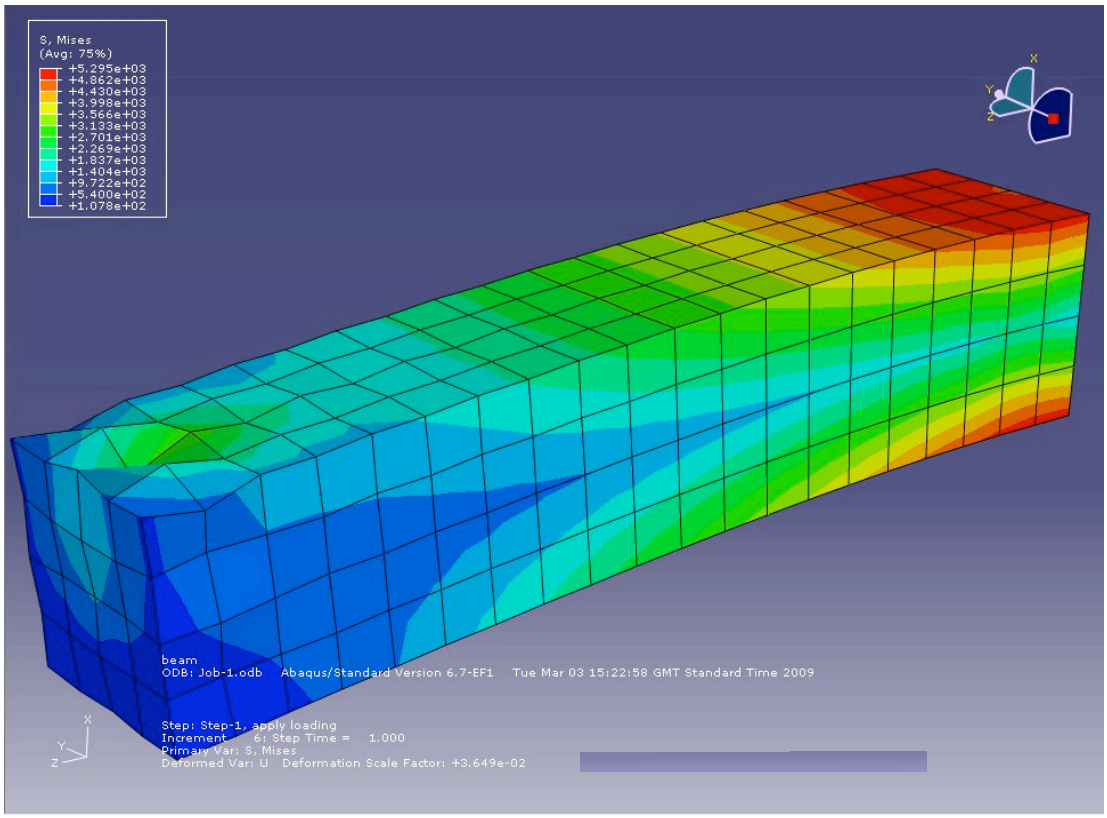

Figure 5.8 FEA modelling of a cantilever in bending with a concentrated load applied to the free end at the left of the model. The red corresponds to higher stresses while the blue corresponds to the lowest stresses.

The FEA experiment shown in Figure 5.8 highlights that the stresses are mainly concentrated in the first 10% of the length of the beam, which indicates that the collagen fibril orientation within this first 10% of the beam length defines bone micro-beam mechanics during bending tests.

The apparent fibril/platelet orientation observed via the backscattered SEM images as shown in Table 5.1 can be related to the elastic modulus of the bone micro-beams measured by AFM methods as shown in Figure 5.6. The elastic modulus of the bone micro-beams is observed to increase as the orientation angle decreases. Thus, collagen fibrils and platelets oriented

along the long axis of the micro-beam (i.e. the 0° angle) provide an increased elastic modulus whereas progressive off-axis alignment gives a drop in the micro-beam elastic modulus. In addition, the observation of orientation at FIB polished micro-beam surfaces using SEM back-scattered imaging appears to be a robust method for characterizing structural orientation and resultant bone micro-beam mechanics. The micro-beam elastic modulus variation with orientation can be described using a theoretical model created by a combination of the slab model and rule of mixtures along with the Halpin-Tsai model as achieved previously by Akiva et al. (Akiva, Wagner & Weiner 1998). Using the structural parameters given by Akiva et al. (Akiva, Wagner & Weiner 1998), the theoretical elastic modulus of a lamellar unit when all collagen fibrils are aligned along the long axis of bone and when the collagen fibrils are aligned perpendicular to the long axis are calculated using Equations 34 and 35 respectively.

$$E_1 = E_m\left(1 - V_p\right) + E_p V_p$$ Eqn. 34 (Akiva, Wagner & Weiner 1998; Hull & Clyne 2001)

$$E_2 = E_3 = \left[\frac{V_p}{E_p} + \frac{\left(1 - V_p\right)}{E_m}\right]^{-1}$$ Eqn. 35 (Akiva, Wagner & Weiner 1998; Hull & Clyne 2001)

Where E_1 is the theoretical elastic modulus of a lamellar unit with all of the platelet reinforced collagen fibres aligned along the long axis of the bone, E_2 is the elastic modulus when these fibres are all aligned transverse and

perpendicular to the long axis of the bone and E_3 is the elastic modulus when the fibres are aligned transversely out-of-plane as shown in Figure 5.4. V_p is the platelet volume fraction taken as 0.5 (Doty, Robinson & Schofield 1976; Ziv, Wagner & Weiner 1996; Akiva, Wagner & Weiner 1998), E_m is the elastic modulus of collagen taken as 2.4±0.4 GPa (Hang & Barber 2011) and E_p the elastic modulus of the mineral platelets taken as 114 GPa (Gilmore & Katz 1982; Akiva, Wagner & Weiner 1998). The values calculated by inputting the previous values into Equations 34 and 35 give E_1= 58.2 GPa, E_2 =E_3=4.7 GPa. Following the modelling of Akiva et al., the elastic modulus values E_1, E_2 *and* E_3 were then inputted into the following equation:

$$E(\theta,\varphi)=\frac{\cos^4\theta}{E_1}+\frac{\sin^4\theta\cos^4\varphi}{E_2}+\frac{\sin^4\theta\sin^4\varphi}{E_3}+\cos^2\theta\sin^2\theta\cos^2\varphi I_{12} \\ +\sin^4\theta\sin^2\varphi\cos^2\varphi I_{23}+\sin^2\theta\cos^2\theta\sin^2\varphi I_{31} \qquad \text{Eqn. 36}$$

Where

$$I_{ij}=\frac{1}{G_{ij}}-2\frac{v_{ij}}{E_{ij}}(i,j=1,2,3,i\neq j) \qquad \text{Eqn. 37}$$

and E is the overall elastic modulus of the lamellar unit including all the collagen fibril orientations, θ is the collagen fibril orientation angle and varies from 0°≤ θ≤90°, φ is the angle of mechanical testing and varies from 0°≤ φ ≤90°, G is the shear approximated by G=E/2(1+ν) where ν is the Poisson's ratio with a value of 0.35 as set by Akiva et al. (Akiva, Wagner & Weiner 1998) and *ij* is the testing axis.

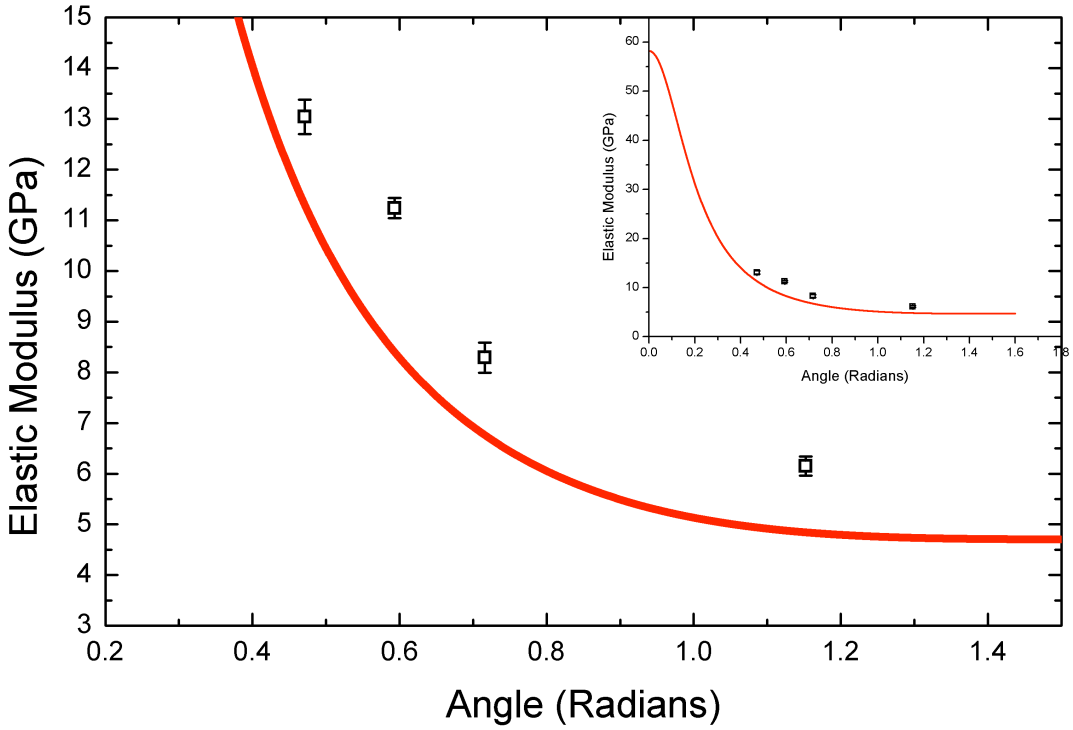

Figure 5.9 Plot of the variation in elastic modulus with predominant collagen fibril orientation measured within the first 10% of each beam length. The red line is the Halpin-Tsai fit of Equation 36 using the theoretical values for the geometrical and mechanical components of bone.

Equation 36 is plotted in Figure 5.9 and shows a good fit with the variation of the elastic modulus of the bone micro-beams with orientation. The experimental results are consistently slightly higher than the curve plotted from Equation 36 and is probably due to an underestimation of the elastic properties of the components used in the curve plot. However, our results show that the variation in the elastic modulus of the micro-beams are consistent with structural models of bone and highlight how the elastic

modulus can be predicted from orientation observations and solving Equation 36.

5.4. Conclusion

Bone micro-beams with dimensions comparable to the lamellar unit were successfully isolated using focussed ion beam (FIB) microscopy and mechanically tested in bending using atomic force microscopy (AFM). A variation in the mechanical properties of the micro-beams was observed and directly related to the mineralised collagen fibril orientation inferred from back-scattered scanning electron microscopy (SEM) imaging. Mechanical models already established by Akiva et al. (1998) were applied to describe the relationship between collagen fibril orientation and mechanical behaviour of the lamellar unit. The results in this chapter highlight the ability to measure discrete bone volumes directly in bending and correlate the mechanical performance of bone with the structural orientation of the mineralised collagen fibrils.

Chapter 6. Effect of orientation in bone lamellae on strength and toughness of bone

6.1 Introduction

Bone is a fibrous biological nanocomposite material, which is optimized to avoid catastrophic failure (Peterlik et al. 2006; Fratzl & Weinkamer 2007). The fracture behaviour of bone is expected to be controlled by the various structural features present across the many existing hierarchical length scales (Gupta & Zioupos 2008). However, micron sized lamellae in bone present the simplest composite unit in bone consisting of mineralized collagen fibrils within a protein matrix, with some work suggesting that this length scale dominates the fracture of whole bone (Peterlik et al. 2006). In this chapter we examine the mechanical properties of individual lamellae, extending the work of the previous chapter, to failure using in-situ atomic force microscopy (AFM)-scanning electron microscopy (SEM) techniques (Hang & Barber 2011). Individual lamellar beams are isolated from bone using focussed ion beam (FIB) microscopy and mechanically deformed with the AFM while observing failure modes using SEM. Both the elastic and fracture behaviour of the bone lamellae are determined using these techniques. Composite analysis is used to evaluate the mechanical behaviour of lamellae and results at micron and sub-micron length scales related to the

overall toughness of bone material. Thus, the contribution of micron and sub-micron toughening mechanisms to the fracture of whole bone is considered.

Bone has different structural features across different lengths scales in order to avoid catastrophic failure. These structural features allow bone to distribute stresses as well as deflect cracks (Koester, Ager & Ritchie 2008). At the macro scale, long bones are tubular distribute loads away from the centre of mass hence allowing bone to carry the load more effectively. At the tissue level bone is organized into layers of bone material in either consecutive, parallel layers or concentric rings. The layers in turn consist of fibres orientated in five distinct orientations (Weiner, Traub & Wagner 1999). These layers allow the bone to deflect cracks allowing it to absorb more energy therefore preventing fast catastrophic failure.

While the elastic properties of bone have been examined in detail as explained in this thesis, a number of works have attempted to measure the fracture properties of bone at different length scales (Bonfield & Datta 1976; Currey 1979; Reilly & Currey 1999; Gupta & Zioupos 2008; Koester, Ager & Ritchie 2008). These studies have identified numerous factors that determine the resultant failure strength and toughness of bone and includes collagen fibril orientation, mechanical testing strain rate and testing temperature as highlighted by Evans, 1973 (Evans 1973; Behiri & Bonfield 1984). Whole bone fracture mechanics have been studied extensively using both notched specimens (Bonfield & Li 1966; Bonfield & Datta 1976; Behiri & Bonfield 1984) and unnotched specimens performed by Evans, 1973 (Evans

1973; Bonfield & Datta 1976). Bonfield and Li first studied the fracture mechanics of bovine long bones such as the femur and tibia. Impact tests conducted in both the bone longitudinal and transverse orientations showed that bone fracture mechanics are directly related to surface cracks, which reduce the energy absorbed during fracture (Bonfield & Li 1966; Bonfield & Datta 1976). The relationship between the surface cracks and fracture stress was a topic studied extensively in order to uncover bone fracture toughness in various forms such as critical strain energy rate (G_c) and the critical stress intensity factor (K_c) (Bonfield & Datta 1976; Behiri & Bonfield 1984). The geometry of the specimen produced fast crack propagation with variable and uncontrollable velocity. Compact tension tests were implemented by Bonfield and Behiri in numerous studies (Bonfield, Grynpas & Young 1978; Behiri & Bonfield 1984) in order to test the fracture mechanics of bone. This testing method allowed the control of the rate of crack propagation permitting the precise measurement of G_c and K_c values for transversely oriented bovine femur and tibia to be made. Further exploitation of compact tension testing was also used to study the effect of bone densities on its fracture properties (Behiri & Bonfield 1984).

At the architectural level, with specimens of dimension of 30x5x4 mm, Currey later analysed the properties of three different types of bones: antler, cow femur and fin whales tympanic bulla in order to determine the correlation between the resultant mechanical properties and the different functions of each bone specimen. To achieve this aim, notched specimens were loaded in three-point bending and the work-to-fracture was calculated.

Resultant work-to-fracture values were shown to be particularly useful in determining if the bone material function was for toughness as the work-to-fracture measures the amount of work necessary to drive a crack through a material and provides quantification of the resistance of bone, and indeed other materials, to catastrophic failure (Currey 1979). Liu et al. performed cantilever bending tests of considerably smaller test specimens of dimensions of 1.3x0.6x0.16 mm of baboon tibia in order to determine the elastic modulus and the work-to-fracture of the test specimens in both longitudinal and transverse while observing differences in their evolved fracture surfaces (Liu, Weiner & Wagner 1999). Liu determined that the collagen fibril orientation is critical in determining the elastic modulus and work-to-fracture. Specifically, the work-to-fracture increases and elastic modulus increases as the collagen fibrils were aligned along the principal axis of the cantilever beam tested. These results obtained from unnotched cantilever bending tests show the same trend as from three-point bending testing performed on much larger sample sizes (1x1x15 mm) (Liu, Wagner & Weiner 2000) although the absolute values are lower for the smaller unnotched cantilever bending tests (Liu, Weiner & Wagner 1999). Liu et al. attributes this decrease in work-to-fracture to possible micro-cracks introduced during the sample preparation or to the difference in specimen size as little is known on the relationship of specimen size and work-to-fracture of bone. Since the samples for these cantilever bending tests were unnotched, the intrinsic work-to-fracture of the material cannot be determined as little is known of the pre-existing flaws in the material. Adding

a notch to the sample allows for a controlled flaw to be introduced and monitored. However, cantilever bending allows the mechanical properties of bone material to be tested by manufacturing the beams with their principal axes along the direction of interest (Liu, Weiner & Wagner 1999) to provide a full evaluation of the effect of structural orientation on bone fracture properties.

More recently Ritchie et al. 2008 concluded that the most suitable fracture mechanics technique for assessing whole bone mechanical behaviour in small animal studies is the application of linear-elastic fracture mechanics techniques to determine the plane-stress K_c value (Ritchie et al. 2008) (Koester, Ager & Ritchie 2008). However, Yang et al. concluded that linear-elastic fracture mechanics is only accurate and consistent if the specimen and crack length both exceed the process-zone length, which is not met in transverse fracture and does not therefore accurately describe the whole fracture process in cortical bone (Yang et al. 2006).

Difficulties in considering a suitable method to describe the fracture of bone arise from the complexity of the bone failure process. In particular, a number of failure mechanisms operate in bone, the most significant being plasticity of the collagen phase, crack deflection along cement lines, diffuse micro-cracking and the bridging of cracks by ductile phases (Yang et al. 2006). Results by Yang el al. showed that bone toughness is defined both by the mineral phase and, critically, the organization and deformation behaviour of the collagen and non-collagenous protein phases (Yang et al. 2006). Peterlik

et al. supported the work of Yang by controlling crack extension in osteonal lamellar bone with dimensions of 15x1.5x2 mm. Peterlik explained that the fracture process is dependent on the direction of the crack propagating through the bone, with brittle failure behaviour (or low toughness) occurring when cracks propagate along the longitudinal direction in bone whereas significant toughness is obtained when cracks propagate in the transverse or tangential direction of bone. The principal mechanism for enhancing toughness was determined to be due to significant micro-cracking events occurring especially when the collagen fibril orientation was perpendicular to the initial crack (Peterlik et al. 2006; Gupta & Zioupos 2008). Peterlik concluded that micron sized lamellae in bone present the simplest composite unit in bone consisting of mineralized collagen fibrils within a protein matrix and that the collagen orientation gives bone its more ductile fracture behaviour, suggesting that this length scale dominates the fracture of whole bone (Peterlik et al. 2006).

The importance of understanding the small length scale behaviour of bone and its influence on enhancing toughness has promoted the use of mechanical testing able to record corresponding deformation and failure behaviour. Although nanoindentation has been effective in determining the variation of lamellae elastic modulus with testing direction (Rho, Tsui & Pharr 1997; Rho et al. 2001; Gupta, Stachewicz & Wagermaier 2006), testing of individual lamellae and sublamellae to fracture is required to determine the absolute contribution of the lamellar unit to overall bone toughness. This chapter therefore evaluates bone failure at the sub-lamellar level in two

different testing methods using buckling and cantilever bending. The selection of buckling and bending represents more closely the physiological loading present within bone (Currey 2002), certainly when compared to the effective puncture testing performed by indentation techniques.

6.2 Materials and methods

Rat femora were used as a source of bone material. Sub-lamellar bone micro-beams from these rat femurs were isolated using a dual beam system. The dual beam system is composed of a scanning electron microscope (SEM) and focused ion beam (FIB) working simultaneously. The FIB allows bone material to be milled out in order to pattern fine cantilever beams of bone for subsequent mechanical testing (Jimenez-Palomar et al. 2012).

Bone micro-beams were extracted from the femurs of 8-month-old sprague dawley rats as described in previous chapters and shown in Figure 6.1. These micro-beams were patterned to suit each type of loading condition. Micro-beams tested in buckling were made slender with dimensions of around 14x1.7x2 μm. Bone beams tested in cantilever bending were patterned, as in the previous chapters, to produce dimensions of 10x2x2 μm. These dimensions ensured that the shear stress contribution to the bending stress was minimal (<~3.5%) (Jimenez-Palomar et al. 2012). All cross-sectional area measurements were taken from top and front SEM images of each of the beams.

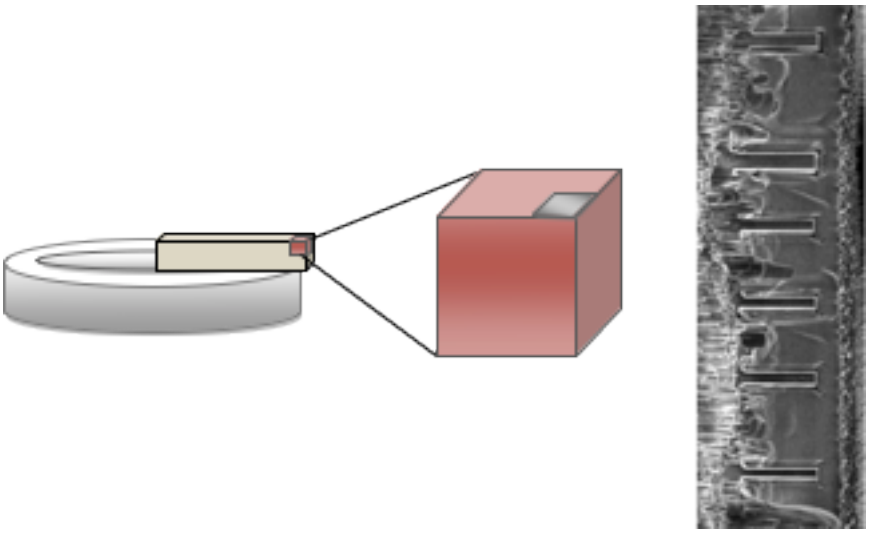

Figure 6.1 Sample setup for buckling experiments; the left shows a schematic of the sliced rat femur with a length of ~10 mm and, on the right, an SEM image of the bone micro-beams each having a length of ~10 μm.

Mechanical testing of the bone micro-beams was performed using a custom built atomic force microscope (AFM) (Attocube GmbH, Ger.) incorporated within the vacuum chamber of an SEM. The setup allows in situ mechanical testing of micro-beams (Hang & Barber 2011) while observing using SEM. High spring constant AFM cantilevers (Veeco, USA) used for testing in buckling had a measured spring constant of 155 and 158 Nm^{-1} respectively. AFM cantilevers (AppNano, USA) used for micro-beam bending tests in this chapter had a spring constant of 28 Nm^{-1}.

6.3 Results

6.3.1 Bending to failure

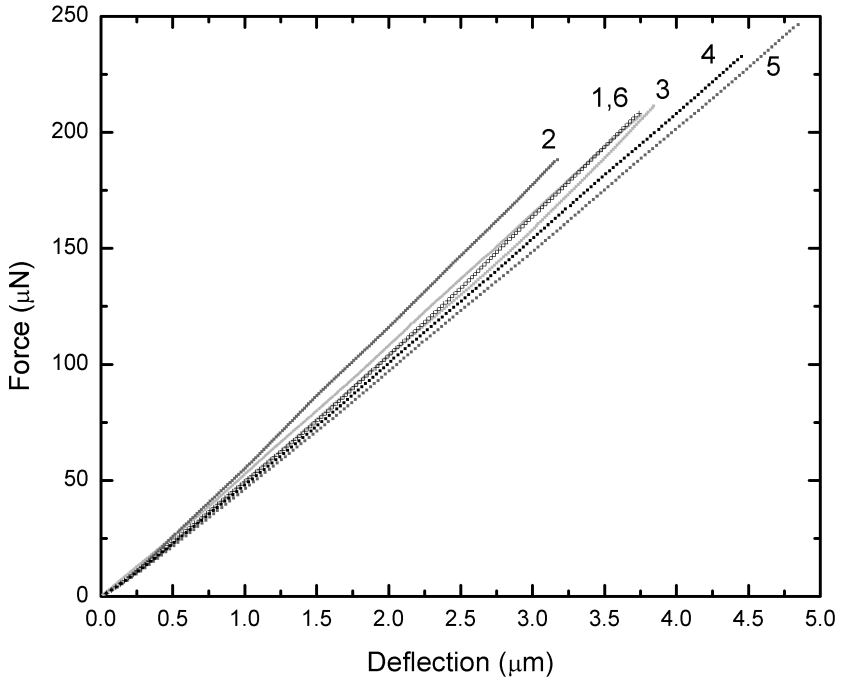

Figure 6.2 AFM force-deflection curves for 6 sub-lamellar micro-beams tested to fracture in bending. The labelling corresponds to the test numbers in Table 6.1.

The first experiments were performed in cantilever bending to failure. The force-displacement curves for six beams tested to failure are shown in Figure 6.2 and the SEM screenshots of in situ testing of rat femur bone micro-beam in bending to failure are shown in Figure 6.3. There are slight variations in the amount of force that was needed to fracture each beam. These slight variations could be attributed to changes in collagen orientation within the bone micro-beams (Peterlik et al. 2006). Table 6.1 details the different elastic modulus and work-to-fracture values calculated for each beam.

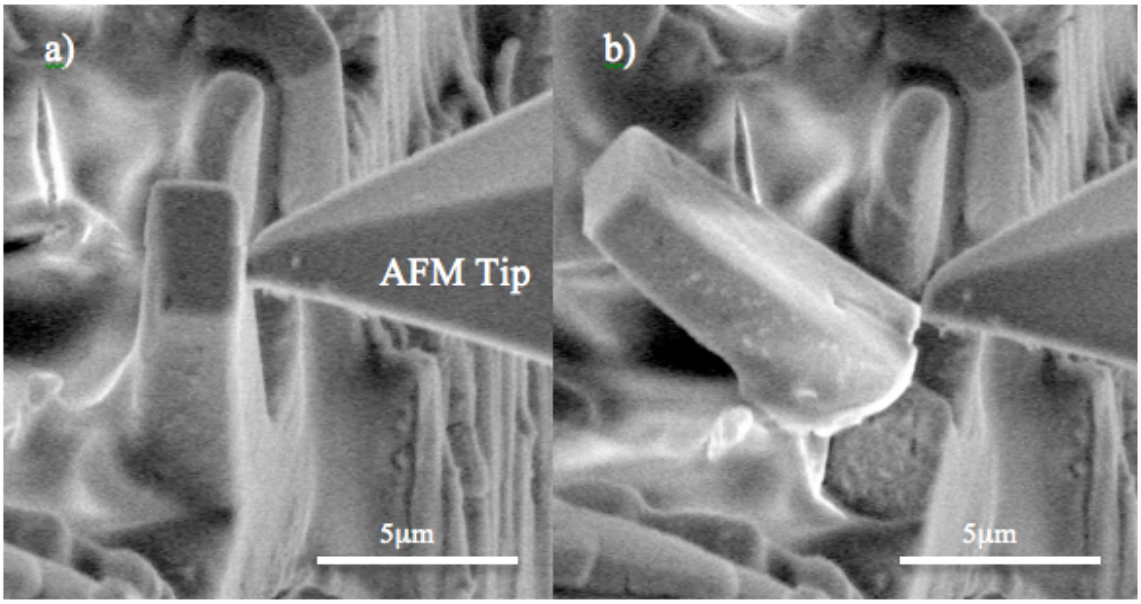

Figure 6.3 SEM micrographs showing a) in-situ cantilever beam testing in bending provided by the AFM tip pushing into the free end of the bone micro-beam until b) failure of the micro-beam occurs. Images were taken with a 25° sample tilt relative to the incident SEM beam.

The elastic modulus and the work-to-fracture for the micro-beams tested to failure shown in Table 6.1 were calculated using a variation of the equation described by Liu et al. (Liu, Weiner & Wagner 1999) adjusted for rectangular cross-sectioned samples used across this thesis as opposed to the circular cross-sectioned samples Liu et al. tested. Specifically, the nominal work-to-fracture was calculated from the area under the force-deflection curve, divided by twice the cross-sectional area of the specimen (Liu, Weiner & Wagner 1999; Koester, Ager & Ritchie 2008). The elastic modulus, the strength and the work-to-fracture of each of the testing methods were calculated from the force deflection curves using the formulas below.

$$E = \frac{12l^3}{3bh^3} \cdot \frac{f}{\delta} \qquad \text{Eqn. 24}$$

$$\sigma_{max} = \frac{6fl}{bh^2} \qquad \text{Eqn. 38}$$

$$W = \frac{2A}{bh} \qquad \text{Eqn. 39}$$

Where *l, b* and *h* are the length from the base of the sample to testing contact point, breadth and height of the rat bone beam respectively and f/δ is the slope of the force-displacement curve as detailed in Chapter 4. σ_{max} is the maximum stress calculated from Equations 25-27 in Chapter 4. *W* is the work-to-fracture and *A* is the area under the force-displacement curve. Table 6.1 shows the elastic modulus, strength and work-to-fracture, calculated using Equation 24, 38 and 39 respectively, for the bone micro-bends mechanically tested in bending to failure using the experiment as displayed in force-distance curves in Figure 6.2.

Table 6.1 Work-to-fracture and elastic modulus values of rat bone femur micro-beams tested in bending to failure. Sample test no. is order in order to provide work-to-fracture values arranged from lowest to highest.

Beam No.	**Test No.**	**Work-to-fracture (Jm^{-2})**	**Strength (MPa)**	**Elastic Modulus (GPa)**
4	2	99.31	846.82	8.12±1.62
3	1	108.80	632.15	3.78±0.76
8	6	124.71	952.07	6.03±1.26
5	3	141.70	1082.8	9.4±1.88
6	4	146.61	796.48	4.8±0.96
7	5	162.25	749.63	3.68±0.74

Generally, except in the case of test number 1 and 3, the elastic modulus on the bone micro-beams increase as the corresponding work-to-fracture decreases as shown in Figure 6.4. The error bars in Figure 6.4 are calculated to be 20% and arise from uncertainties in defining the contact point between the AFM tip performing the bending test and the free end of the bone micro-beam as detailed in Chapter 4. Exceptions to the increase in micro-beam elastic modulus with decreasing work-to-fracture are found for Beam 3 and Beam 5. Interestingly, both these beams appear to possess a large flaw in the form of canaliculi at the base of the micro-beam as seen by SEM-BSED in Figure 5.2 and Figure 5.6.

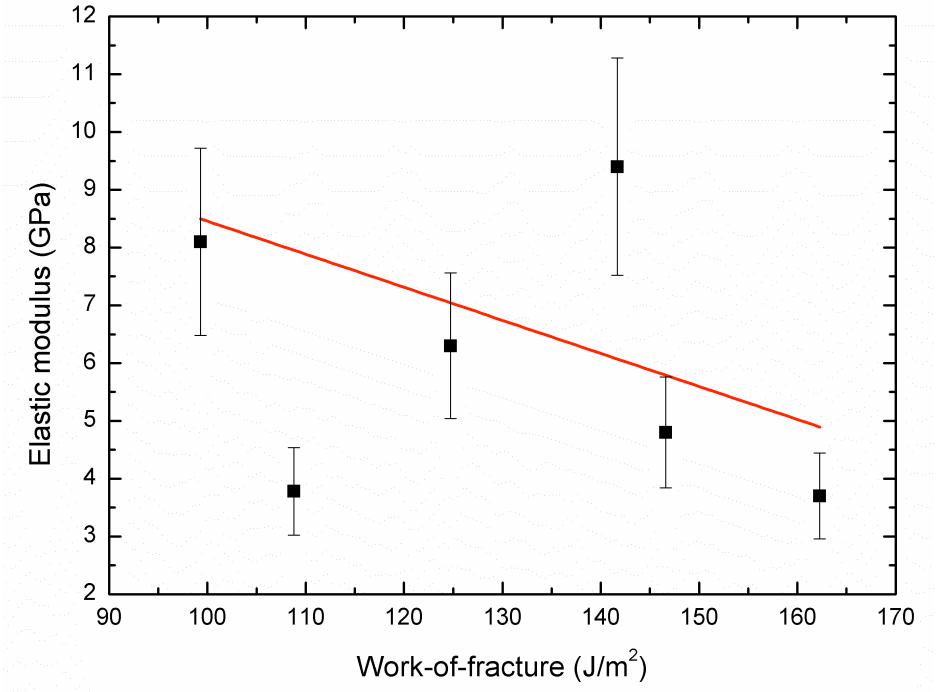

Figure 6.4 Plot of the elastic modulus of bone micro-beams against their corresponding work-to-fracture, with data taken from Table 6.1. The trend line highlights an increase in the bone micro-beam elastic modulus as the work-to-fracture of the beam decreases.

6.3.2 Buckling to failure

The second mechanical test performed on FIB fabricated bone micro-beams was a buckling test. The geometry of the beam used for a buckling test is critical as high aspect ratio beams compressed along their principal axis tend to collapse before reaching the compressive or tensile strength of bone (Currey 2002). Taking into consideration the values for the compression strength of rat bone, a micro-beam critical slenderness length/width ratio, was calculated in order to determine the appropriate dimensions for the micro-beam in order to test in buckling. The mechanical property values of rat bone were taken from Cory et al. 2010 where the compression strength (σ_{UCS}) for whole rat femora in compression is 140 MPa and the elastic modulus is 8.8 GPa (Cory et al. 2010). Using Equation 40 and the relationship of $P_{cr}=\sigma_{UCS}.A$, a slenderness ratio of ~7 is obtained. Therefore, suitable bone micro-beams were fabricated using FIB as described in Chapter 3 to ensure buckling failure under compressive loading.

Mechanical loading was carried out using the custom built AFM setup as shown in Figure 6.5 below where the AFM tip is parallel to the long axis of the micro-beam tested. This setup is subtly different to the standard AFM configuration defined in Chapter 3 due to the requirement of applying a compressive load to the bone micro-beam while allowing SEM imaging of the sample from above.

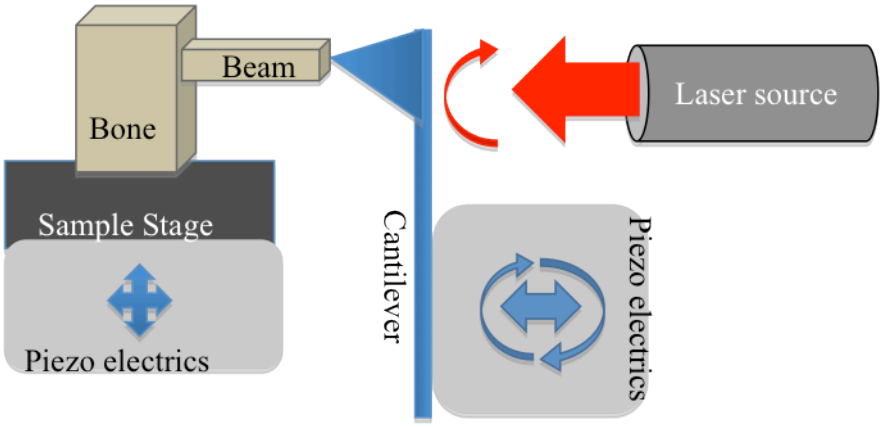

Figure 6.5 Schematic diagram showing the orientation of the bone micro-beam relative to the custom built AFM setup inside SEM. This setup enables the application of compressive forces to the bone micro-beam.

In-situ mechanical testing of individual bone micro-beams compressed along their principal axis using AFM is shown in Figure 6.6 below. The SEM micrographs in Figure 6.6 indicate a progressive compression of the bone micro-beam, with progressive off-axis deformation of the micro-beam occurring as the force applied to the sample by the AFM tip increases.

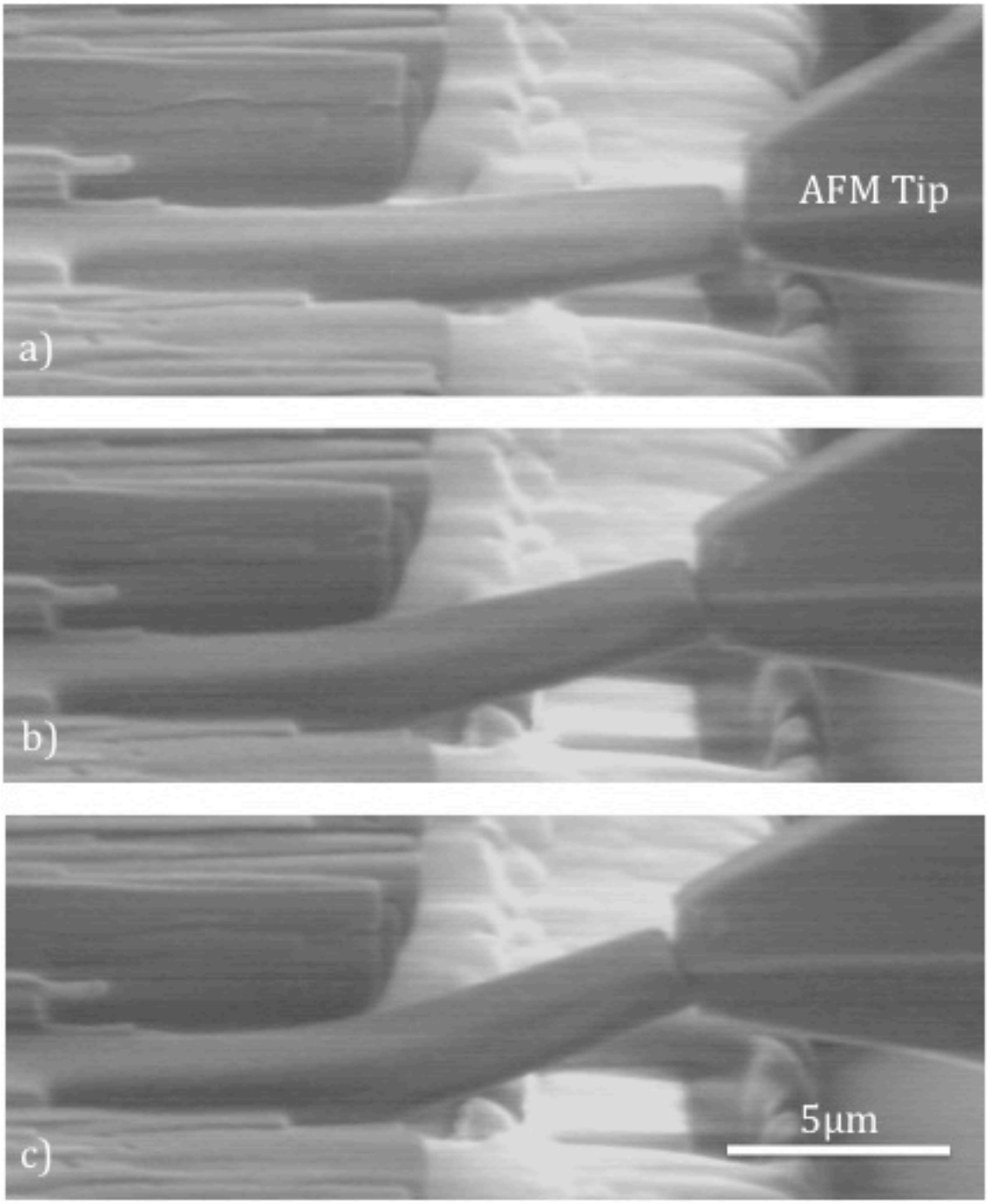

Figure 6.6 SEM micrographs at a 52° angle showing progressive deformation of an individual bone micro-beam in compression with snapshots of SEM video showing one of the six bone micro-beams tested to failure in buckling; a) the micro-beam unloaded b) loading of the micro-beam with some off-axis deformation and c) considerable micro-beam buckling prior to failure. The AFM tip and micro-beam are indeed aligned, as can be noted from the side edge of the micro-beam which aligns to the side edge of the AFM tip.

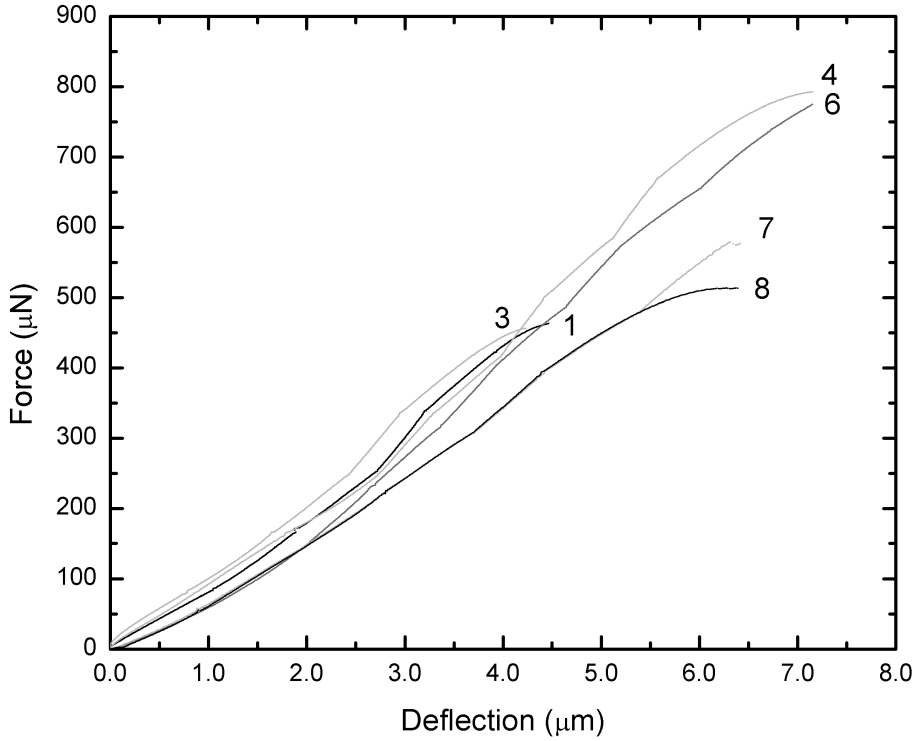

Figure 6.7 AFM force-deflection curves of the 6 sub-lamellar micro-beams tested to fracture in buckling. The labelling corresponds to the test number.

The resultant force-distance curves obtained when buckling the micro-beams tested using a compressive loading from the AFM is shown in Figure 6.7 above. The force is initially observed to show an almost linear increase with sample deflection but becomes non-linear at larger deflections.

Figure 6.7 above is important for quantifying the mechanical behaviour of the bone micro-beams. The work-to-fracture is directly calculated from Figure 6.7 by measuring the area under each of the force-distance curves, whereas the elastic modulus was calculated from the maximum force applied to each micro-beam using Equation 40.

As can be seen in Figure 6.6, the bone micro-beams were buckled in "fixed-pinned" mode. The relationship between the loading and resultant micro-beam elastic modulus is given below in Equation 40 to describe the deformation schematic in Figure 6.8.

$$P_{cr} = \frac{\pi^2 EI}{L_e^{\,2}} \qquad \text{Eqn. 40}$$

Where P_{cr} is the critical load, E is the elastic modulus of the material, I is the minimum moment of inertia, $I_{min}=(1/12)*bt^3$ where b is the breadth and t is the thickness; L_e is the effective length of the column. In this case, since the support method is fixed-pinned, $L_e=0.7*L$ where L is the total length of the cantilever beam tested.

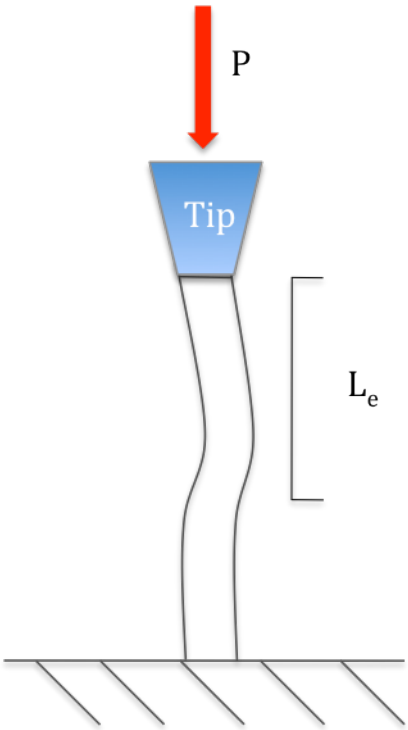

Figure 6.8 Schematic showing the geometry and orientation of the bone micro-beam undergoing loading by the AFM tip. This loading conditions can be described as fixed-pinned, which corresponds to the loading observed in SEM micrographs shown in Figure 6.6.

The elastic modulus and work-to-fracture of the bone micro-beams tested via the AFM tip inducing sample buckling is shown in Table 6.2 below. The results in Table 6.2 show an increase in the work-to-fracture corresponds to increases in both the buckling strength the elastic modulus of bone micro-beams. This trend differs from the previous micro-beams bending results where an increase in the micro-beam work-to-fracture was associated with a decrease in the sample's elastic modulus.

Table 6.2 Work-to-fracture and elastic modulus values of rat bone femur micro-beams tested in buckling to failure. Work-to-fracture values are arranged from lowest to highest.

Test No.	Work-to-fracture (Jm^{-2})	Strength (MPa)	Elastic Modulus (GPa)
3	481	113	3.15
7	729	120	2.95
1	770	180	8.62
4	941	133	2.42
8	1640	247	13.3
6	2560	384	22.4

6.4 Discussion

Differences in mechanical properties between individual bone micro-beams recorded using both buckling and bending tests are expected to be directly correlated with collagen fibril orientation as explained in Chapter 5, especially as there are no other bone features such as lamellar boundaries and cement lines that could affect the fracture properties of these bone samples. However, clear discrepancies exist between the two testing methods employed especially as bending indicates a decrease in elastic modulus of the micro-beams with increasing work-to-fracture whereas buckling indicates an increasing elastic modulus with increasing work-to-fracture. Examination of the force-distance curves for both micro-beam bending and buckling in Figures 6.2 and 6.7 reveal important differences in the deformation behaviour of the samples. Specifically, micro-beams tested in buckling compression exhibit a non-linear region in their force-distance behaviour which the bending test curves lack. This non-linear behaviour may be explained by either progressive off-axis loading that causes a decrease in

the force build-up with sample deflection or inherent material plasticity. The possible explanation of inherent plasticity of the bone micro-beam is expected to be due to the deformation of the mineralized collagen fibrils. In buckling, the mineralized collagen fibrils are compressed and the load is therefore carried mainly by the mineral platelets. However, large applied deformations may cause a plastic deformation of the mineralized collagen fibrils, which will result in the observed non-linear force-distance behaviour. Clear plastic deformation in cantilever bending tests is not observed and is potentially due a fraction of mineralized collagen fibrils carrying more load than other fibrils, such as if fibrils at the top micro-beam surface strain more than fibrils at the bottom micro-beam surface. Thus, failure of the fibrils carrying more load will cause a load redistribution across a smaller fraction of fibrils. These fibrils can fail rapidly due to the load redistribution to that the overall failure of the bone micro-beam resembles a fast fracture.

As discussed earlier in this chapter the fracture mechanical properties are affected by the mechanical testing strain rate, the collagen fibril orientation, the temperature and the amount of defects, in the case of bone such defects could be in the form of microcracks or canaliculi (Evans 1973; Behiri & Bonfield 1984) (Bonfield & Li 1966; Bonfield & Datta 1976). For the purpose of this study, both the rate of testing, the temperature, the environmental condition and the volume were kept constant while the effect of the collagen orientation was considered. Non-the less when comparing the mechanical properties measured in this work to previous work such as mechanical testing performed on larger samples there is a volume effect that has to be

taken into consideration. The amount of defects present in a material decrease with decreasing volume tested. Therefore it was expected to see an increase in the mechanical properties of bone when small volumes of bone such as the ones in this work were tested. This however was not the case; this work shows that the mechanical properties of bone remained the same irrespective of a volume effect. This could be explained by what Peterlik et al. (2006) concluded in his paper as explained previously, that the micron sized lamellae in bone presents the simplest composite unit in bone and that along with the collagen orientation gives bone its more ductile fracture behaviour, suggesting that this length scale dominates the fracture of whole bone (Peterlik et al. 2006).

The different bending and buckling testing used is also reflected in the mechanical properties of the bone micro-beams. Importantly, the elastic modulus of the micro-beams in both bending and buckling are similar. The cantilever bending results have an average elastic modulus of 7.63±3.42 GPa while the buckling results have an elastic modulus of 8.81±7.9 GPa. The recorded elastic modulus is therefore an intrinsic material property for the bone material. Furthermore, the similarity between the elastic modulus of the bone micro-beams in buckling relative to bending indicates that off-axis loading during the buckling test is not prevalent; at least in the initial stages of the mechanical test, as significant off-axis loading in bucking would cause a drop in the recorded elastic modulus. Significant disparity is observed in the recorded micro-beam strengths with bending tests producing an average strength of 843.33±157.96 MPa whereas the buckling strength providing

196.17±104.72 MPa. This discrepancy is more difficult to explain but the different stress conditions acting on the micro-beams in bending and buckling testing would certainly provide different failure strengths. However, our results indicate that the mechanical properties of the bone material are better in bending than compression.

The greatest difference between bending and buckling testing modes is the divergence in work-to-failure vs. elastic moduli trends. The bending tests show a negative relationship, with work-to-fracture decreasing with increasing elastic modulus while the buckling tests show a positive trend with work-to-fracture increasing with elastic modulus. Absolute work-to-fracture values in buckling are considerably higher than in bending, which suggests that while bone material in compression has poor strength, the bone material is able to absorb significant amounts of energy prior to catastrophic failure. Indeed, the larger scale structural features of bone such as the hollow (and high moment of inertia) structures shown in Figure 1.1 could be incorporated to improve the buckling strength due to the inherently poor strength properties of the bone material. Bone micro-beam work-to-fracture values are impossible to compare to previous literature experimental results as it is critically dependent on specimen size and geometry (Koester, Ager & Ritchie 2008). However, the elastic modulus measured through these experiments are comparable to previous work (Liu, Weiner & Wagner 1999; Gupta, Stachewicz & Wagermaier 2006). The relationship between elastic modulus and work-to-fracture in the bone micro-beams can be described by consideration of the potential collagen

fibril orientation within the beams. Collagen fibrils oriented predominantly along the principal long axis of the beam will provide the highest elastic modulus due to the fibrils lying in the direction of the applied load. Conversely, collagen fibrils oriented away from this principle axis will provide less effective resistance to deformation, resulting in a lower elastic modulus, but failure will be able to occur predominantly at interfaces between the collagen fibrils. We therefore expect that the interfacial failure between the collagen fibrils is extensive during fracture of the micro-beams when the fibrils are not aligned in the direction of the bending and provide an enhanced work-to-fracture.

6.5 Conclusion

Unnotched bone micro-beams were mechanically tested in bending and buckling to failure. The work-to-fracture, strength and the elastic modulus in bending and buckling were calculated for individual micro-beams in order to assess the effect of collagen orientation on fracture properties of bone. The work-of-fracture and elastic modulus was calculated for each of the beams tested and exhibited an inverse correlation between the elastic modulus and work-of-fracture observed in tests performed in bending while the opposite is observed in tests performed in buckling.

Chapter 7. Effect of osteoporosis on the mechanical properties of bone at the sub-lamellar level

7.1 Introduction

While previous chapters have examined the environmental and structural effects on the mechanics of the lamellar unit, this chapter will extend these studies in order to examine the effect of disease on bone. Perhaps the most significant type of bone disease that causes degradation of bone's mechanical function is osteoporosis. Osteoporosis is characterized by significant changes in bone structure causing increases in bone fragility and therefore an increase in fracture risk (NIH-consensus-statement 2001). In recent years, due to the amount of people affected, osteoporosis has been vigorously investigated. In the United States alone, the costs of fractures resulting from osteoporosis have been estimated to be from 10 to 18 billion dollars per year and are expected to increase to 60 billion by the year 2020 (Iacono 2007). There are two distinct forms of osteoporosis; Type I which refers to the loss of trabecular bone mass after menopause due to lack of estrogen and Type II which refers to loss of cortical and trabecular bone in both men and women as a result of aging (Marcus & Bouxsein 2010). The disturbances in bone structure are due to changes in metabolic conditions such as hormonal changes (decrease in estrogen levels, growth hormone deficiency, increase in parathyroid hormone), steroids (glucocorticoid deficiency), diet and lifestyle (reduction in calcium intake, lack of vitamin D, sedentary life-styles) (Hauge,

Steiniche & Andreassen 2003; Iacono 2007). Both Type I and Type II osteoporosis share the common effect of increased susceptibility to catastrophic fracture in bone.

Bone fragility due to osteoporosis has been examined in terms of changes in bone structure and resultant influence on mechanical properties. The ability of bone to resist fast fracture depends on structural issues including bone mass, spatial distribution such as shape and micro-architecture, and the intrinsic properties of the bone material (Bouxsein 2001). Bone fragility is not determined by a single architectural feature and is the result of a combination of different architectural structures for a particular function such as to prevent catastrophic failure (Turner 2002). The ability of bone to prevent catastrophic failure is influenced by its strength (ultimate stress), stiffness (elastic modulus) and energy absorption quality (work-to-fracture) (Turner 2002).

At the macrostructural, architectural and microstructural levels, osteoporosis is typically diagnosed as a reduction of bone density. In cortical bone it is regarded as a reduction in bone mass and in trabecular bone as thinning and reduction in the number of trabecular struts across the body (Carter & Hayes 1976). The stiffness and strength of trabecular bone is typically related to bone density in a non-linear fashion with either a squared (Rice, Cowin & Bowman 1988) or a cubic (Carter & Hayes 1976) relationship, as the change in strength is disproportionate to the change in density (Marcus & Bouxsein 2010). However, this non linear relationship between

bone density and resultant mechanical properties can be explained by taking into account variations in bone volume fraction, trabecular orientation, trabecular interconnectivity and a structural anisotropy resulting in a linear relationship between bone density and mechanical properties for loading along the main trabecular orientation (Silva & Gibson 1997; Keaveny et al. 2001). Therefore it is clear that there is a strong effect of the geometry and organizational structure on the mechanical properties of bone.

Osteoporosis lowers the strength of cortical bone, as is the case for trabecular bone, due to decreases in the degree of mineralization and increases in porosity (Currey 1988; Schaffler & Burr 1988) or increases in mineralization due to the continuous aggregations of mineral without resorption (Grynpas 1993). Additional structural changes in cortical bone induced by osteoporosis include collagen content and orientation of collagen fibrils, the extent and nature of collagen cross-linking (Burr 2002), the number and composition of cement lines (Burr, Schaffler & Frederickson 1988) and the presence of fatigue-induced micro-damage (Burr et al. 1997; Burr 2003). These latter factors affecting bone mechanical properties are more closely related to bone at lower hierarchical levels.

The structural changes in osteoporotic bone at higher hierarchical levels, mainly dependent on reduction of bone mass, clearly define the elastic modulus and strength of whole bone. However, the effect of osteoporosis on bone material at lower hierarchical levels remains uncertain such that density alone cannot account for the decrease in stiffness and strength of

trabecular bone, and the strains at which bone fails are almost independent of density (Keaveny et al. 2001). At the lower hierarchical level of bone, all geometric and structural factors can be ignored and the effect of bone mass can be removed allowing for the quality of the bone material to be tested alone. The effect of the quality of bone on its mechanical properties is important as it has been obvious that current diagnosis methods purely based bone density scales from x-ray scans and treatments are not optimal. Recently the National Osteoporosis Guideline Group (NOGG) has placed guidelines for the diagnosis of osteoporosis "FRAX" which takes into account the patient's medical history along with the x-ray measured bone mineral density (BMD) index. BMD alone has been a poor indicator for potential increases in bone fragility and is only able to predict 60% of the variations in bone strength (Ammann & Rizzoli 2003). The quality of the bone material brought on by a patient's lifestyles and other factors affecting the quality of bone material has been suggested as being an important consideration in determining bone fragility due to osteoporosis (WHO 2012).

Due to the strong impact mineral content seems to have on bone fragility, different techniques have been developed and used in order to asses quantify the mineral content of bone in an attempt to quantify the quality of bone material and not only overall bone mass density as is achieved currently. These techniques include microradiography (Bovin & Baud 1984; Boivin & Meunier 2002), quantitative backscattered electron imaging (qBEI) (Roschger et al. 2003) and synchrotron radiation micro computed

tomography (SRμCT) (Borah et al. 2005). All of these methods perform measurements in what is referred to as bone mineralization density distribution (BMDD). BMDD is a measure of the mineral content in small areas defined as image pixels or voxels and can distinguish local variations in mineral content. Bone mineral density (BMD) is a potentially poorer description of osteoporosis as an estimate of the total amount of mineral in a scanned area of whole bone is made but is the current method used clinically (Roschger et al. 2008). Imaging techniques used to quantify bone mineral distribution have been previously combined with addition structural or mechanical testing, notably nanoindentation (Guo & Goldstein 2000), scanning acoustic microscopy (SAM) (Katz & Meunier 1993), Raman spectroscopy (McCreadie et al. 2006) and fourier transform infrared imaging (FTIRI) (Paschalis et al. 2004) in order to correlate mineral content to structure and function relationships (Roschger et al. 2008).

Compositional changes in bone material due to osteoporosis have been shown to decrease the degree of mineralization and collagen cross-linking resulting in bone fragility (Paschalis et al. 2004; Marcus & Bouxsein 2010). Reductions in the degree of mineralization have been further emphasised as detrimental to the material properties of bone (Ciarelli, Fyhrie & Parfitt 2003). The stiffness versus toughness of bone is determined in part by the mineral content (Currey 1988; McCreadie et al. 2006) but when there is an increase or a decrease in the optimal level of mineralization the balance of stiffness versus toughness in bone is lost which in turn increases bone

fragility (Roschger et al. 2008). In case of osteoporosis, a decrease or an increase in mineralization may therefore be detrimental to the mechanical properties of bone (Ciarelli, Fyhrie & Parfitt 2003; Roschger et al. 2008). Low mineralization levels, or hypomineralization, cause reductions in stiffness and strength while high mineralization levels, or hypermineralization, reduce fracture toughness (Ciarelli, Fyhrie & Parfitt 2003). Hypomineralization occurs either due to lack of time for secondary mineralization to occur after remodelling or due to pathological conditions affecting mineralization. On the other hand hypermineralization can only occur if there are changes in crystal size or shape that could lead to a higher mineral density (Roschger et al. 2008).

The significance of changes in the properties of bone material has led to works that attempt to measure mechanical properties of bone at small length scales, thus ignoring geometric effects at higher hierarchical levels. The first set of experiments at the microstructural level were performed by Guo et al. 2000 using nanoindentation tests on trabeculae from the lumbar region of 17 month old control and ovariectomized sprague dawley rats. These results showed no change in elastic modulus or hardness at the microscopic level between control and diseased specimens (Guo & Goldstein 2000), suggesting osteoporosis does not change the material properties of bone but instead only induces changes in bone density. An almost exact same study performed by Maïmoun et al. in 2012 shows a similar reduction in bone loss due to a depletion in estrogen in sprague dawley ovariectomized rats but a reduction in the elastic modulus in trabecular bone which contradicts the results

presented by Guo et al. 2000 (Maïmoun et al. 2012). The experimental results for these two significant pieces of literature are shown in Table 7.2. Maïmoun et al. attributes differences in their mechanical properties relative to the work of Guo et al. as due to variations in bone hydration levels.

Other studies attempting to assess the effect of osteoporosis on the mechanical properties of bone have also shown significant mechanical variations. Fratzl-Zelman et al. performed nanoindentation on cross-sections of osteoporotic versus healthy bone of female human femurs and found no change in elastic modulus even though the results of the qBEI analysis showed a lower mineralization level for the osteoporotic samples. Fratzl-Zelman et al. attributed the constant bone elastic modulus despite mineral loss from osteoporosis to changes in the organic matrix. Specifically, increasing the stiffness of the organic matrix can occur with an increase in the cross-linking pattern of the organic matrix in order to compensate for the low mineral content or a change in the mineral-organic interface during osteoporosis. Although there is no evidence that correlates osteoporosis with increased bone turnover, there is a decrease in mineralization found in trabecular bone of post-menopausal women with osteoporosis which is attributed to increased bone turnover (Fratzl-Zelman et al. 2009), so the key could lie in changes of the collagen matrix which in turn cause alterations in bone mineralization resulting in a decrease in mineralization levels. Increased bone-turnover increases the amount of low mineralized bone as it is mainly new bone that has just been laid down (Fratzl-Zelman et al. 2009). However, the samples tested by Fratzl-Zelman were notable as being dry,

similarly to the samples tested by Guo et al.. Conversely, nanoindentation performed by Silva et al. on dry bone material from mice bred to model osteoporosis due to aging show that the elastic modulus values are higher for the osteoporotic bone than the control. This result is suspected due to the increase in mineralization with age (Silva et al. 2004), which is different to the changes in mineralization due to hormonal imbalances. Boskey et al. states that, as bone ages, the mineral content decreases while the average crystal size increases but the distribution of the crystal size narrows, which in turn results in a weaker bone material (Boskey 2003). The resultant variability in nanoindentation data makes correlation with structural and biochemical observations difficult. This chapter therefore attempts to address this conflict by mechanically testing bone micro-beams in compression to failure. As in previous chapters, bone micro-beams were fabricated using FIB but mechanical testing was performed in compression as a more physiologically relevant loading state (McBroom et al. 1985; Silva et al. 2004; Cory et al. 2010). Thus, the effect of osteoporosis at the lamellar level, which is representative of the bone material, is carried out.

7.2 Materials and methods

Researchers have turned to the use of rats in order to have a controlled environment to study the effects of osteoporosis (Frost & Jee 1992; Guo & Goldstein 2000). The practicality of using rats as test subjects is that osteoporosis can be induced in rats through estrogen depravation by

performing an ovariectomy and many scenarios can be explored due to the highly controlled manner in which the rats can be kept. The rat model has been used extensively and is widely accepted as an adequate animal model for postmenopausal osteoporosis (Frost & Jee 1992; Guo & Goldstein 2000).

Ovariectomized and control rat femurs were obtained from Hebrew University of Jerusalem in order to compare the mechanical properties of osteoporotic and healthy bone. Cantilever beams were created using a Focused Ion Beam (FIB) as detailed in Chapter 3. Since this set of beams was to be tested in compression, average micro-beam dimensions of 8x2x2 μm were used. The dimensions of the beams were chosen by using the same principles that determined the appropriate dimensions of the beams tested in buckling as described in Chapter 6. In the case of the micro-beams tested in compression, the slenderness ratio was therefore kept lower than the critical slenderness ratio for the buckling in order to induce clear compression. The FIB patterning of the micro-beams at the edge of the cut bone sample was performed such that the orientation of the beams was in the same axis as that of the AFM tip. This orientation ensured that the AFM tip would apply compressive forces to the bone micro-beams. An SEM image showing the orientation of the AFM tip relative to the FIB patterned macro-cantilever beams is shown in Figure 7.1 below. The dimensions of the beams were carefully measured using SEM for subsequent stress-strain calculations.

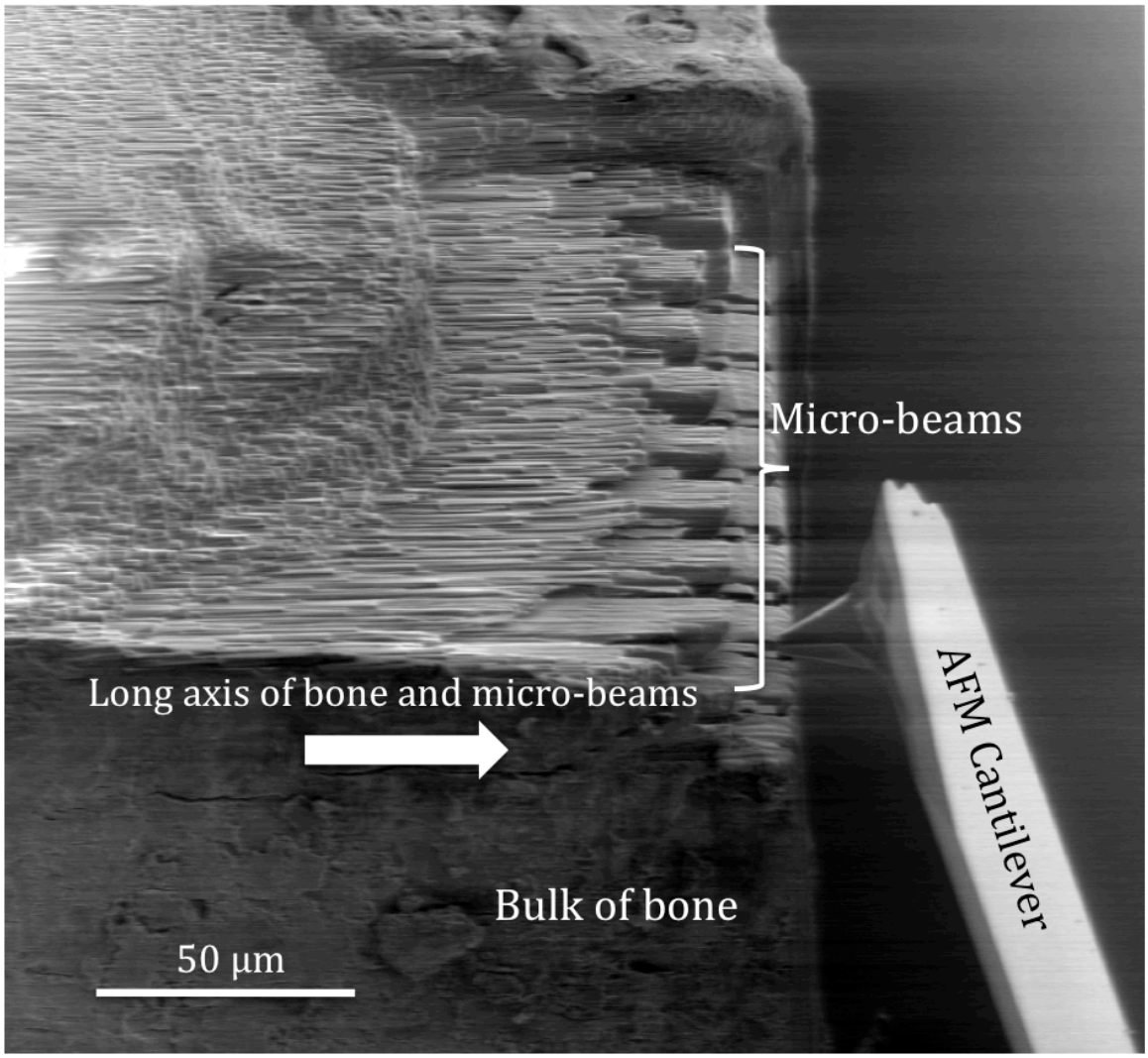

Figure 7.1 SEM micrograph of an AFM cantilever tip approaching a bone micro-beam for in situ mechanical testing. The arrow indicates the direction of the long axis of bone and micro-beam principal axis.

Compression tests were performed inside the chamber of an SEM dual-beam system (Quanta 3D FEG, FEI, USA/EU) so that deformation of the bone micro-beam could be correlated with mechanical information recorded by the AFM system. Misalignment or slippage between the AFM tip and micro-beam sample that could cause underestimation or overestimation of the recorded mechanical properties can also be monitored using SEM imaging.

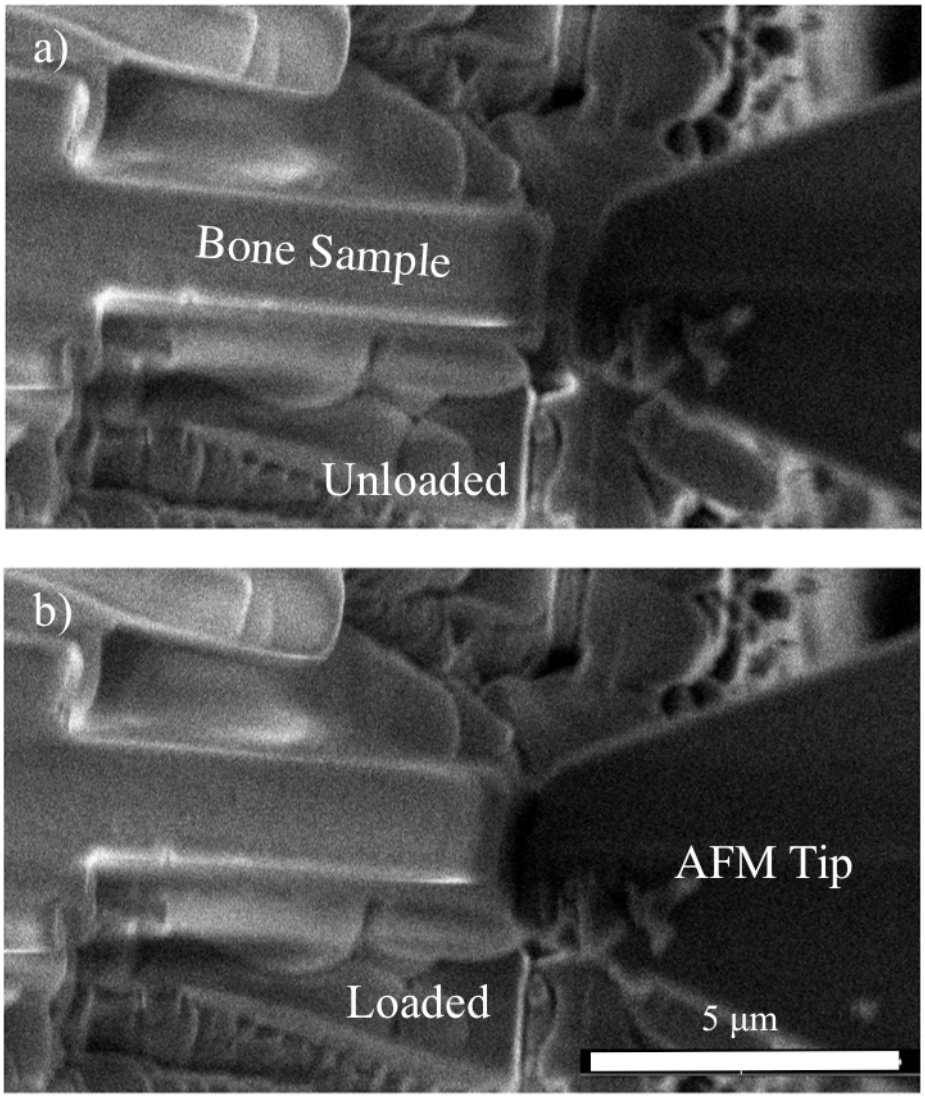

Figure 7.2 SEM micrographs showing compression of rat bone micro-beams a) in the unloaded state with the AFM tip away from the bone micro-beam and b) during contact of the AFM tip with the bone micro-beam causing loading.

Mechanical compression tests were performed in a similar fashion to the beam bending experiments of Chapters 4-6 except the orientation of the beams was in the same axis as that of the AFM tip as shown in Figure 6.5. In-situ SEM was used to observed the movement of the AFM tip towards the end of the micro-beam and ensure that the top of the beam fully contacted with

the AFM tip as shown in Figure 7.2. SEM observation was critical in this manipulation step as the SEM out-of-plane depth is somewhat restricted and caused a number of 'false' contacts where the AFM tip appears contact the beam but is actually either above or below the plane of the beam. These false contacts are confirmed from a lack in deformation in the beam as the AFM tip is moved into the beam.

7.3 Results and discussion

Mechanical testing in compression is preferred as a precise method to compare two different samples, in this case osteoporotic and control/healthy bone. Compression is not usually the preferred method to obtain accurate mechanical properties due to difficulties in applying load along the principal axis of the sample. The main inaccuracy in the compression test occurs due to misalignment of the loading surfaces and friction resulting in high strains at boundary regions causing overestimation of the strain, which in turn underestimates the elastic modulus (An & Draughn 2000). This inaccuracy can be corrected by measuring the strain using the SEM imaging through the middle of the test sample.

Micro-beams were created on both diseased/osteoporotic and healthy/control bone samples from sprague dawley rat femora as achieved in the previous chapters. Six beams from the control and four from the osteoporotic bone were tested in compression to failure using methods described in Chapters 3 and 4. The stress and strain induced in the micro-

beams was calculated using the force-deflection curves gathered from the AFM system and by analysing the SEM images collected during mechanical testing and translating into stress-strain curves. Stress is calculated by dividing the force applied to the sample by the AFM tip by the cross-sectional area of the micro-beam sample whereas strain is calculated by dividing the change in length by the total micro-beam sample length as shown in Equations 41 and 42.

$$\sigma = \frac{f}{A} \qquad \text{Eqn. 41}$$

$$\varepsilon = \frac{\Delta L}{L_0} \qquad \text{Eqn. 42}$$

Where σ is stress in the compressed micro-beam sample, *f* is force, A is the micro-beam cross-sectional area, ε is the strain in the bone micro-beam, ΔL is change in length of the beam and L_0 is the original length of the bone micro-beam. The stress-strain behaviour for the osteoporotic and control bone micro-beams is shown in Figure 7.3 below.

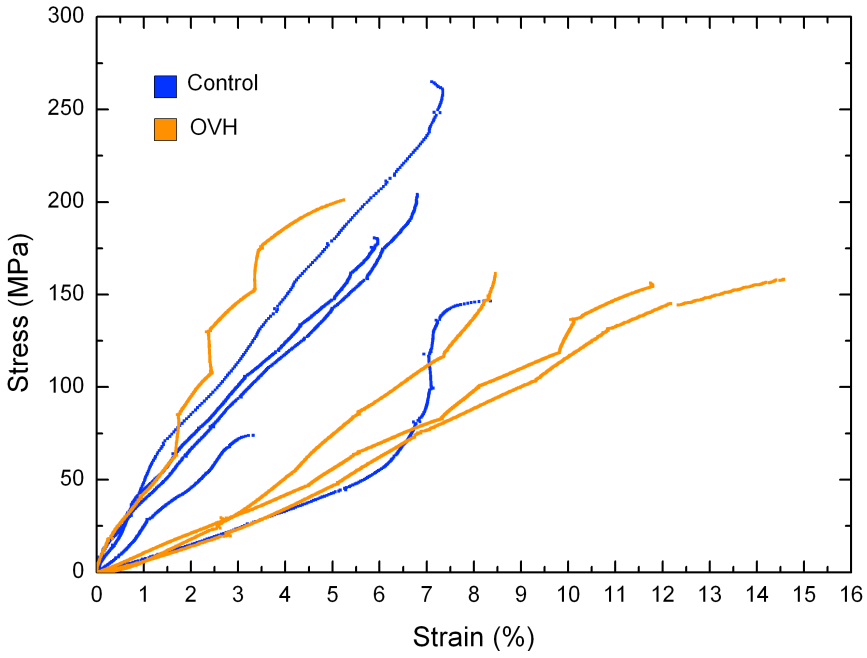

Figure 7.3 Stress-strain curves for compression of control and ovariectomized (OVH) rat bone micro-beams.

The elastic modulus, strength and the strain to failure values calculated from the bone micro-beam compression tests in Figure 7.3 are shown in Table 7.1 below. As can be seen from the stress-strain curves, there is a marked difference between the osteoporotic and the control samples except for one curve of each. The exceptions are probably due to an orientation effect as has been discussed in Chapter 5. The osteoporotic bone has an average elastic modulus of 1.59±1.26 GPa, almost half the value of the elastic modulus of the control sample which is 2.9±1.45 GPa. In terms of strength both ovariectomized and control samples have the same values of 169.23±21.35 MPa and 169.51±66.19 MPa respectively while the % strain varies with the ovariectomized samples reaching higher strains to failure than the control samples.

Table 7.1 Elastic modulus, strength and strain to failure values of both control and ovariectomized (OVH) rat femur bone micro-beams tested in compression.

Beam No.	Elastic Modulus (GPa)	Strength (MPa)	Strain %
Control			
Average	2.9±1.45	169.51±66.19	6.3±1.89
1	3.06	204.22	6.8
4	3.62	180.53	5.88
5	2.37	73.91	3.32
6	4.65	248.35	7.16
8	0.78	140.52	8.35
OVH			
Average	1.59±1.26	169.23±21.35	10±4.04
1	3.46	201.09	5.24
2	1.08	156.17	8.46
3	1.07	161.38	11.74
4	0.74	158.26	14.57

The mechanical properties of the osteoporotic bone micro-beams in this work can be related to previous work. A range of methods have been used to assess the change in mechanical properties of bone due to osteoporosis at many different hierarchical levels and are summarized in Table 7.2.

Table 7.2 Typical mechanical properties of rat bone

	State	Testing method	Strength (MPa)	Elastic Modulus (GPa)	Reference
Macrostructural level					
Whole Bone	Healthy	3-point bending	180±6	6.9±0.3	(Jorgensen, Bak & Andreassen 1991)
Whole Bone	Healthy	3-point bending	134±4	8±0.4	(Barengolts et al. 1993)
Whole Bone	Healthy	3-point bending	153±45	4.9±4	(Ejersted et al. 1993)
Architectural level					
Cross section (1 mm thick)	Healthy (Cortical)	Compression	139.5±19.14	8.8±2.5	(Cory et al. 2010)
Cross section (1 mm thick)	Osteoporotic (Cortical)	Compression	127.24±35.04	7.3±2.7	(Cory et al. 2010)
Cross section (1 mm thick)	Healthy (Trabecular)	Compression	35.95±15.62	2.2±0.92	(Cory et al. 2010)
Cross section (1 mm thick)	Osteoporotic (Trabecular)	Compression	26.89±22.35	1.02±0.79	(Cory et al. 2010)
Beams (1mm thick)	Healthy	3-point bending	-	5.12±0.77	(Kasra et al. 1997)
Beams (1mm thick)	Osteoporotic	3-point bending	-	4.70±0.98	(Kasra et al. 1997)
Sub-microstructural level (sub-lamellar/material level)					
Lamellar (25 μm^2 indent)	Healthy (Trabecular)	Nanoindentation	-	16.1±3.9	(Guo & Goldstein 2000)
Lamellar (25 μm^2 indent)	Osteoporotic (Trabecular)	Nanoindentation	-	15.8±3.9	(Guo & Goldstein 2000)
Lamellar	Healthy (Cortical)	Nanoindentation	-	18.98±4.78	(Cory et al. 2010)
Lamellar	Healthy (Trabecular)	Nanoindentation	-	18.27±4.26	(Cory et al. 2010)
Lamellar	Healthy (Trabecular)	Nanoindentation	-	18.73±0.71	(Maïmoun et al. 2012)
Lamellar	Osteoporotic (Trabecular)	Nanoindentation	-	16±0.85	(Maïmoun et al. 2012)
Lamellar	Healthy (Cortical)	Nanoindentation	-	21.27±1.2	(Maïmoun et al. 2012)
Lamellar	Osteoporotic (Cortical)	Nanoindentation	-	21.12±1.12	(Maïmoun et al. 2012)

The results shown in Table 7.2 indicate no direct evidence of osteoporosis affecting the elastic modulus of bone at lower levels except in the case of the study by Maïmoun et al., which show a decrease in the elastic modulus measured via nanoindentation as has been previously discussed. The lack of change in the elastic modulus of bone due to osteoporosis in previous studies contradicts the results of this study, which shows a clear decrease of bone elastic modulus properties with osteoporosis as shown in Figure 7.3. This lowering of the elastic modulus of osteoporotic bone has been suggested as being due to mechanical degradation of the collagen in osteoporotic bone from reductions in the level of immature collagen cross-links and decreases in collagen fibril diameters (Currey 2003). Compositional changes in collagen, such as the ratio of $\alpha 1$ to $\alpha 2$ chains in different phenotypes of COLIA1 found in Type 1 collagen, seem to affect the fracture risk of bone independently of the changes in bone mass (McGuigan et al. 2001). The results in this chapter therefore indicate that osteoporosis might cause a decrease in the elastic modulus of bone material at the sub-lamellar level due possible structural changes in the collagen. These decreases in bone material elastic modulus due to osteoporosis have failed to be verified using nanoindentation. Previous studies state that indeed, modifications of the organic matrix seem to give origin to an increase in bone fragility as a stiffer organic matrix would in turn increase bone fragility. However they are unable to detect it through nanoindentation and hypothesize that there seems to be a compensation mechanism which by increasing the organic matrix stiffness, there is a decrease in the mineral content which results in

similar hardness elastic modulus values for both diseased and healthy (Fratzl-Zelman et al. 2009).

7.4 Conclusion

The compressive elastic modulus, strength and strain to failure of bone micro-beams were measured in order to assess the effect of osteoporosis on the mechanical properties of bone as a material at the sub-lamellar level. Although compression testing herein cannot be directly compared to previous studies in the literature, results showed a decrease in the elastic modulus of osteoporotic bone compared to a control. This decrease in the elastic modulus with osteoporosis was additionally associated with little change in micro-beam strength and a small increase in failure strain. The origin of osteoporotic induced decreases in bone elastic modulus was suggested as being due to mechanical degradation of the collagen within the bone material.

Chapter 8. Conclusions and future work

8.1 Summary

Bone cantilever beams were tested in bending and compressive loading modes in order to assess the material mechanical properties of the basic unit of bone. These sub-lamellar bone micro-cantilever beams were created using FIB methods and tested in situ via a custom built AFM within an SEM. Results indicate an opportunity to mechanically deform hydrated bone materials in vacuum environments while observing using in situ SEM. A clear correlation between the orientation of the mineralized collagen fibres and the elastic modulus was observed when bending bone micro-beams, which is consistent with the Halpin-Tsai model describing the theoretical mechanical behaviour of a composite. Thus, bone was successfully tested as a composite material at the sub-lamellar level and the mechanical properties were correlated to a rotating plywood fibre orientation. Unnotched bone cantilever beams were further tested to failure in two loading modes of bending and buckling. The work-to-fracture, strength and the elastic modulus were calculated for each of the micro-beams tested in order to assess the effect of collagen orientation on fracture properties of bone. The work-to-fracture for micro-beams in bending exhibited an inverse correlation with the elastic modulus while the opposite is observed for tests performed in buckling. Finally, compression testing of micro-beams with particularly short aspect ratios were applied to evaluate the quality of bone material in osteoporotic versus healthy bone. A

clear decrease in the elastic modulus of osteoporotic bone relative to healthy bone control samples was observed, despite little change in micro-beam compressive failure strength and strain.

8.2 Literature review comparison

This study is the first to measure the mechanical properties of rat bone in bending, buckling and compression at the sub-lamellar level using in situ AFM-SEM techniques. While testing in the vacuum conditions of the SEM was justified as being suitable for examining hydrated bone micro-beams, subsequent mechanical testing results should be compared to literature values for bone material. Table 8.1 shows the mechanical properties of rat bone at different hierarchical levels tested using a range of experimental methods. From the table, it is clear that the results from the bending and the compression tests at different hierarchical levels are similar to the results recorded by the methods developed in this study. The reason for this similarity is due to the nature of the larger testing methods, as they closely resemble the loading conditions used in this study. However, the results presented from the micro-beam mechanics of this work deviate significantly from previous nanoindentation testing. As discussed in previous chapters, nanoindentation represents an unusual loading condition as bone material rarely adapts to resist puncture-like loading conditions so should be treated with caution. Mechanical testing of bone micro-beams therefore allow evaluation of the material behaviour of bone, removing the influence of

higher level hierarchical structure, in much more physiologically relevant state such as bending, buckling and compression.

For the purpose of this study, both the rate of testing and the volume were kept constant. In terms of rate this was important due to the fact that bone is a viscoelastic material and therefore the mechanical properties would be affected by the rate of testing. All tests done in this work were performed at the same rate of 0.04 $\mu m.s^{-1}$. The small volumes tested in this work mean that there could be a volume effect affecting the results. It is a known fact that there is a direct correlation of increased mechanical properties with decrease in volume as the number of defects such as micro cracks decrease with decreasing volume. This effect however was not observed in this work, the results for bending tests performed in previous studies on larger specimens match those from bending tests performed in this work, which is on much smaller samples, indicating that it is the sub-lamellar level which dominates the overall mechanical properties of bone including fracture properties as previously discussed in Chapter 6 with references to the work by Peterlik et al. (2006) (Peterlik et al. 2006).

Table 8.1 Mechanical properties of rat bone recorded at various hierarchical levels using a range of testing methods.

	Type	Testing method	Strength (MPa)	Elastic Modulus (GPa)	Reference
Macrostructural level					
Whole Bone		3-point bending	180±6	6.9±0.3	(Jorgensen, Bak & Andreassen 1991)
Whole Bone		3-point bending	134±4	8±0.4	(Barengolts et al. 1993)
Whole Bone		3-point bending	153±45	4.9±4	(Ejersted et al. 1993)
Architectural level					
Cross section (1 mm thick)	Cortical	Compression	139.5±19.14	8.8±2.5	(Cory et al. 2010)
Cross section (1 mm thick)	Trabecular	Compression	35.95±15.62	2.2±0.92	(Cory et al. 2010)
Beams (1mm thick)	Cortical	3-point bending	-	5.12±0.77	(Kasra et al. 1997)
Sub-microstructural level (sub-lamellar/material level)					
Lamellar (25 μm^2 indent)	Trabecular	Nanoindentation	-	16.1±3.9	(Guo & Goldstein 2000)
Lamellar	Cortical	Nanoindentation	-	18.98±4.78	(Cory et al. 2010)
Lamellar	Trabecular	Nanoindentation	-	18.27±4.26	(Cory et al. 2010)
Lamellar	Cortical	Nanoindentation	-	21.27±1.2	(Maïmoun et al. 2012)
Lamellar	Trabecular	Nanoindentation	-	18.73±0.71	(Maïmoun et al. 2012)
Lamellar	Cortical	Micro-beam bending	843.33±157.96	7.63±3.42	This study
Lamellar	Cortical	Micro-beam buckling	196.17±104.72	8.81±7.9	This study
Lamellar	Cortical	Micro-beam in compression	169.51±66.19	2.9±1.45	This study

8.3 Future work

Future work involves continuing to measure the mechanical properties of bone at the sub-lamellar level. The aims of future work would be to use sub-lamellar micro-cantilever bone beams to isolate distinct features of bone that are expected to contribute to the mechanical properties of bone material. One particularly important feature is the cement line present at the osteon perimeter that has been previously shown to blunt crack tips through promotion of micro-cracking at cement lines (Koester, Agar et al.).

In order to test the ability of cement lines to deflect cracks on the mechanical properties of bone, preliminary rat bone femurs were prepared as described in Chapter 3. The sample was mounted so that a transverse cut exposes osteons and possibly cement lines in plain view as shown in Figure 8.1.

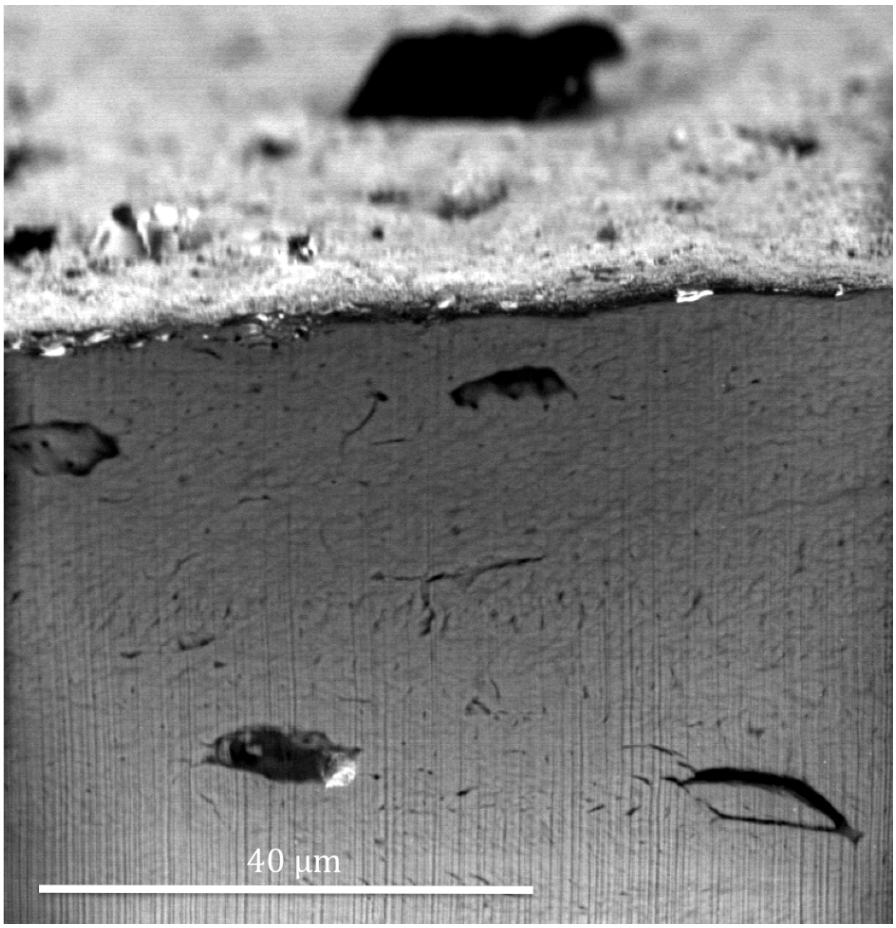

Figure 8.1 BSED-SEM image of a FIB cleaned section at the edge of a rat bone sample. Circular osteon features are observed but cement lines, expected to appear as bright in BSED due to high mineral content, are difficult to identify. The long axis of the bone in this case is perpendicular to the milled surface.

Preliminary work on rat bone is problematic as rat femurs rarely have secondary osteons and therefore few cement lines. Furthermore, potential etching is required in order to observe cement lines using SEM. The etching would most certainly have an effect on the mechanical properties of bone and would be unsuitable. For example, etching using an acid will damage bone tissue due to dissolution of a number of components, especially the mineral content. FIB patterned micro-beams have therefore been shown in Figure 8.2 but cement lines are not identifiable.

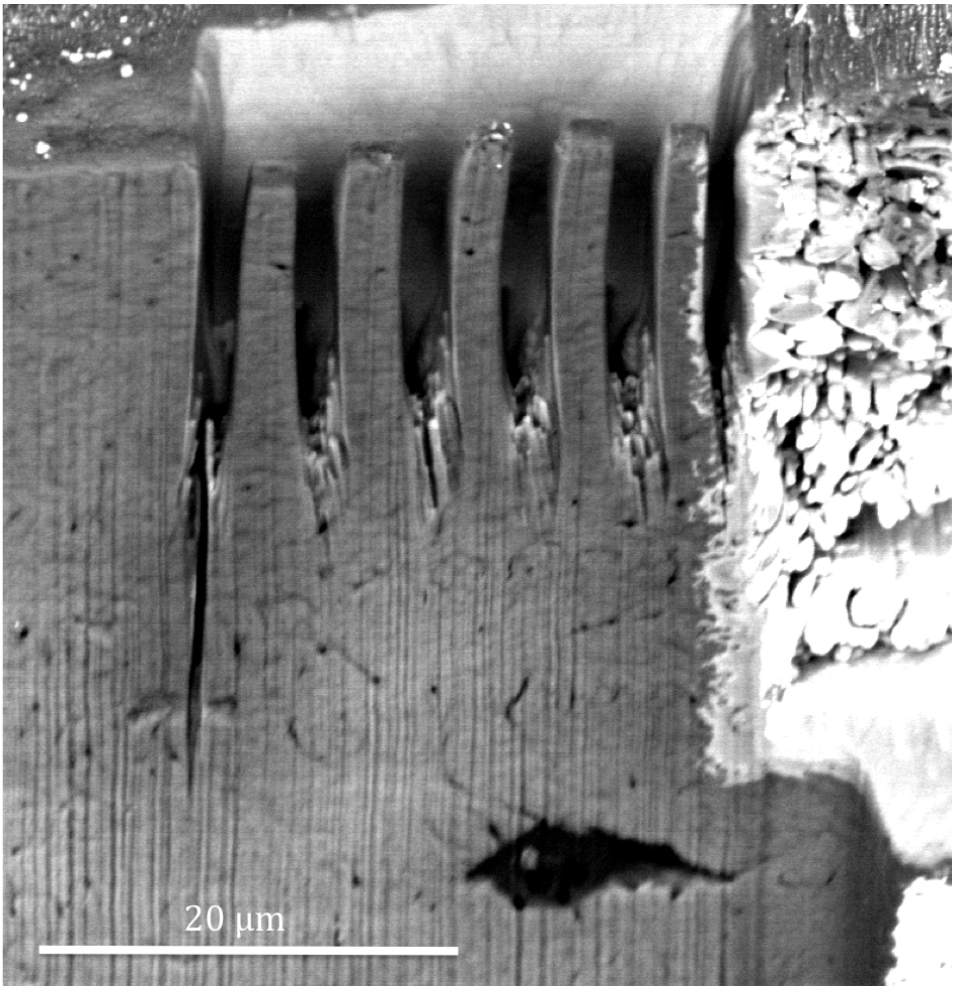

Figure 8.2 BSED-SEM image of the initial process of the milling of micro-beams on the edge of a rat bone sample. The beams are milled around bone features such as vascular canals in order to try to isolate cement lines.

Future work must therefore firstly prepare samples where cement lines can be clearly observed using BSED-SEM. The fabrication of a micro-beam containing a cement line will be effective in quantifying the influence of cement lines on overall bone toughness. Bending of a micro-beam containing a cement line to failure will cause likely crack propagation at the interface between the cement line and the surrounding bone material, especially as cement lines are expected to promote failure. Thus, the work done to fail the

cement line interface will be measured and, by considering the total number of cement line involved in bone failure, their overall contribution to bone toughness can be made.

References

Aibrecht, T. R. and C. F. Quate (1987). "Atomic resolution imaging of a nonconductor by atomic force microscopy." Journal of Applied Physics **62**(7): 2599-2602.

Akiva, U., H. D. Wagner and S. Weiner (1998). "Modelling the three-dimensional elastic constants of parallel-fibred and lamellar bone." Journal of Materials Science **33**: 1497-1509.

Ammann, P. and R. Rizzoli (2003). "Bone strength and its determinants." Osteoporosis International **14**(Supplement 3).

An, Y. H. and R. A. Draughn, Eds. (2000). Mechanical Testing of Bone and the Bone-Implant Interface. New York, CRC Press.

Arteaga-Solis, E., L. Sui-Arteaga, M. Kim, M. B. Schaffler, K. J. Jepsen, N. Pleshko and F. Ramirez (2011). "Material and mechanical properties of bones deficient for fibrillin-1 or fibrillin-2 microfibrils." Matrix Biology **303**: 188-194.

Ascenzi, A., A. Benvenuti and E. Bonucci (1982). "The Tensile Properties of Single Osteonic Lamellae: Technical Problems and Preliminary Results." Journal of Biomechanics **15**(1): 29-37.

Ascenzi, A. and E. Bonucci (1968). "The compressive properties of single osteons." Anatomical Record **161**: 377-392.

Ascenzi, A. and E. Bonucci (1972). "The shearing properties of single osteons." The Anatomical Record **172**(3): 499-510.

Ascenzi, A. and E. Bonucci (1976). "Mechanical similarities between alternate osteons and cross-ply laminates." Journal of Biomechanics **9**(2): 65-71.

Ascenzi, A. and E. Bonucci (1990). "The bending properties of single osteons." Journal Biomechanics **23**: 763-771.

Ascenzi, A., E. Bonucci and B. Ds. (1965). "An electron microscope study of osteon calcification." J. Ultrastruct Res **12**: 287.

Ascenzi, A., E. Bonucci, A. Ripamonti and N. Roveri (1978). "X-ray diffraction and electron microscope study of osteons during calcification." Calcified tissue research **25**: 133-143.

Ascenzi, M. G., A. Ascenzi, A. Benvenuti, M. Burghammer, S. Panzavolta and A. Bigi (2003). "Structural differences between “dark” and “bright” isolated human osteonic lamellae." Journal of Structural Biology **141**(1): 22-33.

Ashman, R. B., S. C. Cowin, W. C. V. Buskirk and J. C. Rice (1984). "A continuous wave technique for the measurement of the elastic properties of cortical bone." Journal Biomechanics **17**(5): 349-361.

Barengolts, E. I., D. J. Curry, M. S. Bapna and S. C. Kukreja (1993). "Effects of Endurance Exercise on Bone Mass and Mechanical Properties in Intact and Ovariectomized Rats." Journal of Bone and Mineral Research **8**(8): 937-942.

Beck, K. and B. Brodsky (1998). "Supercoiled Protein Motifs: The Collagen Triple-Helix and the a-Helical Coiled Coil." Journal of Structural Biology **122**: 17-29.

Behiri, J. C. and W. Bonfield (1984). "Fracture Mechanics Of Bone-The Effects Of Density, Specimen Thickness And Crack Velocity On Longitudinal Fracture." Journal of Biomechanics **17**(1): 25-34.

Bella, J., B. Brodsky and H. M. Berman (1995). "Hydration structure of a collagen peptide." Structure **39**: 893-906.

Bigley, R. F., L. V. Griffin, L. Christensen and R. Vandenbosch (2006). "Osteon interfacial strength and histomorphometry of equine cortical bone." Journal of Biomechanics **39**(9): 1629-1640.

Binning, G., H. Rohrer, C. Gerber and E. Weibel (1982). "Surface Studies by Scanning Tunneling Microscopy." Physical Review Letters **49**(1): 57-61.

Blodgett, O. W. (1991). Design of Welded Structures.14th. Cleveland, Ohio, The James F. Lincoln Arc Welding Foundation.

Boivin, G. and P. J. Meunier (2002). "The Degree of Mineralization of Bone Tissue Measured by Computerized Quantitative Contact Microradiography." Calcified Tissue International **70**(6): 503-511.

Bonar, L. C., A. H. Roufosse, W. K. Sabine, M. D. Grynpas and M. J. Glimcher (1983). "X-ray diffraction studies of the crystallinity of bone mineral in newly synthesized and density fractioned bone." Calcified Tissue International **35**: 202-209.

Bonfield, W. and P. K. Datta (1976). "Fracture Toughness Of Compact Bone." Journal of Biomechanics **9**: 131-134.

Bonfield, W., M. D. Grynpas and R. J. Young (1978). "Crack Velocity and the Fracture of Bone." Journal of Biomechanics **11**: 473-479.

Bonfield, W. and C. H. Li (1966). "Deformation and fracture of bone." J. Appl. Phys. **37**(2): 869-875.

Borah, B., E. L. Ritman, T. E. Dufresne, S. M. Jorgensen, S. Liu, J. Sacha, R. J. Phipps and R. T. Turner (2005). "The effect of risedronate on bone mineralization as measured by micro-computed tomography with synchrotron radiation: Correlation to histomorphometric indices of turnover." Bone **37**(1): 1-9.

Bornstein, P. and H. Sage (1980). "Structurally Distinct Collagen Types." Ann. Rev. Biochem **49**: 957-1003.

Boskey, A. (2003). "Bone mineral crystal size." Osteoporosis International **14**(Supplement 5): 16-21.

Bouxsein, M. (2001). Biomechanics of age-related fractures. Osteoporosis. 2nd. R. Marcus, D. Feldman and J. Kelsey. San Diego, Academic Press**:** 509-534.

Bovin, G. and C. A. Baud (1984). Microradiographic methods for calcified tissues. Methods for calcified tissue preparation G. R. Dickson. Amsterdam, Elsevier**:** 391-411.

Boyd, S. K. and B. M. Nigg (2007). Bone. Biomechanics of the Musculo-skeletal System B. M. Nigg and W. Herzog. Canada, Wiley**:** 65-94.

Boyde, A. and S. J. Jones (1996). "Scanning Electron Microscopy of Bone: Instrument, Specimen, and Issues." Microscopy Research and Technique(33): 92-120.

Bromage, T. G., H. M. Goldman, S. C. McFarlin, J. Warshaw, A. Boyde and C. M. Riggs (2003). "Circularly Polarized Light Standards for Investigations of Collagen Fiber Orientation in Bone." The Anatomical Reocrd (Part B: New Anat) **274B**: 157-168.

Brown, W. L., T. Venkatesan and A. Wagner (1981). "Ion-Beam Lithography." Nuclear Instruments & Methods in Physics Research **191**(1-3): 157-168.

Burr, D. (2003). "Microdamage and bone strength." Osteoporosis International **14**(5): S67-S72.

Burr, D. B. (2002). "The Contribution of the Organic Matrix to Bone's Material Properties." Bone **31**(1): 8-11.

Burr, D. B., M. R. Forwood, D. P. Fyhrie, R. B. Martin, M. B. Schaffler and C. H. Turner (1997). "Bone Microdamage and Skeletal Fragility in Osteoporotic and Stress Fractures." Journal of Bone and Mineral Research **12**(1): 6-15.

Burr, D. B., M. B. Schaffler and R. G. Frederickson (1988). "Composition of the Cement Line and its Possible Mechanical Role as a Local Interface in Human Compact Bone." Journal Biomechanics **21**(11): 939-945.

Butt, H. J., B. Cappella and M. Kappl (2005). "Force measurements with the atomic force microscope: Technique, interpretation and applications." Surface Science Reports **59**: 1-152.

Carter, D. R. and W. C. Hayes (1976). "Bone Compressive Strength: The Influence of Density and Strain Rate." Science **149**(4270): 1174-1176.

Chan, Y. L., A. H. W. Ngan and N. M. King (2009). "Use of focused ion beam milling for investigating the mechanical properties of biological tissues: A study of human primary molars." Journal of the Mechanical Behavior of Biomedical Materials **2**: 375-383.

Chen, P. Y., A. G. Stokes and J. McKittrick (2009). "Comparison of the structure and mechanical properties of bovine femur bone and antler of the North American elk (*Cervus elaphus canadensis*)." Acta Biomaterialia **5**: 693-706.

Choi, K., J. L. Kuhn, M. J. Ciarelli and S. A. Goldstein (1990). "The elastic moduli of human subchondral, trabecular, and cortical bone tissue and the size-dependency of cortical bone modulus." Journal Biomechanics **23**(11): 1102-1113.

Ciarelli, T. E., D. P. Fyhrie and A. M. Parfitt (2003). "Effects of vertebral bone fragility and bone formation rate on the mineralization levels of cancellous bone from white females." Bone **32**(3): 311-315.

Cory, E., A. Nazarian, V. Entezari, V. Vartanians, R. Müller and B. D. Snyder (2010). "Compressive axial mechanical properties of rat bone as functions of bone volume fraction, apparent density and micro-ct based mineral density." Journal of Biomechanics **43**(5): 953-960.

Currey, J. D. (1979). "Mechanical Properties Of Bone Tissues With Greatly Differing Functions." Journal of Biomechanics **12**: 313-319.

Currey, J. D. (1988). "The Effect of Porosity and Mineral Content on the Young's Modulus of Elasticity of Compact Bone." Journal Biomechanics **21**(2): 131-139.

Currey, J. D. (1988). "The Effects of Drying and Re-wetting on some mechanical properties of cortical bone." Journal of Biomechanics **21**(5): 439-441.

Currey, J. D. (1999). "The design of mineralised hard tissues for their mechanical functions." Journal of Experimental Biology **202**: 3285-3294.

Currey, J. D. (2002). Bones Structure and Mechanics.2nd. Princeton University Press.

Currey, J. D. (2003). "Role of collagen and other organics in the mechanical properties of bone." Osteoporosis International **14**(5): S29-S36.

Currey, J. D., T. Landete-Castillejos, J. Estevez, F. Ceacero, A. Olguin, A. Garcia and L. Gallego (2009). "The mechanical properties of red deer antler bone when used in fighting." The Journal of Experimental Biology **212**: 3985-3993.

Doty, S., R. A. Robinson and B. Schofield (1976). Morphology of bone and histochemical staining characteristics of bone cells. Handbook of Physiology G. D. Aurbach. Washington D.C., American Physiology Society**:** 3-23.

Ejersted, C., T. T. Andreassen, H. Oxlund, P. H. Jorgensen, B. Bak, J. Haggblad, O. Torring and M. H. L. Nilsson (1993). "Human Parathyroid Hormone (1-34) and (1-84) Increase the Mechanical Strength and Thickness of Cortical Bone in Rats." Journal of Bone and Mineral Research **8**(9): 1097-1101.

Eppell, S. J., W. Tong, J. L. Katz, L. Kuhn and M. J. Glimcher (2001). "Shape and size of isolated bone mineralites measured using atomic force microscopy." Journal of Orthopaedic Research **19**(6): 1027-1034.

Evans, F. G. (1973). Mechanical Properties of Bone.Springfield, Charles C. Thomas.

Fantner, G. E., T. Hassenkam, J. H. Kindt, J. C. Weaver, H. Birkedal, L. Pechenik, J. A. Cutroni, G. A. G. Cidade, G. D. Stucky, D. E. Morse and H. G. Hansma (2005). "Sacrificial bonds and hidden length dissipate energy as mineralized fibrils separate during bone fracture." Nature Materials **4**: 612-616.

Fantner, G. E., O. Rabinovych, G. Schitter, P. Thurner, J. H. Kindt, M. M. Finch, J. C. Weaver, L. S. Golde, D. E. Morse, E. A. Lipman, I. W. Rangelow and P. K. Hansma (2006). "Hierarchical interconnections in the nano-composite material bone: Fibrillar cross-links resist fracture on several length scales." Composites Science and Technology **66**: 1202-1208.

Fratzl-Zelman, N., P. Roschger, A. Gourrier, M. Weber, B. M. Misof, N. Loveridge, J. Reeve, K. Klaushofer and P. Fratzl (2009). "Combination of Nanoindentation and Quantitative Backscattered Electron Imaging Revealed Altered Bone Material Properties Associated with Femoral Neck Fragility." Calcified Tissue International **85**(4): 335-343.

Fratzl, P., H. S. Gupta, E. P. Paschalis and P. Roschger (2004). "Structure and mechanical quality of the collagen-mineral nano-composite in bone." Journal of Materials Chemistry **14**(14): 2115-2123.

Fratzl, P. and R. Weinkamer (2007). "Nature's hierarchical materials." Progress in Materials Science **528**: 1263-1334.

Frost, H. M. and W. S. S. Jee (1992). "On the rat model of human osteopenias and osteoporoses." Bone and Mineral **18**(3): 227-236.

Galloway, J. (1985). Structure of collagen fibrils. Biology of Invertebrate and Lower Vertebrate Collagens A. Bairoti and R. Garrone. New York, Plenum**:** 73-82.

Ganss, B., R. H. Kim and J. Sodek (1999). "Bone sialoprotein." Crit Rev Oral Biol Med **10**(1): 79-98.

Gebhardt, W. (1906). "Über funktionelle wichtige Anordnungsweisen der feineren und gröberen Bauelemente des Wirbeltierknochens. II. Spezieller Teil. Der Bau der Haversschen Lamellensysteme und seine funktionelle Bedeutung. ." Arch. Entwickl. Mech. Org. **20**: 187-322.

Giannuzzi, L. A. and F. A. Stevie (1999). "A review of focused ion beam milling techniques for TEM specimen preparation." Micron **30**: 197-204.

Gilmore, R. S. and J. L. Katz (1982). "Elastic properties of apatites." Journal of Materials Science **17**(4): 1131-1141.

Giraud-Guille, M. M. (1988). "Twisted Plywood Architecture of Collagen Fibrils in Human Compact Bone Osteons." Calcified Tissue International **42**: 167-180.

Gould, J. (2009). cited 2011; Available from: http://www.docstoc.com/docs/4212130/Blank-Long-Bone-Diagram. B. L. B. Diagram.

Grynpas, M. (1993). "Age and disease-related changes in the mineral of bone." Calcified Tissue International **53**(Supplement 1): S57-S64.

Grynpas, M. D., L. C. Bonar and M. J. Glimcher (1984). "X-ray diffraction radial distribution function studies on bone mineral and synthetic calcium phosphates." Journal Materials Science **19**: 723-736.

Guo, X. E. and S. A. Goldstein (2000). "Vertebral Trabecular Bone Microscopic Tissue Elastic Modulus and Hardness Do Not Change in Ovariectomized Rats." Journal of Orthopaedic Research **18**(2): 333-336.

Gupta, H. S., U. Stachewicz and W. Wagermaier (2006). "Mechanical modulation at the lamellar level in osteonal bone." J. Mater. Res. **21**(8): 1913-1921.

Gupta, H. S. and P. Zioupos (2008). "Fracture of bone tissue: The 'hows' and the 'whys'." Medical Engineering and Physics **30**: 1209-1226.

Halpin, J. C. and J. L. Kardos (1976). "The Halpin-Tsai Equations: A Review." Polymer Engineering and Science **16**(5): 344-352.

Hang, F. and A. H. Barber (2011). "Nano-mechanical properties of individual mineralized collagen fibrils from bone tissue." J. R. Soc. Interface **8**(57): 500-505.

Hang, F., D. Lu, R. J. Bailey, I. Jimenez-Palomar, U. Stachewicz, B. Cortes-Ballesteros, M. Davies, M. Zech, C. Bödefeld and A. H. Barber (2011). "In situ tensile testing of nanofibers by combining atomic force microscopy and scanning electron microscopy." Nanotechnology **22**(36).

Hauge, E. M., T. Steiniche and T. T. Andreassen (2003). Histomorphometry of Metabolic Bone Conditions. Handbook of Histology Methods for Bone and Cartilage Y. H. An and K. L. Martin. Totowa, NJ, Human Press Inc**:** 391-410.

Hodge, A. J. (1989). "Molecular Models Illustrating the Possible Distributions of 'Holes' in Simple Systematically Staggered Arrays of Type Collagen Molecules in Native-Type Fibrils." Connective Tissue Research **21**(1-4): 137-147.

Hoffler, C. E., X. E. Guo, P. K. Zysset and S. A. Goldstein (2005). "An Application of Nanoindentation Technique to Measure Bone Tissue Lamellae Properties." Journal of Biomechanical Engineering **127**(7): 1046-1054.

Hull, D. and T. W. Clyne (2001). An Introduction to Composite Materials.Second. Cambridge, UK, Cambridge University Press.

Iacono, M. V. (2007). "Osteoporosis: A National Public Health Priority." Journal of PeriAnesthesia Nursing **22**(3): 175-183.

Ingram, R. T., B. L. Clarke, L. W. Fisher and L. A. Fitzpatrick (1993). "Distribution of noncollagenous proteins in the matrix of adult human bone: evidence of anatomic and functional heterogeneity." Journal of Bone and Mineral Research **8**(9): 1019-29.

Ingram, R. T., M. Collazo-Clavell, R. Tiegs and L. A. Fitzpatrick (1996). "Paget's disease is associated with changes in the immunohistochemical distribution of noncollagenous matrix proteins in bone." Journal of Clinical Endocrinology and Metabolism **81**(5): 1810-20.

Isaksson, H., S. Nagao, M. Malkiewicz, P. Julkunen, R. Nowak and J. S. Jurvelin (2010). "Precision of nanoindentation protocols for measurement of viscoelasticity in cortical and trabecular bone." Journal of Biomechanics **43**: 2410-2417.

Jäger, I. and P. Fratzl (2000). "Mineralized Collagen Fibrils: A Mechanical Model with a Staggered Arrangement of Mineral Particles." Biophysical Journal **79**: 1737-1746.

Jimenez-Palomar, I., A. Shipov, R. Shahar and A. H. Barber (2012). "Influence of SEM vacuum on bone micromechanics using in situ AFM." Journal of the Mechanical Behavior of Biomedical Materials **5**: 149-155.

Jorgensen, P. H., B. Bak and T. T. Andreassen (1991). "Mechanical Properties and Biochemical Composition of Rat Cortical Femur and Tibia after Long-Term Treatment with Biosynthetic Human Growth Hormone." Bone **12**: 353-359.

Kasra, M., C. M. Vanin, N. J. MacLusky, R. F. Casper and M. D. Grynpas (1997). "Effects of Different Estrogen and Progestin Regimens on the Mechanical Properties of Rat Femur." Journal of Orthopaedic Research **15**: 118-123.

Katz, J. L. and A. Meunier (1993). "Scanning acoustic microscope studies of the elastic properties of osteons and osteon lamellae." J Biomech Eng **115**(4B): 543-8.

Keaveny, T. M., E. F. Morgan, G. L. Niebur and O. C. Yeh (2001). "Biomechanics of Trabecular Bone." Annual Review Biomedical Engineering **3**: 307-333.

Koester, K. J., J. W. Ager and R. O. Ritchie (2008). "The true toughness of human cortical bone measured with realistically short cracks." Nature Materials **7**: 672-677.

Krauss, S., P. Fratzl, J. Seto, J. D. Currey, J. A. Estevez, S. S. Funari and H. S. Gupta (2009). "Inhomogeneous fibril stretching in antler starts after macroscopic yielding: Indication for a nanoscale toughening mechanism." Bone **44**: 1105-1110.

Landis, W. J., K. J. Hodgens, J. Arena, M. J. Song and B. F. McEwen (1996). "Structural relations between collagen and mineral in bone as determined by high voltage electron microscopic tomography." Microscopy Research and Technique **33**(2): 192-202.

Landis, W. J., M. J. Song, A. Leith, L. McEwen and B. F. McEwen (1993). "Mineral and organic matrix interaction in normally calcifying tendon visualised in three dimensions by high-voltage electron microscopic tomography and by graphic image reconstruction." Journal of Structural Biology **110**(39-54).

Lennard-Jones, J. E. (1925). "On the Forces between Atoms and Ions." Proceedings of the Royal Society of London. Series A, Containing Papers of a Mathematical and Physical Character **109**(752): 584-597.

Les, C. M., J. H. Keyak, S. M. Stover, K. T. Taylor and A. J. Kaneps (1994). "Estimation of material properties in the equine metacarpus with use of quantitative computed tomography." Journal of Orthopeadic Research **12**: 822-833.

Lewis, G. and J. S. Nyman (2008). "The use of Nanoindentation for Characterizing the Properties of Mineralized Hard tissue: State-of-the Art Review." Journal of Biomedical Materials Research Part B: Applied Biomaterials **87B**(1): 286-300.

Liu, D., H. D. Wagner and S. Weiner (2000). "Bending and fracture of compact circumferential and osteonal lamellar bone of the baboon tibia." Journal of Materials Science: Materials in Medicine **11**(1): 49-60.

Liu, D., S. Weiner and D. Wagner (1999). "Anisotropic mechanical properties of lamellar bone using miniature cantilever bending specimens." Journal of Biomechanics **2**: 647}654.

Lu, D. and A. H. Barber (2012). "Optimized nanoscale composite behaviour in limpet teeth." J. R. Soc. Interface **9**: 1318-1324.

Maïmoun, L., T. C. Brennan-Speranza, R. Rizzoli and P. Ammann (2012). "Effects of ovariectomy on the changes in microarchitecture and material level properties in response to hind leg disuse in female rats." **51**(3): 586–591.

Maitland, M. E. and A. L. Arsenault (1989). "A correlation between the distribution of biological apatite and amino acid sequence of type I collagen." Calcified Tissue International **48**(5): 341-352.

Marcus, R. and M. L. Bouxsein (2010). The Nature of Osteoporosis. Fundamentals of Osteoporosis R. Marcus, D. Feldman, D. A. Nelson and C. J. Rosen. San Diego, Academic Press**:** 25-34.

Marotti, G. (1993). "A New Theory of Bone Lamellation." Calcified Tissue International **53**(Supplement 1): S47-S56.

Martin, R. B., V. A. Gibson, S. M. Stover, J. C. Gibeling and L. V. Griffin (1996). "Osteonal Structure in the Equine Third Metacarpus." Bone **19**(2): 165-171.

Martin, R. B. and J. Ishida (1989). "The Relative Effects of Collagen Fiber Orientation, Porosity, Density and Mineralization on Bone Strength." Journal of Biomechanics **22**(5): 419-426.

McBroom, R. J., W. C. Hayes, W. T. Edwards, R. P. Goldberg and A. A. White (1985). "Prediction of vertebral body compressive fracture using quantitative computed tomography." The Journal of Bone and Joint Surgery **67**(8): 1206-1214.

McCreadie, B. R., M. D. Morris, T. Chen, R. D. Sudhaker, W. F. Finney, E. Widjaja and S. A. Goldstein (2006). "Bone tissue compositional differences in women with and without osteoporotic fracture." Bone **39**(6): 1190-1195.

McGuigan, F. E. A., G. Armbrecht, R. Smith, D. Felsenberg, D. M. Reid and S. H. Ralston (2001). "Prediction of Osteoporotic Fractures by Bone Densitometry and COLIA1 Genotyping: A Prospective, Population-Based Study in Men and Women." Osteoporosis International **12**(2): 91-96.

Morais, J. J. L., M. F. S. F. deMoura, F. A. M. Pereira, J. Xavier, N. Dourado, M. I. R. Dias and J. M. T. Azevedo (2010). "The double cantilever beam test applied to mode I fracture characterization of cortical bone tissue." Journal of the Mechanical Behavior of Biomedical Materials **3**: 446-453.

Nanci, A. (1999). "Content and distribution of noncollagenous matrix proteins in bone and cementum: Relationship to speed of formation and collagen packing density." Journal of Structural Biology **126**(3): 256-269.

National Cancer Institute's SEER Program, U. S. (2011). Compact bone & Spongy (Cancellous Bone). Available from: http://training.seer.cancer.gov/anatomy/skeletal/tissue.html, U.S. National Cancer Institute.

NIH-consensus-statement (2001). "Osteoporosis prevention, diagnosis, and therapy." JAMA **285**(6): 785-795.

Nyman, J. S., A. Roy, X. Shen, R. L. Acuna, J. H. Tyler and X. Wang (2006). "The influence of water removal on the strength and toughness of cortical bone." Journal of Biomechanics **39**(5): 931-938.

Ohler, B. (2007). Practical Advice on the Determination of Cantilever Spring Constants. Veeco Instruments Inc., Veeco Instruments Inc.**:** 1-12.

Ou-Yang, H., E. P. Paschalis, W. E. Mayo, A. L. Boskey and R. Mendelsohn (2001). "Infrared Microscopic Imaging of Bone: Spatial Distribution of CO_3^{2-}." Journal of Bone and Mineral Research **165**: 893-900.

Paschalis, E. P., E. Shane, G. Lyritis, G. Skarantavos, R. Mendelsohn and A. L. Boskey (2004). "Bone Fragility and Collagen Cross-Links." Journal of Bone and Mineral Research **19**(12): 2000-2004.

Peterlik, H., P. Roschger, K. Klaushofer and P. Fratzl (2006). "From Brittle To Ductile Fracture Of Bone." Nature Materials **5**: 52-55.

Pithioux, M., P. Lasaygues and P. Chabrand (2002). "An alternative ultrasonic method for measuring the elastic properties of cortical bone." Journal Biomechanics **35**(7): 961-968.

Prockop, D. J. and A. Fertala (1998). "The Collagen Fibril: The Almost Crystalline Structure." Journal of Structural Biology **122**: 111-118.

Prostak, K. S. and S. Lees (1996). "Visualization of crystal matrix structure in situ demineralization of mineralized turkey tendon and bone." Calcified Tissue International **59**: 474-479.

Ramachandran, G. N. (1967). Structure of collagen at the molecular level. Treatise on Collagen: Chemistry in Collagen. New York, Academic Press. **1:** 103-184.

Ramasamy, J. G. and O. Akkus (2007). "Local variations in the micromechanical properties of mouse femur: The involvement of collagen fiber orientation and mineralization." Journal of Biomechanics **40**: 910-818.

Reilly, D. T. and A. H. Burstein (1975). "The elastic and ultimate properties of compact bone tissue." Journal Biomechanics **8**(6): 393-396.

Reilly, G. and J. D. Currey (1999). "The Development of Microcracking Failure in Bone Depends on the Loading Mode to Which it is Adapted." The Journal of Experimental Biology **202**: 543-552.

Renugopalakrishnan, V., G. Chandrakason, S. Moore, T. B. Hutson, C. V. Berney and R. S. Bhatnagar (1989). "Bound Water in Collagen. Evidence from Fourier Transform Infrared and Fourier Transform Infrared Photoacoustic Spectroscopic Study." Macromolecules **22**: 4121-4124.

Rho, J. Y., J. D. Currey, P. Zioupos and G. Pharr (2001). "The Anisotropic Young's Modulus of Equine Secondary Osteons and Interstitial Bone Determined by Nanoindentation." The Journal of Experimental Biology **204**: 1775-1781.

Rho, J. Y., L. Kuhn-Spearing and P. Zioupos (1998). "Mechanical properties and the hierarchical structure of bone." Medical Engineering and Physics **20**: 92-102.

Rho, J. Y., T. Y. Tsui and G. M. Pharr (1997). "Elastic properties of human cortical and trabecular lamellar bone measured by nanoindentation." Biomaterials **18**: 1325-1330.

Rice, J. C., S. C. Cowin and J. A. Bowman (1988). "On the Dependence of the Elasticity and Strength of Cancellous Bone on Apparent Density." Journal Biomechanics **21**(2): 155-168.

Riggs, C. M., L. C. Vaughan, G. P. Evans, L. E. Lanyon and A. Boyde (1993). "Mechanical implications of collagen fibre orientation in cortical bone of the equine radius." Anatomy and Embryology **187**: 239-248.

Ritchie, R. O., K. J. Koester, S. Ionova, W. Yaoc, N. E. Lane and J. W. Ager III (2008). "Measurement Of The Toughness Of Bone: A Tutorial With Special Reference To Small Animal Studies." Bone **43**: 798-812.

Roach, H. I. (1994). "Why does bone matrix contain non-collagenous proteins? The possible roles of osteocalcin, osteonectin, osteopontin and bone sialoprotein in bone mineralisation and resorption." Cell Biology International **18**(6): 617-628.

Roschger, P., H. S. Gupta, A. Berzlanovich, G. Ittner, D. W. Dempster, P. Fratzl, F. Cosman, M. Parisien, R. Lindsay, J. W. Nieves and K. Klaushofer (2003). "Constant mineralization density distribution in cancellous human bone." Bone **32**(3): 316-323.

Roschger, P., E. P. Paschalis, P. Fratzl and K. Klaushofer (2008). "Bone mineralization density distribution in health and disease." Bone **42**(3): 456-466.

Rubin, C. T. and L. E. Lanyon (1984). "Regulation of Bone Formation by Applied Dynamic Loads." The Journal of Bone and Joint Surgery **66-A**(3): 397-402.

Rubin, M. A., I. Jasiuk, J. Taylor, J. Rubin, T. Ganey and R. P. Apkarian (2003). "TEM Analysis of the nanostructure of normal and osteoporotic human trabecular bone." Bone **33**: 270-282.

Sader, J. E., I. Larson, P. Mulvaney and L. R. White (1995). "Method for the calibration of atomic force microscope cantilevers." Rev. Sci. Instrum. **66**(7): 3789-3798.

Sasaki, N., T. Ikawa and A. Fukuda (1991). "Orientation of Mineral in bovine bone and the anisotropic mechanical properties of plexiform bone." Journal Biomechanics **24**(1): 57-61.

Schaffler, M. B. and D. B. Burr (1988). "Stiffness of Compact Bone: Effects of Porosity and Density." Journal Biomechanics **21**(1): 13-16.

Sedlin, E. D. and C. Hirsch (1966). "Factors affecting the determination of the physical properties of femoral cortical bone." Acta Orthopedica Scandinavica **37**: 29-48.

Shahar, R., P. Zaslansky, M. Barak, A. A. Friesem, J. D. Currey and S. Weiner (2007). "Anisotropic Poisson's Ratio And Compression Modulus Of Cortical Bone Determined By Speckle Interferometry." Journal of Biomechanics **40**: 252–264.

Silva, M. J., M. D. Brodt, Z. Fan and J.Y.Rho (2004). "Nanoindentation and whole-bone bending estimates of material properties in bones from the senescence accelerated mouse SAMP6." **37**(11): 1639–1646.

Silva, M. J. and L. J. Gibson (1997). "Modeling the Mechanical Behavior of Vertebral Trabecular Bone: Effects of Age-Related Changes in Microstructure." Bone **21**(2): 191-199.

Tai, K., M. Dao, S. Suresh, A. Palazoglu and C. Ortiz (2007). "Nanoscale heterogeneity promotes energy dissipation in bone." Nature Materials **6**: 454-462.

Turner, C. H. (2002). "Biomechanics of Bone: Determinants of Skeletal Fragility and Bone Quality." Osteoporosis International **13**(2): 97-104.

TutorVista. (2012). "Rat skeletal system illustration with parts." Retrieved 13/8/2012, 2012, from http://www.tutorvista.com/content/biology/biology-iii/animal-morphology/skeletal-digestive-circulatory-system-rat.php#.

Ubic, R. (2005). MAT 400 Structural Characterisation of Materials. Lecture notes. Q. M. U. o. London. London, 64-73.

Utku, F. S., E. Klein, H. Saybasili, C. A. Yucesoy and S. Weiner (2008). "Probing the role of water in lamellar bone by dehydration in the environmental scanning electron microscope." Journal of Structural Biology **162**(3): 361-367.

Wagermaier, W., H. S. Gupta, A. Gourrier, M. Burghammer, P. Roschger and P. Fratzl (2006). "Spiral twisting of fiber orientation inside bone lamellae." Biointerphases **1**(1): 1-5.

Wagermaier, W., H. S. Gupta, A. Gourrier, O. Paris, P. Roschger, M. Burghammer, C. Riekel and P. Fratzl (2007). "Scanning texture analysis of lamellar bone using microbeam synchrotron x-ray radiation." Journal of Applied Crystallography **40**: 115-120.

Wagner, D. and S. Weiner (1992). "On the relationship between the microstructure of bone and its mechanical stiffness." Journal of Biomechanics **25**(11): 1311-1320.

Wainwright, S. A., W. D. Biggs, J. D. Currey and J. M. Gosline (1982). Mechanical Design in Organisms. Princeton University Press.

Weiner, S., T. Arad, I. Sabanay and W. Traub (1997). "Rotated Plywood Structure of Primary Lamellar Bone in the Rat: Orientations of the Collagen Fibril Arrays." Bone **20**(6): 509-514.

Weiner, S., W. Traub and H. D. Wagner (1999). "Lamellar Bone: Structure-Function Relations." Journal of Structural Biology **126**(3): 241-255.

Weinkamer, R. and P. Fratzl (2011). "Mechanical adaptation of biological materials - The examples of bone and wood." Materials Science & Engineering C **31**: 1164-1173.

Wenger, M. P. E., L. Bozec, M. A. Horton and P. Mesquida (2007). "Mechanical Properties of Collagen Fibrils." Biophysical Journal **93**: 1255-1263.

Wenger, M. P. E., M. A. Horton and P. Mesquida (2008). "Nanoscale scraping and dissection of collagen fibrils." Nanotechnology **19**.

WHO. (2012, May 25 2012). "National Osteoporosis Guideline Group (NOGG)." Retrieved July 04, 2012, from http://www.shef.ac.uk/NOGG/.

Wilson, E. E., A. Awonusi, M. D. Morris, D. H. Kohn, M. M. J. Tecklenburg and L. W. Beck (2006). "Three Structural Roles for Water in Bone Observed by Solid-State NMR." Biophysical Journal **90**: 3722-3731.

Wolfram, U., H. J. Wilke and P.K. Zysset (2010). "Rehydration of vertebral trabecular bone: Influences on its anisotropy, its stiffness and the indentation work with a view to age, gender and vertebral level." Bone **46**(2): 348-354.

Xu, J., J. Y. Rho, S. R. Mishra and Z. Fan (2003). "Atomic force miscroscopy and nanoindentation characterization of human lamellar bone prepared by microtome sectioning and mechanical polishing technique." Journal of Biomedical Materials Research **67A**: 719-726.

Yan, J., A. Daga, R. Kumar and J. J. Mecholsky (2008). "Fracture toughness and work of fracture of hydrated, dehydrated, and ashed bovine bone." Journal of Biomechanics **41**: 1929-1936.

Yang, Q. D., B. N. Cox, R. K. Nalla and R. O. Ritchie (2006). "Re-Evaluating The Toughness Of Human Cortical Bone." Bone **38**: 878-887.

Zhang, K., B.-J. Park, F.-F. Fang and H. J. Choi (2009). "Sonochemical Preparation of Polymer Nanocomposites." Molecules **14**: 2095-2110.

Ziv, V., H. D. Wagner and S. Weiner (1996). "Microstructure-microhardness relations in parallel-fibered and lamellar bone." Bone **18**(5): 417-428.

Appendix

A. 1. Data Analysis

The following is a description of the method used to analyse the data produced by the Attocube AFM system using a software script that was designed to automate the process. Russell J. Bailey, Fei Hang, Dun Lu and Ines Jimenez-Palomar created the method and Carlos J. Pasquali developed the script. Steps are detailed to first identify features on the sinusoidal output data from the Attocube AFM system on graph-plotting software. Specifically, the data should be first manipulated so that the sinusoidal data is of a form that can be subsequently processed by the script.

A.1.1. Calibration data analysis

1. Data from the Attocube AFM system is first exported to a graph-plotting software package, such as Microsoft Excel. First locate amplitude maxima and minima.
2. Normalize y-axis so that all maximum and minimum values are recalculated from +1 to -1 respectively using the following equation:

$$y_{norm} = \frac{2y - y_{\max} - y_{\min}}{y_{\max} - y_{\min}}$$

Note: use the first and last sets of max and min values for the beginning and end portions of the full sinusoidal curve as shown in Figure A.1.

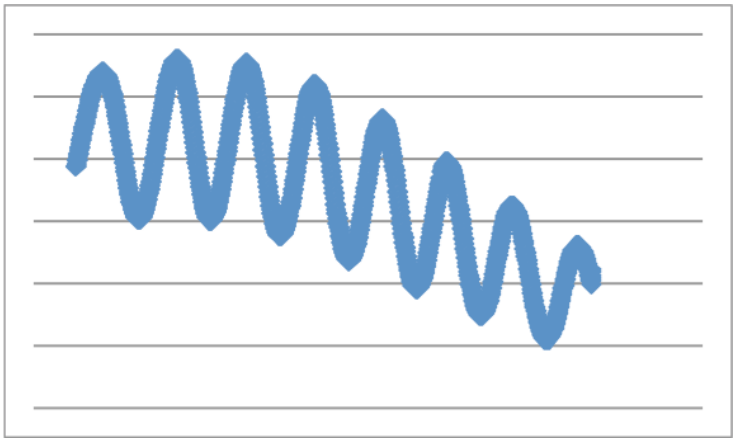

Figure A.1 Original sinusoidal data imported from the Attobcube AFM and displayed on Microsoft Excel.

3. Shift x and y values to origin (0,0) by subtracting by the first value. This is achieved on Excel by positioning all of the data so that the first data point is found in cell A1 so that A1-A$1 is applied to shift everything to the origin.

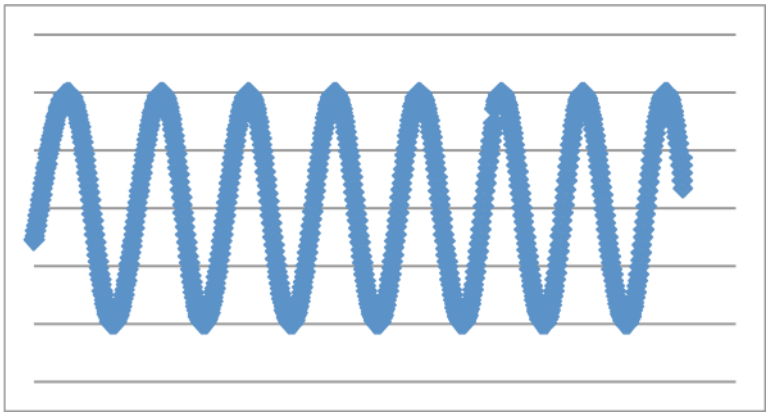

Figure A.2 Plot of the raw data normalized so that all y-axis data falls between +1 and -1, and the curve start is shifted to the origin.

4. The x-axis values were adjusted so that the actual z-piezo movement (as seen live inside the SEM) matches the software movement. Typically, 36 µm of z-piezo movement observed by SEM corresponded to 40 µm of software-recorded movement. The x-axis values are therefore converted using:

$$x_{adjusted} = x \cdot \frac{observed}{software}$$

5. The sinusoidal curve was converted to a linear plot by inputting the y-axis values into Arc-sine and Arc-cosine equations below. This step was needed as each wavelength on the sinusoidal curve corresponds to a progressive bending of the AFM cantilever shown on the y-axis.

$$y_{linear} = A\sin(y_{norm}) \text{ from -1 to +1}$$

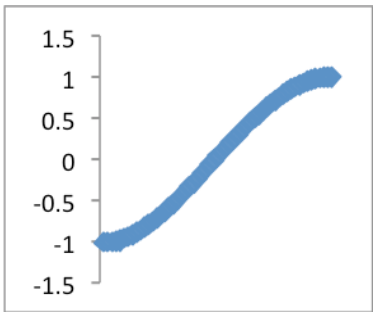

Figure A.3 Plot of the curve converted from a sinusoidal function to a continual accumulation of the y-axis data from -1 to +1.

$$y_{linear} = A\cos(y_{norm}) \text{ from +1 to -1}$$

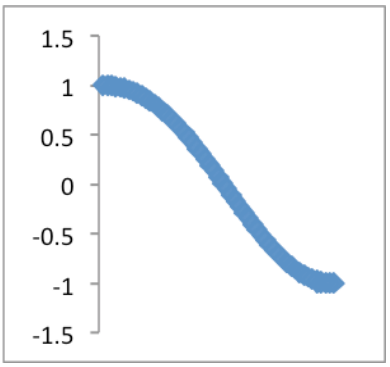

Figure A.4 Plot of the curve converted from a sinusoidal function to a continual accumulation of the y-axis data from +1 to -1.

Note: There is no need to divide the curve into different sections, just drag the Arc sine and cosine equations down until a maximum or minimum value is reached, apply it to the max or min value and change the equation on the next value. Alternate Asin and Acos equation as required.

The table below indicates when x values in the left column are converted using with Asin or Acos functions depending if the values are going from a maximum to a minimum or viceversa as the sinusoidal curve progresses.

Table A.1 – Example of the x and y-axis data; indicating where the formula needs to change from the Asin to the Acos equation and vices versa.

+1	Asin
0.75	Acos
0.5	
0.25	
0	
-0.25	
-0.5	
-0.75	
-1	Acos
-0.75	Asin

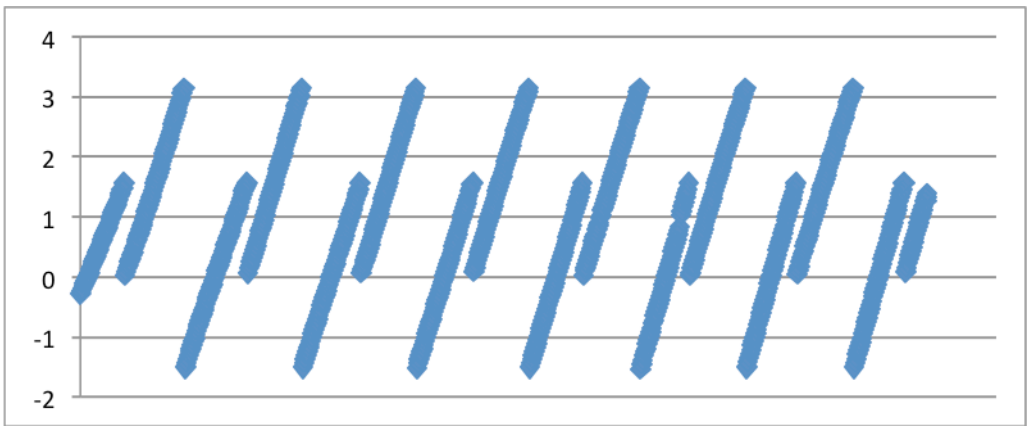

Figure A.5 Resultant plot of data for each converted section shown in A.3 and A.4.

6. All of the linear sections are matched together by adding increasing wave periods using the equation:

$$y_{match} = y_{linear} + i\pi$$

The 'i' values from above are selected so that the linear-like sections in A.5 can be connected together as shown in Figure A.6.

Table A.2 – Example of the 'i' incrementing values used in order to match all linear sections to create a single linear curve.

i	**Curve y_{linear} values**
0	Start to +1
0.5	+0.99 to -1
2	-0.99 to +1
2.5	+0.99 to -1
4	-0.99 to +1
4.5	+0.99 to -1
6	-0.99 to +1
6.5	+0.99 to -1
8	-0.99 to +1

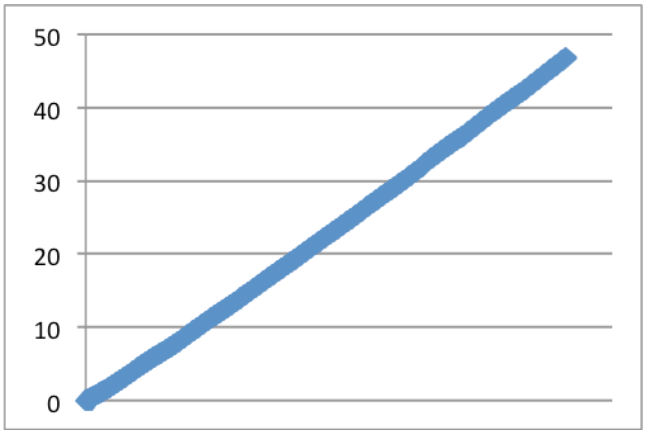

Figure A.6 Plot of all linear sections of the curve matched to form one linear curve.

Note: The equation applied to the data has to be changed <u>after</u> the max or min value. The same applies to all of the previous equations.

7. Intensity y-values (in volts) converted to distance values (in metres) using the known wavelength, λ = 1200 nm, of the laser using the following equation:

$$y_{meters} = \frac{y_{match} \cdot \lambda}{2\pi}$$

where

$\lambda = 655 \times 10^{-9} m$

8. The linear trend-line equation for the calibration data calculated to find the 'Calibration Factor' also known as the 'Russell Factor', defined by the value that needs to be multiplied to the calibration data in order to get a slope of 1.

This calibration is required in order to normalize the data to match the assumption that during the calibration, the cantilever deflects 1 nm to every 1 nm of z-piezo movement. The calibration factor is used later in order to adjust the test data.

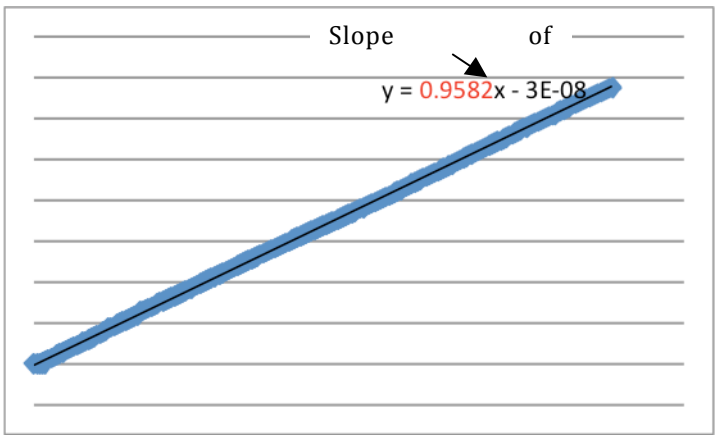

Figure A.7 Calibration Factor calculated by fitting a linear trend line to the calibration curve (all in metres).

A.1.2. Test data analysis

1. Follow steps 1-7 of the previous section
2. The end result is a linear curve with units of meters both in the x- and y-axis.
3. Multiply Y values by (1/slope of calibration)
4. Displacement = X-Y
   =Z-piezo movement - Cantilever Bending

   Force = Y*Spring Constant
5. Calculations of strain and stress as per normal.

A.2. Using the script for the data analysis

You will notice that the script has notes detailing what step it is carried out and where. Each step of the script below follows the Data Analysis process described previously.

A.2.1. Operating the script with Octave

1. Download Octave from http://octave.sourceforge.net/ and select your operating system.

2. Create a folder in c:/ called "data" thus making the address of the file is c:/data

3. Prepare the data:

The data has to be in the following format:

X,Y;X,Y;X,Y

e.g.:

1.82999484e-05,3.29872617;1.83036107e-05,3.28811732;1.83072731e-05,3.27713902;1.83109355e-05,3.26572188;1.83145979e-05,3.25567576;1.83182603e-05,3.24454508;

*I recommend opening the data on "Notepad ++" that comes with the octave package as it is quick and allows certain replacements that cannot be performed in any other notepad application.

a. Open data in Notepad++

b. Search→ Replace→ ; for ,

c. Select a "Paragraph" of the data by selecting the empty space after the Y value and dragging it along to the next cell before the X value. Then go Search→ Replace→ [ ] for ;

d. Select a "Space" of the data by selecting the space between the coma and the number. Then go Search→ Replace→ [ ] for "leave empty".

e. Search→ Find → "curve" and erase "#cuve2;" in order to avoid problems with the script.

You should have the data displayed as a string of numbers shown above.

4. Insert the string of numbers in SCRIPT1 in between the brackets ie Raw = [DATA IN THE FORM OF STRING OF NUMBERS] ;

You can select the string of numbers easily by placing the cursor before the first number, and applying SHIFT+END before pasting the data into the brackets. Make sure there is no ';' at the end of the last data point to avoid problems.

5. Open SCRIPT2 and input the values according to your data:

For example:

SoftAdj = 0.9;

CalibFact = 0.743;

CantiSpring = 40;

BeamLength = 8.29e-6;

BeamCross = 4.57e-12;

These parameters represent the following values:

SoftAdj = Software Adjustment (the SEM observed movement of the z-peizo positioner vs the software selected z-piezo movement). This number is usually an SEM observed 36 μm when selecting 40 μm using the AFM software, which gives a SoftAdj=36/40=0.9

CalibFact= Calibration Factor. This number is given by running the data of the Calibration through SCRIPT1. You will notice that it will give you different values; the nature of this difference is described above each value. I usually use the first value as this value is calculated using all of the data.

CantiSpring= Cantilever Spring Constant

BeamLength = Beam Length as measured in the SEM

BeamCross= Beam Cross section, the cross section area of the beam = width x thickness.

6. Run Octave:

*Note: ENTER means press Enter or Return.

a. addpath c:/data ENTER

b. SoftAdj=0.9 ENTER

c. If calibrating then type SCRIPT1 ENTER

If experimental data processing then type SCRIPT2 ENTER

d. Script will give you the option of forward (f), back (b) or quit (q)

Press f in order to observe the data. Data is suitable when outputting 4 columns of non-zero numbers. Press q.

e. In order to create a *.txt file with the data place the following command:

save -text c:/data/ans.txt ans; ENTER

*Note that you can change the name of the text file by just changing the word before the ".txt" in the command.

After every run of the script type in 'clear all' ENTER.

Notes:

Remember that this script was specifically developed for AFM tip movement into the sample such as compression and cantilever bending data analysis. The script may be possible for other types of manipulation.

Definitions of Script 2:

Script 2

CALIB(:,1) = CALIB(:,1).*CalibFact;

CALIB(:,3) = CALIB(:,2) - CALIB(:,1);

CALIB(:,4) = CALIB(:,1).*CantiSpring;

CALIB(:,5) = CALIB(:,3)./BeamLength;

CALIB(:,6) = CALIB(:,4)./BeamCross;

CALIB(:,7) = CALIB(:,5).*100;

CALIB(:,8) = CALIB(:,6)*(1E10^(-6));

[CALIB(:,3),CALIB(:,4),CALIB(:,5),CALIB(:,6)]

Definitions

CALIB1 is the Calibration with the Calibration Factor taken into account

CALIB3 is the Displacement

CALIB4 is the Force

CALIB5 is the Strain

CALIB6 is the Stress

CALIB7 is the Strain in %

CALIB8 is the Stress in MPa

And the last line expresses what the output of the SCRIPT2 is which is:

1st column = Displacement

2nd column = Force

3rd column = Strain

4th column = Stress

A.3. Troubleshooting

1. If the data is too noisy at the beginning:

You have to remove the data from the beginning until "contact point" or until it stops being so noisy. Otherwise it will cause problems when running the SCRIPT1 or SCRIPT2.

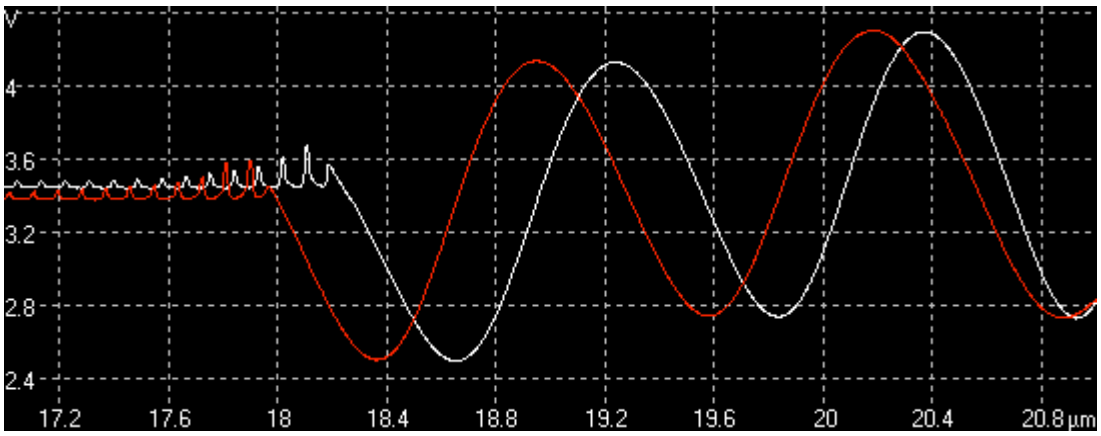

Figure A.8 Screen shot of raw sinusoidal data curve gathered from the Attocube's interferometer.

2. If there are problems and the SCRIPT2 does not seem to want to run:

a. make sure you have defined SoftAdj. ie SoftAdj=0.9 before running SCRIPT2 or even SCRIPT1. (Usually if this is the problem it will say so.)

b. exit Octave and open it again

c. change the "tol=" value that is in SCRIPT1 Line 11.

Note: The set value of "tol" should be always left as 8. If the curve does not have enough periods, I recommend lowering "tol" to 2 or 3. The data that is outputted will not be very accurate but at least it will give a relative curve.

*I recommend always having at least 4 or 5 periods (or max, min values) on the data to avoid this problem.

A.4. Script

```
1;


#This file calibrates and normalizes input data.


RAW = [INSERT DATA];


#Global definitions

#This is necessarily a magic number, be sure to specify it so that it is << than the amount of data RAW contains, four seems to work pretty well.

numofmaxmins = 4;

#Checks for upward or downward trend

tol = 8;



#---------------------------

#Function definitions


function [a, b] = findupdownrun(c, d, SECTION, tol)


  #Check if there is an increasing run


  for a = c:size(SECTION)

    count = 0;

    for g = 1:tol
```

```
        if(SECTION(a+g-1,2) < SECTION(a+g,2))
            count = count+1;
        else
            break;
        endif
    endfor
    if count == tol
        break;
    endif
endfor

#Check if there is a decreasing run first.

for b = d:size(SECTION)
    count = 0;
    for g = 1:tol
        if(SECTION(b+g-1,2) > SECTION(b+g,2))
            count = count+1;
        else
            break;
        endif
    endfor
    if count == tol
        break;
    endif
endfor

endfunction
```

```
#----------------------------------------


#Main part of the script

[a, b] = findupdownrun(1, 1, RAW, tol);

#Which run is closer, the increasing run or decreasing run?  Scrub out data
up to either closest run.

if a < b
   incdec = 1;
   CONTACT = [RAW(a:size(RAW), :)];
else
   incdec = -1;
   CONTACT = [RAW(b:size(RAW), :)];
endif

#Zero the X values

XSHIFT(1:size(CONTACT),1) = CONTACT(1,1);
XSHIFT(:,2) = 0;

CONTACTZERO = CONTACT - XSHIFT;

   #Recalibrate the up or down run position
```

```
    if incdec == 1
        b = b - a;
        a = 1;
    else
        a = a - b;
        b = 1;
    endif

#Create a max / min position matrix

#Write in the first and additional entries

if incdec == 1
    [m,im] = max(CONTACTZERO(a:b+6,2));
    MAXMIN(1,1) = a+im-1;
    MAXMIN(1,2) = m;
    for i = 2:numofmaxmins
        [a,b] = findupdownrun(b+6, b+6, CONTACTZERO, tol);
        [m,im] = min(CONTACTZERO(b:a+6,2));
        MAXMIN(i-1,3) = b+im-1;
        MAXMIN(i-1,4) = m;
        [a,b] = findupdownrun(a+6, a+6, CONTACTZERO, tol);
        [m,im] = max(CONTACTZERO(a:b+6,2));
        MAXMIN(i,1) = a+im-1;
        MAXMIN(i,2) = m;
    endfor
else
```

```
   #Yet to check
   [m,im] = min(CONTACTZERO(b:a+6,2));
   MAXMIN(1,3) = b+im-1;
   MAXMIN(1,4) = m;
   for i = 2:numofmaxmins
      [a,b] = findupdownrun(a+6, a+6, CONTACTZERO, tol);
      [m,im] = max(CONTACTZERO(a:b+6,2));
      MAXMIN(i,1) = a+im-1;
      MAXMIN(i,2) = m;
      [a,b] = findupdownrun(b+6, b+6, CONTACTZERO, tol);
      [m,im] = min(CONTACTZERO(b:a+6,2));
      MAXMIN(i,3) = b+im-1;
      MAXMIN(i,4) = m;
   endfor
endif

#Normalize

NORMED(:,1) = CONTACTZERO(:,1);

if incdec == 1
   #Use the next max and 1-step forward min until we reach the such to
normalize.
   e = MAXMIN(1,3);
   MAX(1:e,1) = MAXMIN(1,2);
   MIN(1:e,1) = MAXMIN(1,4);
   NORMED(1:e,2) = (2*CONTACTZERO(1:e,2)-MAX-MIN)./(MAX-MIN);
```

```
  #Now proceed alternating max/mins "manually."


  for i = 2:numofmaxmins
    f = MAXMIN(i,1);
    clear MAX;
    MAX(1:(f-e),1) = MAXMIN(i,2);
    clear MIN;
    MIN(1:(f-e),1) = MAXMIN(i-1,4);
    NORMED(e+1:f,2) = (2*CONTACTZERO(e+1:f,2)-MAX-MIN)./(MAX-MIN);
    e = MAXMIN(i,3);
    clear MIN;
    MIN(1:(e-f),1) = MAXMIN(i,4);
    clear MAX;
    MAX(1:(e-f),1) = MAXMIN(i,2);
    NORMED(f+1:e,2) = (2*CONTACTZERO(f+1:e,2)-MAX-MIN)./(MAX-MIN);
  endfor
else
  #Use the next min and 1-step forward max until we reach the such to
normalize.
  e = MAXMIN(2,1);
  MIN(1:e,1) = MAXMIN(1,4);
  MAX(1:e,1) = MAXMIN(2,2);
  NORMED(1:e,2) = (2*CONTACTZERO(1:e,2)-MAX-MIN)./(MAX-MIN);


  #Now proceed alternating min/max "manually."


  for i = 2:numofmaxmins-1
    f = MAXMIN(i,3);
```

```
      clear MIN;
      MIN(1:(f-e),1) = MAXMIN(i,4);
      clear MAX;
      MAX(1:(f-e),1) = MAXMIN(i,2);
      NORMED(e+1:f,2) = (2*CONTACTZERO(e+1:f,2)-MAX-MIN)./(MAX-MIN);
      e = MAXMIN(i+1,1);
      clear MAX;
      MAX(1:(e-f),1) = MAXMIN(i+1,2);
      clear MIN;
      MIN(1:(e-f),1) = MAXMIN(i,4);
      NORMED(f+1:e,2) = (2*CONTACTZERO(f+1:e,2)-MAX-MIN)./(MAX-MIN);
   endfor

   #The tail is missing
   f = MAXMIN(numofmaxmins,3);
   clear MIN;
   MIN(1:(f-e),1) = MAXMIN(numofmaxmins,4);
   clear MAX;
   MAX(1:(f-e),1) = MAXMIN(numofmaxmins,2);
   NORMED(e+1:f,2) = (2*CONTACTZERO(e+1:f,2)-MAX-MIN)./(MAX-MIN);

endif

#Linearize

if incdec == 1
   LINEAR = NORMED(1:MAXMIN(i,1),:);
```

```
   #Linearize descents
   for i = 1:numofmaxmins
      LINEAR(MAXMIN(i,1)+1:MAXMIN(i,3),3) =
acos(LINEAR(MAXMIN(i,1)+1:MAXMIN(i,3),2));
   endfor

   #Linearize ascents
   #First ascent
   LINEAR(1:MAXMIN(1,1),3) = asin(LINEAR(1:MAXMIN(1,1),2));
   #Subsequent ascents
   for i = 2:numofmaxmins
      LINEAR(MAXMIN(i-1,3)+1:MAXMIN(i,1),3) = asin(LINEAR(MAXMIN(i-
1,3)+1:MAXMIN(i,1),2));
   endfor
else
   LINEAR = NORMED(1:MAXMIN(numofmaxmins,3),:);

   #Linearize ascents
   for i = 1:numofmaxmins-1
      LINEAR(MAXMIN(i,3)+1:MAXMIN(i+1,1),3) =
asin(LINEAR(MAXMIN(i,3)+1:MAXMIN(i+1,1),2));
   endfor

   #Linearize descents
   #First descent
   LINEAR(1:MAXMIN(1,3),3) = acos(LINEAR(1:MAXMIN(1,3),2));
   #Subsequent descents
   for i = 2:numofmaxmins
```

```
    LINEAR(MAXMIN(i,1)+1:MAXMIN(i,3),3) =
acos(LINEAR(MAXMIN(i,1)+1:MAXMIN(i,3),2));

  endfor

endif


#Match


MATCHED = LINEAR;

if incdec == 1

  #Match descents

  for i = 1:numofmaxmins

    switch i

      case 1

        MATCHED(MAXMIN(i,1)+1:MAXMIN(i,3),4) =
MATCHED(MAXMIN(i,1)+1:MAXMIN(i,3),3) + 0.5*pi;

      case 2

        MATCHED(MAXMIN(i,1)+1:MAXMIN(i,3),4) =
MATCHED(MAXMIN(i,1)+1:MAXMIN(i,3),3) + 2.5*pi;

      case 3

        MATCHED(MAXMIN(i,1)+1:MAXMIN(i,3),4) =
MATCHED(MAXMIN(i,1)+1:MAXMIN(i,3),3) + 4.5*pi;

      case 4

        MATCHED(MAXMIN(i,1)+1:MAXMIN(i,3),4) =
MATCHED(MAXMIN(i,1)+1:MAXMIN(i,3),3) + 6.5*pi;

      otherwise

        printf("\n\nProblems with matching.  See script or Guru.\n\n");

    endswitch

  endfor


  #Match ascents
```

```
  #First ascent
  MATCHED(1:MAXMIN(1,1),4) = MATCHED(1:MAXMIN(1,1),3) + 0*pi;
  #Subsequent ascents
  for i = 2:numofmaxmins
    switch i
      case 2
        MATCHED(MAXMIN(i-1,3)+1:MAXMIN(i,1),4) =
MATCHED(MAXMIN(i-1,3)+1:MAXMIN(i,1),3) + 2*pi;
      case 3
        MATCHED(MAXMIN(i-1,3)+1:MAXMIN(i,1),4) =
MATCHED(MAXMIN(i-1,3)+1:MAXMIN(i,1),3) + 4*pi;
      case 4
        MATCHED(MAXMIN(i-1,3)+1:MAXMIN(i,1),4) =
MATCHED(MAXMIN(i-1,3)+1:MAXMIN(i,1),3) + 6*pi;
      case 5
        MATCHED(MAXMIN(i-1,3)+1:MAXMIN(i,1),4) =
MATCHED(MAXMIN(i-1,3)+1:MAXMIN(i,1),3) + 8*pi;
      otherwise
        printf("\n\nProblems with matching.  See script or Guru.\n\n");
    endswitch
  endfor
else
  #Match ascents
  for i = 1:numofmaxmins-1
    switch i
      case 1
        MATCHED(MAXMIN(i,3)+1:MAXMIN(i+1,1),4) =
MATCHED(MAXMIN(i,3)+1:MAXMIN(i+1,1),3) + 1.5*pi;
      case 2
```

```
            MATCHED(MAXMIN(i,3)+1:MAXMIN(i+1,1),4) =
MATCHED(MAXMIN(i,3)+1:MAXMIN(i+1,1),3) + 3.5*pi;

        case 3

            MATCHED(MAXMIN(i,3)+1:MAXMIN(i+1,1),4) =
MATCHED(MAXMIN(i,3)+1:MAXMIN(i+1,1),3) + 5.5*pi;

        case 4

            MATCHED(MAXMIN(i,3)+1:MAXMIN(i+1,1),4) =
MATCHED(MAXMIN(i,3)+1:MAXMIN(i+1,1),3) + 7.5*pi;

        otherwise

            printf("\n\nProblems with matching.  See script or Guru.\n\n");

      endswitch

   endfor


   #Match descents

   #First descent

   MATCHED(1:MAXMIN(1,3),4) = MATCHED(1:MAXMIN(1,3),3) + 0*pi;

   #Subsequent descents

   for i = 2:numofmaxmins

      switch i

         case 2

            MATCHED(MAXMIN(i,1)+1:MAXMIN(i,3),4) =
MATCHED(MAXMIN(i,1)+1:MAXMIN(i,3),3) + 2*pi;

         case 3

            MATCHED(MAXMIN(i,1)+1:MAXMIN(i,3),4) =
MATCHED(MAXMIN(i,1)+1:MAXMIN(i,3),3) + 4*pi;

         case 4

            MATCHED(MAXMIN(i,1)+1:MAXMIN(i,3),4) =
MATCHED(MAXMIN(i,1)+1:MAXMIN(i,3),3) + 6*pi;

         case 5

            MATCHED(MAXMIN(i,1)+1:MAXMIN(i,3),4) =
MATCHED(MAXMIN(i,1)+1:MAXMIN(i,3),3) + 8*pi;
```

```
        otherwise
            printf("\n\nProblems with matching.  See script or Guru.\n\n");
      endswitch
   endfor
endif

#Zero the Y-values

YSHIFT(1:size(MATCHED),1) = MATCHED(1,4);

ALLZEROED(:,1) = MATCHED(:,1);
ALLZEROED(:,2) = MATCHED(:,4) - YSHIFT;

#Convert volts to meters using the laser wavelength
YMETERS = ALLZEROED;

YMETERS(:,3) = ALLZEROED(:,2).*(655*10^(-9))./(2*pi);

#Software adjust the X-values

SOFTED(:,1) = YMETERS(:,1).*0.9;
SOFTED(:,2) = YMETERS(:,3);

#Trend line, using Ordinary Least Squares

printf("\n\n Using all available data from contact up to numofmaxmins = %d,
or %d points\n\n", numofmaxmins, size(SOFTED)(1));
[SLOPE1, SIGMA1, R1] = ols(SOFTED(:,2),SOFTED(:,1));
```

```
SLOPE1

printf("\n\n Using first half of data points \n\n");

[SLOPE2, SIGMA2, R2] =
ols(SOFTED(1:round(size(SOFTED)(1)/2),2),SOFTED(1:round(size(SOFTED)
(1)/2),1));

SLOPE2

printf("\n\n Using second half of data points \n\n");

[SLOPE3, SIGMA3, R3] =
ols(SOFTED(round(size(SOFTED)(1)/2):size(SOFTED)(1),2),SOFTED(round(
size(SOFTED)(1)/2):size(SOFTED)(1),1));

SLOPE3

printf("\n\n Using middle third of data points \n\n");

[SLOPE4, SIGMA4, R4] =
ols(SOFTED(round(size(SOFTED)(1)/3):round(size(SOFTED)(1)/3)*2,2),SOF
TED(round(size(SOFTED)(1)/3):round(size(SOFTED)(1)/3)*2,1));

SLOPE4

printf("\n\n");
```

Second Script

Insert constant parameters and output the data.

```
1;


SCRIPT1;


CalibFact = 1.2;

CantiSpring = 28.25;

BeamLength = 9.35e-06;

BeamCross = 7.02e-12;


CALIB = SOFTED;
```

```
CALIB(:,1) = CALIB(:,1).*(CalibFact);

CALIB(:,3) = CALIB(:,1) - CALIB(:,2);

CALIB(:,4) = CALIB(:,1).*CantiSpring;

CALIB(:,5) = CALIB(:,3)./BeamLength;

CALIB(:,6) = CALIB(:,4)./BeamCross;

CALIB(:,7) = CALIB(:,5).*100;

CALIB(:,8) = CALIB(:,6)*(1E10^(-6));

[CALIB(:,3),CALIB(:,4),CALIB(:,5),CALIB(:,6)]
```